Volumetric Laser Ion Acceleration

Peter Hilz

München 2020

In Memory of
Simon

"Mein Papa weiß alles. Er ist Physiker."
"My dad knows everything. He is physicist."

Elisabeth Hilz, **2017**

Der Gefangene:

Die Gedanken sind frei,
wer kann sie erraten;
sie rauschen vorbei
wie nächtliche Schatten,
kein Mensch kann sie wissen,
kein Jäger sie schießen;
es bleibet dabei:
Die Gedanken sind frei!

Das Mädchen:

Im Sommer ist gut lustig sein
auf hohen wilden Bergen.
Dort findet man grün Plätzelein,
mein Herz verliebtes Schätzelein,
von dir mag ich nicht scheiden!

Der Gefangene:

Und sperrt man mich ein
im finstere Kerker,
dies Alles sind nur
vergebliche Werke;
denn meine Gedanken
zerreißen die Schranken
und Mauern entzwei,
die Gedanken sind frei!

Das Mädchen:

Im Sommer ist gut lustig sein
auf hohen wilden Bergen.
Man ist da ewig ganz allein
auf hohen, wilden Bergen,
man hört da gar kein Kindergeschrei!
Die Luft mag einem da werden,
ja die Luft mag einem werden.

Der Gefangene:

So sei's, wie es sei,
und wenn es sich schicket,
nur Alles, Alles sei in der Stille,
nur All's in der Still!
Mein Wunsch und Begehren,
Niemand kann's wehren!
Es bleibt dabei:
Die Gedanken sind fre!

Das Mädchen:

Mein Schatz, du singst so fröhlich hier,
wie's Vögelein in dem Grase.
Ich steh' so traurig bei Kerkertür,
wär' ich doch tot, wär' ich bei dir,
ach muß, ach muß ich immer denn klagen!?

Der Gefangene:

Und weil du so klagst,
der Lieb' ich entsage!
Und ist es gewagt,
so kann mich Nichts plagen!

So kann ich im Herzen
stets lachen, bald scherzen.
Es bleibet dabei:
Die Gedanken sind frei!

Die Gedanken sind frei!

Volumetric Laser Ion Acceleration

Peter Hilz

Dissertation

an der Fakultät für Physik

der Ludwig–Maximilians–Universität

München

vorgelegt von

Peter Hilz

aus München

München, den 1.10.2020

Erstgutachter: Prof. Dr. Jörg Schreiber

Zweitgutachter: Prof. Dr. Matt Zepf

Tag der mündlichen Prüfung: 17.11.2020

Contents

Contents

List of Figures

Zusammenfassung

In dieser Arbeit wird die Interaktion von intensiven Laserpulsen mit räumlich begrentzen Targets, sogenannten massenlimitierten Targets beschrieben. Die untersuchten Targets hatten eine räumliche Ausdehnung von ca 1 μm, was ungefähr der Wellenlänge des verwendeten Laserlichts entspricht. Aufgrund der geringen Größe würde jegliche Haltestruktur die experimentellen Ergebnisse dominieren oder zumindest massiv verfälschen. Daher wurde eine elektrodynamische Paul-Falle entwickelt, mit deren Hilfe es möglich ist, spährische Targets raumfest schweben zu lassen.

Die für diese Arbeit relevanten Experimente fanden am PHELIX-Laser in Darmstadt statt. Hierbei wurden μm - große Plastikkugeln einer Intensität von $I_L > 10^{20} \frac{W}{cm^2}$ ausgesetzt. Die dadurch beschleunigten Protonenstrahlen hatten für Lasereplasma-beschleuniger atypische Eigenschaften. Normalerweise haben laserbeschleu-nigte Protonenstrahlen ein exponentiell abfallendes Spektrum mit einer wohldefinierten Maximalenergie. Die Protonenstrahlen in dem vorgestellten Experiment besaßen ein monoenergetisches Spektrum mit einer Energie um die 20 MeV und einer spektralen Bandbreite von 25%. Darüber hinaus zeigten die gemessenen Teilchenzahlen, dass ein Großteil der sich in der Kugel befindlichen Protonen in Vorwärtsrichtung beschleunigt worden sind.

Durch eine im Experiment implementierte optische Diagnostik (In-Line-Holography) konnte gezeigt werden, dass das Target signifikant vorexpandiert und der Hauptpuls des Lasers mit einem unterkritischen (optisch transparenten), massenlimitierten Target interagiert hat. Die Kenntnis des Plas-

mazustandes während der Interaktion ermöglichte es, 3D-PIC-Simulationen durchzuführen, welche die experimentellen Ergebnisse reproduzieren.

Subfokusgroße, unterkritische, massenlimitierte Targets haben sich als interessante Targets für die Laser-Ionenbeschleunigung erwiesen. Sie ermöglichen eine volumetrische Laser-Target-Interaktion, welche zu monoenergetischen Protononenstrahlen führt. Das vorgestellte Experiment stellt eine erste Demonstration dieses neuartigen Beschleunigungsprozesses dar. Weitere Experimente sind notwendig, um ein tieferes Verständnis für die zugrunde liegenden physikalischen Mechanismen zu erlangen und den Beschleunigungsprozess in Zukunft zu optimieren. Hierbei können 3D PIC Simulation helfen, geeignete Parameter für zukünftige Experimente zu finden.

In Hinblick auf die neue Generation von Hochintensitätlasern (GIST, ATLAS 3000, etc) können die besonderen Eigenschaften eines unterkritischen, massenlimitierten Targets viele technische Probleme lösen (Debris, Rückreflex, Laser Kontrast, Elektromagnetischer Puls etc).

Die gewonnenen Ergebnisse wurden im Journal Nature Communications veröffentlicht [1].

Abstract

This work describes the interaction of an intense laser pulse with spatial constrained targets, so called mass limited targets. The used targets had a size of approximately 1 μm, comparable to the wavelength of the driving laser. Due to the size, every mounting structure would have severe impact on the experimental results. To avoid this, an electrodynamic Paul trap was developed, which enabled the stationary levitation of spherical targets.

The experiments, relevant for this work, were conducted at the PHELIX laser situated in Darmstadt. μm - sized plastic beads were exposed to an intensity of $I_L > 10^{20} \frac{W}{cm^2}$. The obtained proton beams had atypical properties. Normally laser-accelerated proton beams exhibit an exponentially decaying energy spectrum with a well defined maximum cut off energy. The proton beams in the presented experiment were mono-energetic with a peak energy around 20 MeV and a spectral bandwidth of 25%. The measured particle numbers indicated that a large fraction of the protons contained in the target were accelerated collinear with the laser.

The implementation of an optical diagnostic (in-line-holography) in the experiment showed a severe pre-expansion of the target. It was shown that the main laser pulse interacted with an under-critical (optically transparent), mass limited target. The knowledge of the plasma state during the interaction enabled to conduct 3D-PIC simulations, which reproduced the experimental results quantitatively.

Sub-focus sized, under-critical, mass-limited targets have shown to be interesting targets for laser ion acceleration. They enable a volumetric laser-

target-interaction, which lead to mono-energetic proton beams. The conducted experiment, can be seen as a first demonstration of this new acceleration process. Further experiments are necessary, to obtain a deeper understanding of the underlying physical mechanisms and to optimize the acceleration process in the future. Hereby 3D PIC simulation can serve as a guidance to select the right parameters in future experiments.

Regarding the new generation of high intensity lasers (ATLAS 3000, GIST) a mass limited, under-critical target can solve many technical issues (debris, laser contrast, electromagnetic pulse etc.).

The obtained results were published in the journal Nature Communications [1].

Chapter 1

Introduction

$$F = m \cdot a \tag{1.1}$$

Equation (1.1) describes the acceleration of objects in the presence of a force. It is known as Newton's second law. Equation (1.1) is of great simplicity and beauty. Even small children understand it intuitively. They pick up a stone and throw it, then the pick it up again and throw it harder and finally they search for smaller stones.

Increasing the forces and decreasing the mass of the projectile has proven to be an effective strategy to increase the velocity of a projectile. Accelerators resembled outstanding technological achievements in human history. For example the newly developed longbows of the English were decisive during the famous medieval battles of Crécy [2] and Agincourt [3].

The smallest possible projectile mass constitutes a single elementary particle. Nowadays physicists use electromagnetic forces to accelerate charged elementary particles. This allows to achieve velocities close to the speed of

light, the ultimate speed limit of nature.[1]

Particle accelerators resemble outstanding technological achievements of contemporary history. They lead to numerous scientific findings such as e.g., X-rays [7], which enabled new experimental techniques such as X-ray crystallography [8]. Many technological achievements are based on accelerators such as electron microscopy [9] and electron beam lithography [10]. Without all these inventions and tools based on accelerators our modern digital life consisting of computers, smartphones, internet, GPS, etc. would be obsolete and we would probably live in a steam punk like world.

Over the last decades the maximum attainable particle energy has been steadily increased. Today's accelerators often use resonant cavities, in which electromagnetic fields form a standing wave. The cavities are designed in a way, that the particles passing trough them always see the electric field at the right phase in order to get accelerated. The electric field in cavities is limited by the occurrence of electric breakdown inside the cavity.

The maximum achievable electric fields prior to breakdown depends on the frequency of the electric field. The maximum obtainable electric field E can be estimated via the empirically found relation [11, 12]:

$$\nu = 1.64 \; MHz \cdot \left(\frac{E}{E_0}\right)^2 \cdot e^{-8.5\left(\frac{E_0}{E}\right)} \tag{1.2}$$

with:

$$E_0 = 1 \; \frac{MV}{m} \tag{1.3}$$

Equation (1.2) is known as Kilpatrick limit. Figure 1.1 shows the graph obtained by eq. (1.2) and the operating points of CERN and the European

---

[1]From time to time there are reports on super-luminescent velocities in literature. Sometimes these are faulthy measurements as e.g., in the case of super-luminescent neutrinos [4]. Sometimes super-luminescent speeds are encountered due to questionable interpretations of experimental results [5]. A very nice demystifying publication for such a kind of experiments is given by [6], in which apparently super-luminescent velocities are demonstrated only by the use of standard electronic components.
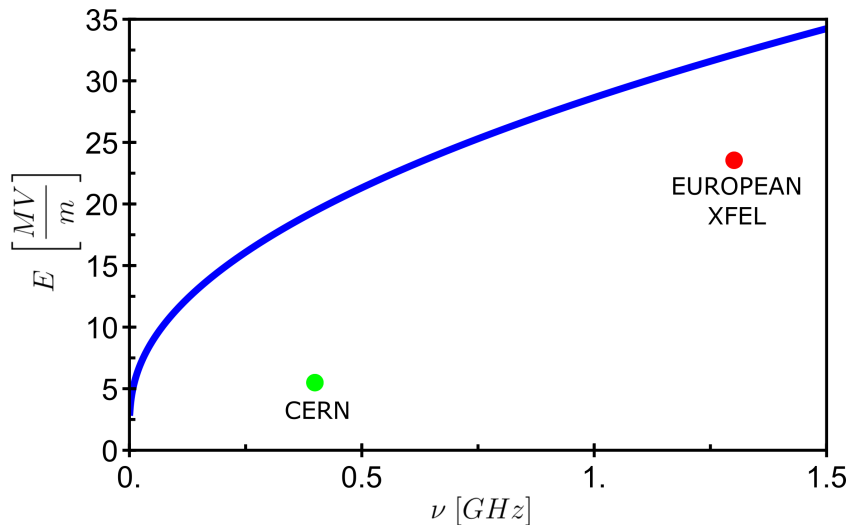
Figure 1.1: The blue line shows the Kilpatric limit. In regions above the blue line electrical breakdown occurs. The green and red dot indicate the operation points of CERN and the European X-Fel respectively.

X-FEL. Recalling that the length of the free electron lasers nowadays amount to more than three kilometers [13, 14], there is definitively an economic pressure to develop new methods to accelerate electrons harder and hereby more efficient in future accelerators.

One possible option is to go to much higher frequencies e.g., optical frequencies. First proof of principle experiments have shown an accelerating gradient of 25 $\frac{MeV}{m}$ [15]. The miniaturization limited the energy gain to a few $100\ eV$ at the moment.

A second possibility is to ignore the assumptions of the Kilpatric limit completely and allow breakdown to happen during the acceleration process. Since plasmas are already 'broken' they are able to sustain extremely high field strengths. The main idea is to go to non equilibrium physics on extremely short timescales.

Particle acceleration in plasmas resembles a new method to deliver energetic particles. Laser-plasma-accelerators (LPAs) use energetic short pulse

laser systems, which are focused to a few μm^2. The electric field in such a laser amounts up to several $\frac{TV}{m}$. Unfortunately these fields oscillate transversely with PHz frequency. All LPAs have in common that they convert, in one way or the other, the transverse oscillatory fields into a quasi static longitudinal field.

LPAs have unique properties and to a certain extent resemble complementary concepts to existing accelerators. LPAs are commonly divided into two groups. Depending on the density of the target, the laser light can propagate through the plasma or it is reflected from the plasma. The first case is called an under-critical plasma the second is referred to as an over-critical plasma.

Under the right conditions one can drive a density modulation in the electron distribution of a gas via the laser. This density modulation moves with the group velocity of the laser. Due to the ionic background of the plasma strong electric fields built up. In these co-propagating quasi-static electric fields electrons can be accelerated efficiently. Gas targets typically have an longitudinal extension of a few mm up to a few cm. Due to the under-critical nature of the plasma the laser interacts in a volumetric fashion.

Solid state targets are used to accelerate protons and ions. Today's laser systems are not intense enough to couple directly to protons. This inhibits the use of wake fields to accelerate protons/ions with presently available laser systems. Laser-ion-acceleration is always an indirect acceleration process. In a fist step energy is transferred onto electrons, which then couple onto the ions. This typically happens at a plasma vacuum border. Electrons leaving the plasma set up strong charge separation field. Protons and ions are accelerated in this quasi-static electric field. Since the plasma is over-critical the laser can only interact with the surface of the target, ergo electrons, which are situated before or near the critical density.

If one divides the field of laser-plasma acceleration in the presented manner, it stands out, that next to the density also the target size is varied. By

decoupling target size and target density, on obtains four different interaction scenarios:

Large targets $d \gg \lambda$ with high electron density $n_e > n_c$ are used in the field of warm dense matter. Warm dense matter resembles the link between solid state and plasma physics.

Large targets $d \gg \lambda$ with low electron density $n_e < n_c$ are used for electron acceleration via wake fields.

Small targets $d \approx \lambda$ with high electron density $n_e > n_c$ are used for proton and ion acceleration.

Small targets $d \approx \lambda$ with low electron density $n_e < n_c$ resembles widely uncharted terrain, in which the presented work takes place.

The last case is poorly studied in theory and experiment, not due to the fact that it is not interesting. The reasoning behind this is quite simple. Its just extremely challenging to produce such targets with today's technology in comparison to the targets used in the first three cases.

This work describes one of the first experiment which falls into the 4th category with $d \approx \lambda$ and $n_e < n_c$. Wavelength sized spheres were used as targets. For targets with such small dimensions any kind of support would alter the laser-plasma interaction significantly. The smallest available supports structure for targets constitute glass capillaries with approximately 1 μm diameter [16] or spider silk [17] with similar dimensions. It is obvious that it makes no sense to mount a wavelength sized target via these state of the art methods. A possible solution to this problem constitutes the removal of any mounting and use a levitated target instead. To achieve this, a Paul trap, designed to trap wavelength sized spheres, was developed. By the use of a electro-optical damping system the targets can be positioned in the focus of a high intensity laser with sub-micrometer accuracy. The experiments were conducted at the PHELIX laser located at GSI in Darmstadt.
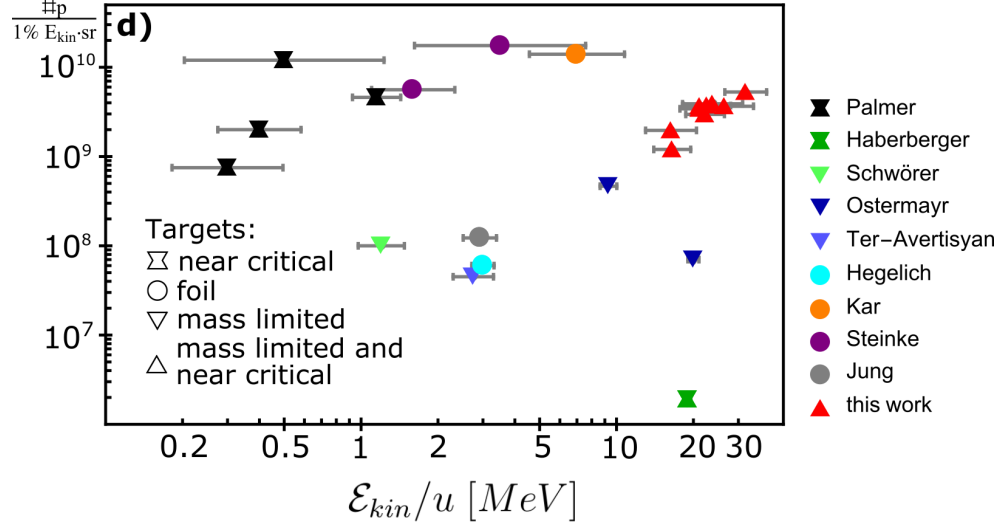
Figure 1.2: Comparison of various experiments yielding mono-energetic proton/ion spectra [1, 19–27]. The symbols represent different target systems. The error-bars depict the FWHM of the proton/ion distribution.

Previous experiments at PHELIX employing foil targets with similar longitudinal dimensions yielded exponentially decaying energy spectra with a distinct high energy cutoff [18]. Such spectra are commonly encountered for an acceleration mechanism called target normal sheet acceleration (TNSA) (see section 2.2.1). For spherical targets with comparable diameters one naively would expect similar energy spectra. Instead a mono-energetic spectrum was recorded in each shot. Target geometry and altered pre-expansion were identified to be responsible that no TNSA like acceleration took place. The sub-focus sized spherical target undergoes a stronger pre-expansion in comparison to thin foil targets. In the resulting still sub-focus sized undercritical plasma, a volumetric acceleration mechanism takes place. The experiment and their interpretation were published in [1].

Figure 1.2 shows previous experiments in which mono-energetic proton beams were recorded in comparison to the results obtained in this work. In the past different target systems were used to achieve mono-energetic

ion beams. The different approaches are marked by individual symbols in fig. 1.2. Cross shaped symbols represent experiments, which use near-critical gas target at CO_2 laser systems [19, 20]. Circles depict experiments which use thin foils as targets [24–27]. Pointing down triangles used spherical solid targets (such as e.g., droplets) [21–23]. The result of this work are represented via upright red triangles, where a sub-focus sized under-critical target was used [1]. The ion energies for such a target system are considerably higher compared to all previous experiments. Also the spectral bandwidth is smaller compared to experiments which yielded similar count rates. Finally it shall be highlighted, that the energy spectra in this work exhibit no exponential background signal compared to all other experiments shown in fig. 1.2. This evidences, that in previous experiments different acceleration mechanisms competed with TNSA like acceleration. The data obtained form sub-focus sized near-critical targets shows a clear signature of a volumetric acceleration mechanism without any TNSA contribution.

Chapter 2

Theory

Nature is complex. Physicists use models to describe nature. One of the main task of physicists is the choice of appropriate theoretical 'tool'/model in accordance to problem under investigation. To calculate the trajectory of a soccer ball one could use special relativity, quantum mechanics or Newtonian mechanics. All results obtained by these different approaches would be extremely similar. In the limit of small velocities special relativity and Newtonian mechanics are equivalent. The same holds for large objects in quantum mechanics, here also Newtonian mechanics is applicable. In a philosophical sense the results obtained by special relativity and/or quantum mechanics would be closer to an universal truth, than the results obtained by Newtonian mechanics. Unfortunately these results would be lengthy and rather complex. The treatment via Newtonian mechanics is much easier.

The simpler formalism helps the physicist to acquire an physical intuition for the treated problem faster compared to the use of formalisms with higher complexity. Therefore every decent physicist would not hesitate, to use Newtonian mechanics to calculate the trajectory of a soccer ball. Nevertheless this simplification is not free of charge. One always must keep in mind what were the taken assumptions, do they still hold for the new parameters, how big is the error compared to a more sophisticated and complex model. So

he can only extrapolate the obtained results according to the validity of the employed theory. Mostly the question regarding the validity is answered by experience, intuition and back on the envelope calculations.

Many-body physics inherently tend to be complex due the large amount of interacting particles. This circumstance leads to a plethora of physical effects such as fluid dynamics [28], theory of gases [29, 30], equation of state for stars [31, 32], plasma physics [33, 34], and so on, just to name a few.

LPAs use properties of charged many body systems to accelerate particles such as electrons or protons/ions to high energies. Today's LPAs can accelerate electrons onto a few GeV [35–37] over just a few centimeters. Protons can reach energies close to $100 MeV$ [18, 38]. The large parameter space based on different driving lasers and various targets systems enables the investigation of many different effects and acceleration mechanisms.

In the spirit of the first paragraph some models and concepts suitable to describe laser-plasma based accelerators will be presented in the next sections of the theory chapter.

One of the most important concepts in LPAs is the ponderomotive force. Therefore ponderomotive forces are discussed in great detail in section 2.1. In section 2.1.1 the one-dimensional ponderomotive force is derived. The ponderomotive force for relativistic light fields is presented in section 2.1.3.

The effects of higher dimensionality is presented on the example of an two-dimensional Paul-trap in section 2.1.2.

Section 2.2 describes various standard methods to accelerate ions via strong laser pulses. The selected acceleration mechanism illustrate the differences between surface dominated acceleration and volumetric acceleration mechanisms. Section 2.2.1 describes a surface acceleration mechanism called target normal sheet acceleration (TNSA). A semi-volumetric acceleration is the so called hole boring acceleration (HB) which is described in section 2.2.2. Radiation pressure acceleration (RPA) and coulomb explosion (CE) are examples for volumetric acceleration. They are described in section 2.2.3 and

section 2.2.4.

TNSA, HB and RPA are only described in a schematic way to illustrate the underlying physical concepts and ideas. CE is treated with much more detail. Not due to the fact that CE is an important accelerating mechanism, rather than due to its simplicity. The rigorous analytical treatment of CE's gives interesting insights into systems consisting of many charged particles.

Imperfect laser contrast can alter the target properties due to pre-plasma formation and subsequent expansion prior to the main laser pulse. Some physical concepts, which are encountered in pre-plasmas and special aspects of pre-plasma dynamics in the case of sub focus sized MLTs are discussed in section 2.3.

In the presented experiment the transmitted and reflected light were recorded. The transmitted light was essential for the characterization of the pre-plasma expansion via in-line-hologrphy. Section 2.4.1 describe the concept of in-line-holography (ILH). For the reflected light, the concept of the relativistic mirror is introduced in section 2.4.2.

2.1 Ponderomotive Forces and Secular Motion

The dynamics of charged particles in oscillating electromagnetic fields can be rather complex due to the high frequency terms in the corresponding differential equations. The concept of ponderomotive forces (PF) and ponderomotive potentials (PP) helps to simplify these kind of problems.

In the context of this work the PP and the corresponding forces are of uttermost importance. A Paul trap was used to levitate microscopical particles which subsequently served as targets for laser-plasma acceleration experiments. The whole trapping dynamics of Paul traps is fully based on PFs (see section 2.1.2). The trapped particles were consequently irradiated by a high power laser to accelerate protons and ions. Due to the oscillatory nature of electromagnetic waves PFs quite naturally play an important role in the description of such kind of interactions.

Trajectories of charged particles in electromagnetic fields can be obtained by direct integration of the Lorenz force F_L :

$$\vec{F}_L = \frac{d\vec{p}}{dt} = q \cdot (\vec{E} + \vec{v} \times \vec{B}) \qquad (2.1)$$

Unfortunately this set of differential equations can only be solved analytically for a few selected cases. Often electromagnetic fields $\vec{E}$ and $\vec{B}$ exhibit spatial and temporal dependencies, which render the analytical solutions, if present at all, extremely complex. Under certain conditions the trajectory of a charged particle in a inhomogeneous oscillatory field can be decomposed into slow and fast varying parts:

$$\vec{r} = \vec{\mathfrak{R}} + \vec{\xi} \qquad (2.2)$$

The hereby necessary constraints are summarized and discussed at the end of section 2.1.1. $\vec{\mathfrak{R}}$ is called secular motion. $\vec{\mathfrak{R}}$ represents the average drift

motion of the charged particle. The term secular motion has its origin in astrophysics, where it is used to describe long term motions and drifts of celestial objects e.g., the axial precession of the earth ($25800\ a$). $\vec{\xi}$ represents the oscillatory motion at higher frequencies e.g., the annual motion of earth around the sun.

In electrodynamics, the quiver motion $\vec{\xi}$ is the solution of eq. (2.1) in zeroth order. Ergo the situation without local and temporal gradients in the electromagnetic fields. Subsequently the time average of $\vec{r}$ over one oscillation period is then just the secular motion.

$$\langle\, \vec{r}\, \rangle_t = \vec{\mathfrak{R}} \tag{2.3}$$

In Paul trap literature $\vec{\mathfrak{R}}$ is mostly referred to as macromotion, whilst $\vec{\xi}$ is called micromotion [39, 40].

The underlying idea of the ponderomotive concept is the definition of a pseudopotential Φ_p which only describes the secular motion $\vec{\mathfrak{R}}$, ergo averaging over the highly oscillating parts $\vec{\xi}$ of the motion. This concept dates back to Kapitza and Dirac who investigated the scattering from electrons on a standing light wave [41].

At the end of their paper Kapitza and Dirac propose an experimental setup based on 'state of the art technology'. It took more than half a century, before the experiment was finally realized [42, 43]. Maybe this historic example can serve as a warning for future generations, when reading or writing a phrase in the spirit of: 'With present day technology ...' or 'With soon available high power laser systems ...'.

In section 2.1.1 the one-dimensional non relativistic ponderomotive potential and force is derived, based on their work cited by [40, 44]. Generalizations regarding higher dimensions and aspects relating to relativistic effect, as encountered in high intensity laser-plasma experiments, will be discussed in sections 2.1.2 and 2.1.3.

The ponderomotive concept is often treated rather sloppy in literature,

since it only represents an averaging in time. For example the corresponding constraints, under which the ponderomotive concept is still valid, are often insufficiently discussed in corresponding literature. Sometimes these constraints are not mentioned at all [45]. The inversion of the ponderomotive force depending on the laser intensity as described in [46] is rather attributed to a violation of fundamental assumptions. The same holds for the uphill acceleration presented in [47] (see also section 2.1.3).

Another still ongoing discussion is the question regarding the polarization dependency of the ponderomotive force. The extraction of electrons out of the focal region of a high power laser due to the ponderomotive force was experimentally investigated in [48]. Two comments indicated that the ponderomotive force should be radial symmetric [49, 50]. A reply by the experimentalist states a clear polarization dependency by experimental proof [51]. Hopefully this work will be able to shed some light onto this still ongoing debate.

2.1.1 One-Dimensional Non-Relativistic Ponderomotive Force and Secular Motion

Starting with an one-dimensional electric field composed of static and oscillatory components:

$$E = E_0 + E_\omega \cos(\omega t) \tag{2.4}$$

Herby E_0 and E_ω are the amplitudes of static and oscillatory electric fields. Both amplitudes may exhibit spatial dependencies. Taylor expanding the equation of motion in ξ and only keeping the first oder terms results into:

$$\frac{d^2\mathfrak{R}}{dt^2} + \frac{d^2\xi}{dt^2} = \frac{q}{m}\left[E_0 + \xi\frac{dE_0}{dr} + E_\omega\cos(\omega t) + \xi\frac{dE_\omega}{dr}\cos(\omega t)\right] \tag{2.5}$$

The 'trick' is to solve the differential eq. (2.5) for the fast oscillating and smooth varying terms separately. For the fast terms one obtains:

$$\frac{d^2\xi}{dt^2} = \frac{q}{m}E_\omega \cos(\omega t) \tag{2.6}$$

with the solution:

$$\xi = -\frac{q}{m}\frac{E_\omega}{\omega^2}\cos(\omega t) \tag{2.7}$$

ξ represents the high frequency oscillatory motion. The amplitude of this quiver motion is directly proportional to the field amplitude E_ω . In the case of a Paul trap the micromotion vanishes in the trap center (see also [52–57]). Substituting eq. (2.7) into eq. (2.5) and averaging over one oscillation period leads to:

$$m\frac{d^2\mathfrak{R}}{dt^2} = qE_0 - \frac{q^2}{4m\omega^2}\frac{dE_\omega^2}{dr} \tag{2.8}$$

Equation (2.8) can be interpreted as the equation of motion for the secular motion $\mathfrak{R}$. By integration of eq. (2.8) one obtains the effective potential:

$$\Phi_{eff} = \Phi_0 + \frac{q}{4m\omega^2}E_\omega^2 \tag{2.9}$$

Equation (2.9) reveals that the obtained effective potential Φ_{eff} is composed out of two parts. The first term is the classical electrostatic potential Φ_0. The second term originates due to the inhomogeneity of the time dependent electric field and is called ponderomotive potential given by:

$$\Phi_p = \frac{q}{4m\omega^2}E_\omega^2 \tag{2.10}$$

There exist solutions for Φ_p which aren't a solution of Maxwell's equations, e.g., potentials with a local minimum (see section 2.1.2). Therefore Φ_p is often referred to as pseudo potential. Nevertheless Φ_p behaves mathematically like every other conservative potential. It obeys the superposition principle as

seen in eq. (2.9). The corresponding ponderomotive force F_p is given by:

$$F_p = -q\frac{d\Phi_p}{dr} = -\frac{q^2}{4m\omega^2}\frac{dE_\omega^2}{dr} \tag{2.11}$$

One interesting aspect of the ponderomotive force is, that it has the same value and direction for positive and negative charges. In the same field configuration electrons and positrons experience the same ponderomotive force, since F_p is proportional to q^2. This might seem anti-intuitive at first glance. Indeed by changing the sign of the charge, the phase of the micro motion ξ differs by π. To obtain eq. (2.6) one averaged over the complete oscillation period, which implies no overall effect due to the different sign in the phase.

Another noteworthy feature of the ponderomotive force is, that it points towards regions of decreasing field amplitudes E_ω. Heuristically this can be motivated in a simple thought experiment. The setup consist out of an electron situated on the axis of a weak laser beam with Gaussian envelope in space. Due the electric field of the laser, the electron will experience a force away from the laser axis. The electron moves into regions with smaller field amplitudes. After some time the field changes sign, and the electron will experience a force towards the laser axis. This restoring force is slightly smaller than the expelling force, since the electron is now located in a region with smaller field amplitude. Ergo with every oscillation period of the field the electron is moved away from the laser axis towards field free regions.

The time averaged kinetic energy of the quiver motion is given by:

$$\mathcal{E}_{quiver} = \langle\, \mathcal{E}_{kin}\, \rangle_t = \left\langle\, \frac{1}{2}m\dot{\xi}^2 \,\right\rangle_t =$$

$$\frac{q^2 E_\omega^2}{2m\omega^2} \frac{\int_0^{\frac{2\pi}{\omega}} |\sin^2(\omega t)|dt}{\int_0^{\frac{2\pi}{\omega}} dt} = \frac{q^2 E_\omega^2}{4m\omega^2} \tag{2.12}$$

By comparison with eq. (2.10) it is found:

$$\mathcal{E}_{quiver} = q\Phi_p \tag{2.13}$$

Equation (2.13) can be interpreted as 'inner ponderomotive energy' of a particle. When a particle runs down the ponderomotive potential the 'inner ponderomotive energy' stored in the micro motion is converted into kinetic energy of the macro motion. Therefore $\mathcal{E}_{quiver}$ is also often called ponderomotive energy.

The efficient absorption of light by a plasma is one key requisites of TNSA. Almost all collisionless absorption mechanisms in laser-plasma interactions rely on the fact, that the light field is decoupled from the electrons in one way or the other (see section 2.2.1). For example this can happen on a step like plasma profile or in a plasma gradient. The presence of electron densities larger than the critical density n_c is of vital importance for different laser absorption mechanisms. In the case of a steep plasma profile the electron temperature/energy is defined by the $\mathcal{E}_{kin}$ of the ensemble. In the case of a plasma gradient the final electron energy will be defined by poderomotive potential. Equation (2.13) would indicate the equality of both scenarios regarding the electron temperature, similar to the ergodic hypothesis. This picture unfortunately is to simplistic. Plasma gradients can lead to a field swelling of the incoming radiation due to the optical properties of the plasma (see also sections 2.3.3 and 2.4.1). The same laser parameters lead to different quiver energies. Here only a single particle picture is discussed. Many particle systems can alter the scenario. Nevertheless the ponderomotive energy of a single particle delivers a good order of magnitude approximation for the electron temperature in a laser-plasma interaction (see also section 2.2.1).

The presented derivations for the PF and PP are only valid under certain conditions which will be summarized and discussed in the following paragraphs.

The decomposition according to eq. (2.2) was used to solve eq. (2.5).

This is only possible under the assumption, that the amplitude of ξ is small
compared to the scale length of the inhomogeneity of the electric field. From
eq. (2.5) it follows directly:

$$E_\omega \gg \xi \cdot \frac{dE_\omega}{dr} \tag{2.14}$$

Inserting eq. (2.7) into eq. (2.14) leads to:

$$\frac{q}{m\omega^2} \cdot \frac{dE_\omega}{dr} \ll 1 \tag{2.15}$$

Another possible formulation of this constraint is often used in literature [47]:

$$\xi \ll \mathfrak{R} \tag{2.16}$$

$$\dot{\xi} \gg \dot{\mathfrak{R}} \tag{2.17}$$

Unfortunately eqs. (2.16) and (2.17) represent a circular statement, since
they already imply the possible decomposition of the trajectory according
to eq. (2.2). Nevertheless for systems governed by ponderomotive forces
eqs. (2.16) and (2.17) have to be fulfilled. If one knows the complete trajec-
tory of a particle one can judge via eqs. (2.16) and (2.17), if the governing
force is ponderomotive in nature or not.

   To obtain eq. (2.7) it was assumed, that the particle velocity is non rel-
ativistic. If the particle speed approaches the speed of light, the amplitude
of the micromotion will no longer be proportional to the electric field. The
relativistic increase of the particle mass indeed limits the amplitude of the
particle trajectory. Via the c -barrier an upper limit for the amplitude can
be estimated to $\frac{c\pi}{\omega}$. As described earlier the micromotion ξ samples the field
inhomogeneity. With smaller sampling region the ponderomotive force will
act weaker than suggested by eq. (2.11).

   If one wants to investigate the ponderomotive force onto an electron in a
light field one also has to account for the magnetic field. The magnetic field
amplitude in a electromagnetic wave amounts to $B_0 = \frac{E_0}{c}$ (see section 2.1.3).

Ergo if the particle only reaches velocities much smaller than c one can neglect the contribution of the magnetic force.

In section 2.1.3 the dimensionless amplitude a_0 is introduced. It defines the critical intensity, which allows to distinguish two different regimes. For values $a_0 \ll 1$ the magnetic contribution to eq. (2.1) can be neglected, here one can make use of the non-relativistic force as derived in this chapter. For values $a_0 \gg 1$ the electron velocity approaches relativistic velocities and the ponderomotive force has also a component along the pointing vector.

2.1.2 Ponderomotive Forces in 2D Quadrupole Traps

In this work a Paul trap was used to position microscopic spheres inside the focus of a high power laser. Paul traps use ponderomotive forces to generate a (pseudo-)potential minimum. In section 2.1.1 the one-dimensional ponderomotive force is derived. The effects of higher dimensionality for ponderomotive forces will be discussed in this section on the example of a two-dimensional Paul trap.

The electric field of an ideal linear Paul trap is given by:

$$\begin{pmatrix} E_x \\ E_y \\ E_z \end{pmatrix} = A \cdot \begin{pmatrix} x \\ -y \\ 0 \end{pmatrix} \cdot \cos(\omega t) \qquad (2.18)$$

with amplitude A and angular frequency ω.

The electric field is shown schematically fig. 2.1. The electric field has the structure of a quadrupole. The amplitude of the electric field decreases linearly with the radius. This follows directly from eq. (2.18).

The trajectories for two particles with different starting positions are shown in Figure 2.1. The amplitude and frequency of the trap voltages and the charge to mass ratio of the particle were chosen in such a way to obtain $\mathfrak{q} = 0.064$. The dimensionless $\mathfrak{q}$ - parameter is defined and discussed in [52–57]. $\mathfrak{q} \leq 0.4$ implies that the conditions necessary for a conservative
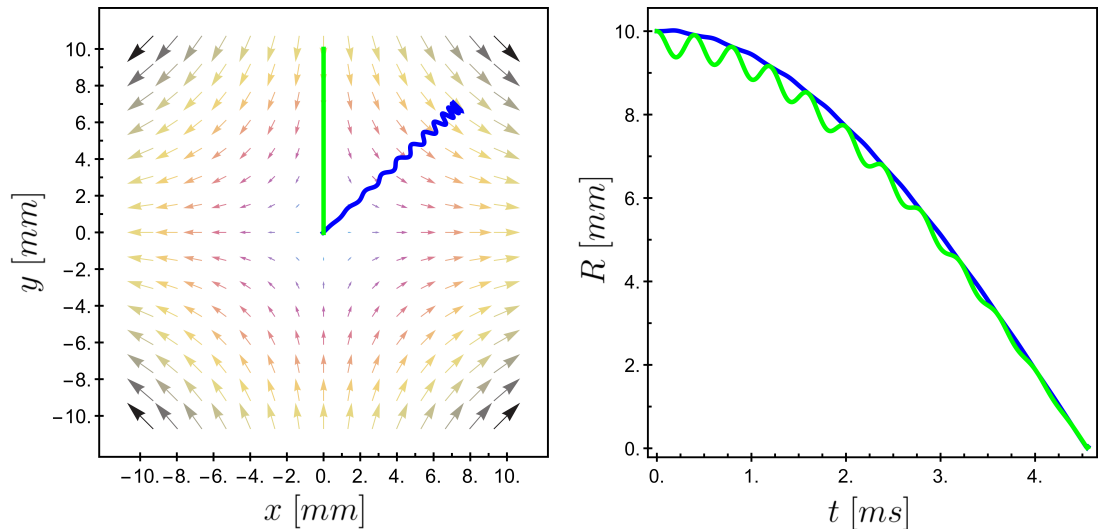
Figure 2.1: Trajectories of two particles in a Paul trap.

pseudo-potential are fulfilled. The used values for this simulation were: $\omega = 2\pi\ 2.5\ kHz$, $r_0 = 10\ mm$, $\Phi_{PT} = 4\ kV$, $\frac{q}{m} = 0.1\ \frac{C}{kg}$. The simulation was stopped when the particle reached the trap center.

The green trajectory shows a particle, which starts on the axis between two electrodes. It looks exactly like the one dimensional case. The particle exhibits a radial quivermotion and is accelerated to the trap center.

The blue trajectory shows a particle, which starts between two electrodes. The equations of motion for the particle exhibit a coupling between the different coordinates. One might think that the micromotion now can be described by the superposition of two ponderomotive potentials, one for each component (see eq. (2.9)). Even if this concept delivers the right result, it is worth to look into this question in more detail, since eq. (2.9) was derived for a one-dimensional case.

The particle starting between the electrodes also experiences a macromotion towards the trap center (a necessary requisite for a trap) like in the case of the green trajectory. But now the micromotion is perpendicular to the drift motion. This is a direct result due to the fact, that the micromotion in

x and y have a phase difference of π. This fact alters the microscopic interpretation of the particle trajectory. While the green trajectory samples the electric field gradient, the blue curve samples the curvature of the electric field. They lead to the same time averaged radial force but have different physical reasons.

This difference becomes clear in a simple mind experiment. In an infinitely large trap the quivermotion would run into the c-barrier for large radial distances. As stated in section 2.1.1 the ponderomotive force for the particle with the green trajectory will get smaller since a smaller region of the linear field gradient is sampled. The particle with the blue trajectory samples the curvature of the electric field. The radial force has its origin in the decomposition of the electric field into radial and tangetial components. The radial force is largest at the turning points and zero in between. Ergo the c-barrier would diminish the ponderomotive force stronger than in the case of the particle with the green trajectory. This fact can easily be shown in computer simulations, which involve Paul traps with the size of the solar system and electrostatic fields of several E_{crit}.

Finally it can be stated that in the case of a two dimensional Paul trap the ponderomotive force is radial symmetric:

$$F_r = -\frac{q^2}{4m\omega^2}\frac{dE_\omega^2}{dr} \tag{2.19}$$

This result is a direct consequence of the investigated field geometry. The subtle differences, in the origin of the ponderomotive force in a two-dimensional Paul trap, can be seen as a hint that the pondereomotive force is not necessarily proportional to $\frac{dE_\omega^2}{dr}$. The effect of higher dimensionality for the ponderomotive force is further discussed in section 2.1.3.2.

2.1.3   Ponderomotive Forces in Relativistic Light Fields

According to the Lawson-Woodward theorem [58,59] a free electron interacting with an electromagnetic wave will not be accelerated. Fortunately the Lawson-Woodward theorem is bound to quite a few requisites [60]:

1. the region of interaction is infinite

2. the electromagnetic fields are in vacuum with no walls or boundaries present

3. the electron is highly relativistic and moves into the direction of the radiation

4. no static electric or magnetic fields are present

5. nonlinear effects (e.g., ponderomotive and radiation reaction forces) are neglected

To experimentally fulfill all necessary conditions for the application of the Lawson-Woodward theorem in a real world experiment would actually resemble a great challenge. But fortunately this effort is not necessary, since one is rather interested in the efficient acceleration of particles via high power laser systems, rather than working on purely academic questions.

Nevertheless it is instructive to start with a thought experiment were the Lawson-Woodward theorem is still fulfilled. By breaking constraints one by one, one can shed light onto various aspects of the underlying accelerating mechanisms. In this work we will concentrate on breaking the Lawson-Woodward theorem via the items 1, 2 and 5.

2.1.3.1   Single Electron Dynamics in a Plane Wave

In relativistic laser-plasma physics typically a strong laser pulse interacts with some kind of target. The resulting extremely energetic many body

systems are highly nonlinear in nature. This non-linearity in combination with different laser and target parameters lead to a plethora of interesting laser-plasma interactions currently under investigation in many laboratories.

The dynamics of a single charged particle in a plane infinite electromagnetic wave might seem trivial at first sight, compared to the complex collective dynamics of realistic real world laser-plasma interactions. Nevertheless it is one of the few cases, which can be treated rigorously in an analytical closed form, rather than by the implementation of demanding computer simulations. The dynamics of a single charged particle enables the definition of important concepts and scale lengths for relativistic laser-plasma interactions in a natural manner, such as the concept of relativistic intensity and relativistic ponderomotive forces.

Special care was taken to keep the formalism simple. As far as possible results are presented in measurable units such as e.g., time t rather than proper time τ .

Electromagnetic force fields can be expressed by a vector potential $\vec{A}$ in combination with a scalar potential Φ [61]. One has a certain liberty in choosing $\vec{A}$ and Φ , as long as the Lorenz condition given by eq. (2.20) remains fulfilled. This is known under the term gauge freedom.

$$\vec{\nabla} \cdot \vec{A} + \frac{1}{c^2} \frac{\partial \Phi}{\partial t} = 0 \tag{2.20}$$

The observable field quantities $\vec{E}, \vec{B}$ are given by:

$$\vec{E} = -\frac{\partial \vec{A}}{\partial t} - \vec{\nabla} \Phi \tag{2.21}$$

$$\vec{B} = \vec{\nabla} \times \vec{A} \tag{2.22}$$

The potentials of a plane electromagnetic wave traveling in x direction, polarized in y with amplitude A_0 and wavelength λ can therefore be written

as:

$$\vec{A}(\vec{x}, t) = -\vec{e_y} A_0 \sin(\omega\tau + \varphi) \tag{2.23}$$

$$\Phi(\vec{x}, t) = 0 \tag{2.24}$$

The retarded time τ and angular frequency ω are given by:

$$\tau = t - \frac{x}{c} \tag{2.25}$$

$$\omega = kc = \frac{2\pi c}{\lambda} \tag{2.26}$$

c denotes the speed of light. The choice of $\vec{\nabla} \cdot \vec{A} = 0$ and $\Phi = 0$ is refereed to as coulomb gauge. The corresponding electromagnetic fields for a wave polarized in y is given via eqs. (2.21) and (2.22):

$$\vec{E}(\tau) = -\frac{d\vec{A}}{d\tau} = \vec{e_y} E_0 \cos(\omega\tau + \varphi) \tag{2.27}$$

$$\vec{B}(\tau) = \vec{\nabla} \times \vec{A} = \vec{e_z} B_0 \cos(\omega\tau + \varphi) \tag{2.28}$$

With $E_0 = A_0\omega$ and $B_0 = \frac{E_0}{c} = kA_0$.

All the following derivation could also be conducted, by using electromagnetic fields rather than potentials. One only would have to derive the relation of field amplitudes directly out of the Maxwell equations. Here it follows directly out of eq. (2.20). Additionally in the case of linear polarization, the use of potentials helps to keep the equations slender and compact.

The equations of motion for a charged particle (e.g an electron) are obtained by inserting eqs. (2.27) and (2.28) into the Lorentz force eq. (2.1):

$$\dot{p}_x = qB_z\dot{y} = -q\beta_y\frac{dA_y}{d\tau} \tag{2.29}$$

$$\dot{p}_y = q\left(E_y - B_z\dot{x}\right) = -q\left(1 - \beta_x\right)\frac{dA_y}{d\tau} \tag{2.30}$$

$$\dot{p}_z = 0 \tag{2.31}$$

Equations (2.29) to (2.31) would be sufficient to calculate the trajectory of a charged particle in Newtonian mechanics. For scenarios where the particles acquire velocities close to the speed of light, this set of equations is undetermined, since in this case the particle mass depends on its velocity according to special relativity:

$$m = m_0\gamma = m_0\frac{1}{\sqrt{1-\beta^2}} = m_0\sqrt{1 + \left(\frac{p}{m_0 c}\right)^2} \tag{2.32}$$

γ is known as Lorentz factor, m_0 represents the particle mass at rest, also referred to as rest mass. Inserting eq. (2.32) into eq. (2.1) yields after some rearrangement the so called energy equation.

$$\dot{\mathcal{E}}_{kin} = \frac{d(\gamma-1)}{dt}m_0 c^2 = q\vec{E}\cdot\dot{\vec{r}} \tag{2.33}$$

For the considered linear polarized plane wave eq. (2.33) reads:

$$\dot{\gamma}m_0 c = qE_y\beta_y = -q\beta_y\frac{dA_y}{d\tau} \tag{2.34}$$

Equations (2.29) to (2.31) and (2.34) constitute a complete set of equations describing the motion of the particle. In the following steps it is assumed, that the particle is initially at rest and the light pulse is ramped up adiabatically from zero to its final intensity. Hereby the term adiabatic denotes the compatibility with the ponderomotive concept. The encountered constants of integration are chosen according to $r\,(t=0) = \beta\,(t=0) = 0$ and $\gamma\,(t=0) = 1$. This assumption holds for free electrons initially at rest. In the case of field ionization the electron is 'born' into the electric field, ergo the above assumptions do not hold.

By subtracting eq. (2.29) from eq. (2.34) and subsequent integration one obtains the first constant of motion:

$$1 - \beta_x = \frac{1}{\gamma} \tag{2.35}$$

It is interesting to note, that according to eq. (2.35) γ solely depends on β_x and not on β as on might suggested due to eq. (2.32). Equations (2.29) to (2.31) and (2.34) contain two different derivatives (dt and $d\tau$) . Equation (2.25) relates t and τ and with eq. (2.35) results in:

$$\frac{d\tau}{dt} = 1 - \beta_x = \frac{1}{\gamma} \tag{2.36}$$

Equation (2.36) allows to replace γ and t from eqs. (2.29) to (2.31) by τ . Equation (2.30) can then directly be integrated to:

$$\frac{dy}{d\tau} = \frac{-qA_y}{m_0} = ca_0 \sin(\omega\tau) \tag{2.37}$$

with the dimensionless amplitude:

$$a_0 = \frac{qA_0}{m_0 c} = \frac{qE_{rel}}{\omega m_0 c} \tag{2.38}$$

with the relativistic electric field given by:

$$E_{rel} = \frac{\omega m_0 c}{q} \tag{2.39}$$

Inserting eq. (2.37) into eq. (2.29) results into:

$$\frac{dx}{d\tau} = c\frac{a_0^2}{2} \sin^2(\omega\tau) \tag{2.40}$$

Equation (2.31) has the trivial solution:

$$\frac{dz}{d\tau} = 0 \tag{2.41}$$

It is interesting to note, that according to eq. (2.37) the amplitude of y is directly proportional to a_0 . This might seem anti-intuitive since one would expect the amplitude to be limited by the c-barrier. In the same way in

which eq. (2.40) was obtained one gets the corresponding relation for γ :

$$\gamma = 1 + \frac{a_0^2}{2} \sin^2(\omega\tau) \tag{2.42}$$

Averaging over one Period $T = \frac{2\pi}{\omega}$ and using $dt = \left(1 + \frac{1}{c}\frac{dx}{d\tau}\right) d\tau$ from eq. (2.36) one obtains the following expression for the average drift velocity:

$$\langle \dot{x} \rangle_t = \frac{\int \dot{x} dt}{\int dt} = \frac{\frac{ca_0^2}{2}\int_0^T \sin^2(\omega\tau)d\tau}{\int_0^T \left(1 + \frac{a_0^2}{2}\sin^2(\omega\tau)\right) d\tau} = \frac{a_0^2}{a_0^2 + 4} c \tag{2.43}$$

and:

$$\langle |\dot{y}| \rangle_t = \frac{\int \dot{y} dt}{\int dt} = \frac{ca_0 \int_0^{\frac{T}{2}} \sin(\omega\tau)d\tau}{\int_0^{\frac{T}{2}} \left(1 + \frac{a_0^2}{2}\sin^2(\omega\tau)\right) d\tau} = \frac{8a_0}{(a_0^2 + 4)\pi} c \tag{2.44}$$

It is interesting to note, that the electron secular velocity given by eqs. (2.43) and (2.45) is constant in time. The micromotion in x given by eq. (2.40) indicates, that the electron gets accelerated and decelerated in every light cycle. In a simple picture one could argue, that the electron is constantly overtaken by photons. Hereby the electron should get accelerated by scattering events according to the Klein Nishina formula [62].

In other words the radiation force would need to be considered for a full description [63,64]. This implies, that a single electron would not experience any force by the light pressure. Another ultimate limitation is that energy is not conserved i.e. the light field remains constant in strength, regardless of absorption.

In analogy to the calculation of the drift velocity one obtains for a time

averaged γ factor:

$$\langle \gamma \rangle_t = \frac{\int \gamma dt}{\int dt} = \frac{\int_0^T \left(1 + \frac{a_0^2}{2} \sin^2(\omega\tau)\right)^2 d\tau}{\int_0^T \left(1 + \frac{a_0^2}{2} \sin^2(\omega\tau)\right) d\tau} = \frac{3a_0^4 + 16a_0^2 + 32}{8\left(a^2 + 4\right)} \tag{2.45}$$

It is instructive to take a look at the ratio of the time averaged amplitudes of longitudinal and transverse momentum.

$$\frac{\langle |p_x| \rangle_t}{\langle |p_y| \rangle_t} = \frac{\langle |\dot{x}| \rangle_t}{\langle |\dot{y}| \rangle_t} = \frac{a_0 \pi}{8} \tag{2.46}$$

Equation (2.46) shows that for $a_0 \ll 1$ the motion in y dominates, ergo the electron oscillates up and down. For values $a_0 \gg 1$ the longitudinal momentum dominates and the electron drifts along x. This also resolves the problem of the unconstrained amplitude in the y coordinate. For values of a_0 larger than one, the electron starts moving into forward direction. It then experiences the radiation with a redshift due to its longitudinal motion. Due to this redshift no c-barrier is encountered for a free electron in its rest frame.

Equation (2.46) can be used to distinguish relativistic $a_0 \gg 1$ and non-relativistic $a_0 \ll 1$ light fields. Another possible differentiating factor would be $\langle \gamma \rangle_t = 2$, which leads to a similar value of $a_o \approx 1.8$.

Two colliding light fields with the same amplitude and linear polarization can form a standing wave without any magnetic field. The maximum gradient is given by:

$$\frac{dE_\omega}{dr} = \frac{E_\omega \pi}{\lambda} \tag{2.47}$$

With eqs. (2.38) and (2.39) now eq. (2.15) reads:

$$1 \gg 2\pi^2 a_0 \tag{2.48}$$

Equation (2.48) shows that for relativistic intensities in a standing wave the fundamental assumption for ponderomotive forces break down [46, 47].

2.1.3.2 Single Electron Dynamics in Inhomogeneous Light Fields (Relativistic Ponderomotive Force)

Section 2.1.3.1 describes the motion of an electron in a strong plain electromagnetic wave. For inhomogeneous fields relativistic ponderomotive forces will arise. The following heuristic considerations will use a cylindrical symmetric electromagnetic field of the form:

$$\vec{E}_x(\tau, \ r) = a_0 E_{rel} e^{-\frac{\tau^2}{2\sigma_t^2}} \ e^{-\frac{r^2}{2\sigma_r^2}} \cos{(\Omega\tau)} \qquad (2.49)$$

$$\vec{B}_y(\tau, \ r) = \frac{E_x}{c} \qquad (2.50)$$

Obviously eqs. (2.49) and (2.50) do not fulfill the Maxwell equations. A real laser pulse constitutes a much more complicated geometry. So e.g., a Gaussian beam exhibits a divergence and in the case of strong focusing non-neglectable longitudinal fields. Nevertheless such a simplistic case helps to understand the underlying effects.

This 'pseudopulse' interacts with single free electrons initially at rest. Three cases are considered. In the first case, the electron is situated directly on the laser axis. In the two other cases, the electron is displaced slightly from the laser axis along the polarization direction. The numerical integrated trajectories are shown in fig. 2.2. The used values for the simulation are given by: $a_0 = 5$, $FWHM_I = 30 \ fs$, $FWHM_r = 10 \ \mu m$, $\lambda = 1 \ \mu m$. Figure 2.3 shows the corresponding graphs for the γ - factors. Looking at the blue trajectories one sees, that the on-axis electron gets accelerated and decelarated along the pulse propagation direction. After the pulse slipped over the electron the electron is at rest again. The maximum encountered value for γ is in good accordance with eq. (2.42). Even for a moderate intensity of
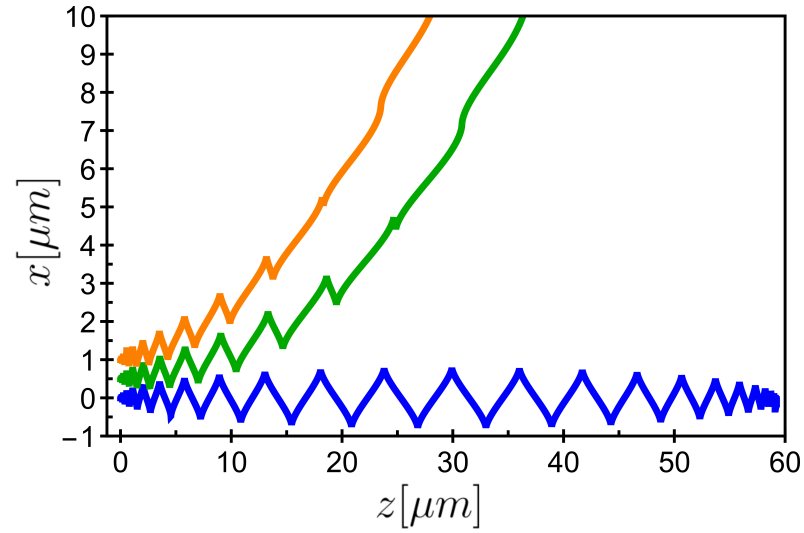
Figure 2.2: Trajectories of free electrons in a 'pseudo' light pulse with Gaussian temporal and spatial profile
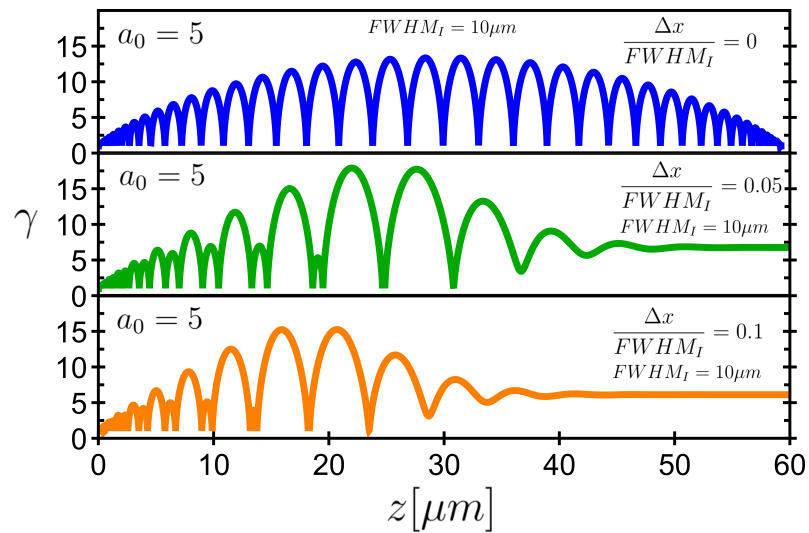
Figure 2.3: Energy of free electrons in a 'pseudo' light pulse with Gaussian temporal and spatial profile

$a_0 = 5$ the displacement is larger than the typical Rayleigh encountered with a short focus (#F2) parabola. One could think that with eq. (2.43) one could integrate over the pulse envelope to obtain the displacement of the electron. But this calculation yields wrong results, which are too small. The reasoning behind that is, that no gradient forces are considered by this approach.

The electrons which are situated slightly off axis are expelled radially. They leave the interaction region approximately after half the pulse passed through the origin. It is interesting to note, that this expelled electrons remain with a final kinetic energy ($\gamma \approx 6$) after the interaction. A direct consequence of the Lawson Woodward theorem. In section 2.1.1 it was stated that quiver energy is converted into kinetic energy when a particle runs down the ponderomotive potential. Here the γ - factor amounts to larger values than for the on axis case. This fact already hints that a relativistic pondero- motive potential is hard to define for relativistic light pulses. This becomes even more evident if one considers the same case with a larger radial gradient. Figure 2.4 shows the graphs for the γ - factors as in fig. 2.3 with a smaller ra- dial extent of the pulse($FWHM_I = 2.5~\mu m$). The positions of the electrons off axis electrons where re-sized by the same amount. One would expect that with higher gradients the particles should experience larger ponderomotive forces. The final kinetic energy of the expelled electrons should be the same compared to the smaller gradient if the one-dimensional equations eqs. (2.10) and (2.13) also hold for higher dimensions.

It is interesting to note that the on axis electron now also gets expelled radially. This is immediately evident by recalling the mind experiment de- scribed in section 2.1.1. For long enough pulses, there is no stable way to oscillate around the axis without experiencing ponderomotive forces, which expel the target. The direction in which the electron is extracted depends on the pulse envelope and the carrier phase envelope. This might come as a surprise, since even for very large pulse durations the carrier phase envelope decides in which direction the particle leaves the high intensity region. The
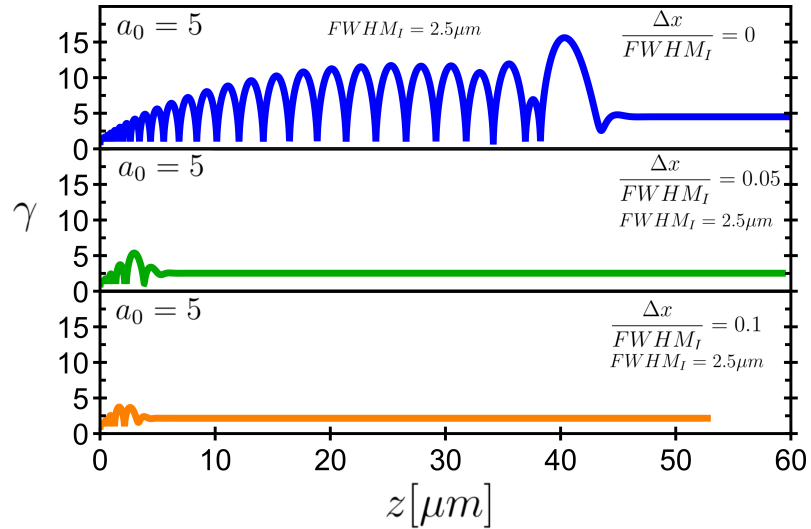
Figure 2.4: Energy of free electrons in a 'pseudo' light pulse with Gaussian temporal and spatial profile

energy is comparable to the energy of the radial expelled electrons in the low gradient case. A second interesting fact is that the off axis electrons exhibit a smaller value for their final γ. This is understood if one assumes two competing ponderomotive potentials. One acting along the polarization, the second one acts along the propagation direction. If the radial ponderomotive force is increased via a larger radial gradients, the longitudinal ponderomotive force can not act as long onto the electrons, as in the low gradient case, since the electrons leave the interaction volume with larger radial velocities.

It is easily shown that the electrons are only expelled along the polarization direction. So one can finally conclude from these heuristic observations that there is no way to define a ponderomotive potential for a laser pulse solemnly by the gradient of a scalar value. Otherwise the force would be radial symmetric. If there exist a ponderomotive potential, it must also exhibit a curl.

2.1.3.3 Single Electron Dynamics in a Plane Wave with a Retaining Field

As shown in section 2.1.3.1 a free electron is accelerated and decelerated in a light pulse due to the relativistic ponderomotive force. In the case of laser ion acceleration electrons are not free. Obviously some electrons can escape the target but the vast majority of the electrons are coupled to a positive charge distribution. This is necessary for laser ion acceleration, since the electrons must transfer their kinetic energy onto the ions. An exception constitutes ion acceleration via a coulomb explosion, which is described in section 2.2.4. For bound electrons the average drift velocity with respect to the ions is zero in first order approximation, since the longitudinal ponderomotive force is balanced by Coulomb retaining fields. In the following derivation the ions are assumed to be immobile.

In section 2.1.3.1 it was assumed that the particle is initially at rest. The resulting trajectory shows a constant drift velocity given by eq. (2.43). This implies the existence of a reference frame were the average drift velocity is zero. Unfortunately by changing the reference frame one also changes the wavelength of the light wave due to the relativistic Doppler shift (see section 2.4.2). For an experimentalist the wavelength constitutes a more or less fixed parameter. One could of course pre-compensate the Doppler shift prior to the Lorentz transformation, which would have to be applied to all results obtained in section 2.1.3.1. A mathematically less cumbersome way is to adapt the constants of integration used in section 2.1.3.1. Instead of $r\,(t=0) = \beta\,(t=0) = 0$ and $\gamma\,(t=0) = 1$ one uses: $r\,(t=0) = \beta_y\,(t=0) = 0$, $\gamma\,(t=0) = \gamma_0 > 1$, $\beta_x\,(t=0) = \beta_{x0} \neq 0$.

Some of the intermediate results are quite lengthy. The final results of these calculations are quite elegant. $\gamma\,(t=0)$ and $\beta_x\,(t=0)$ must be chosen in such a way, to fulfill:

$$\left\langle \dot{x} \right\rangle_t \overset{!}{=} 0 \qquad\qquad (2.51)$$

Equation (2.36) now reads:

$$\frac{d\tau}{dt} = 1 - \beta_x = \frac{C_1}{\gamma} \tag{2.52}$$

With:

$$C_1 = (1 - \beta_{x0})\,\gamma_0 \tag{2.53}$$

β_{x0} and γ_0 depend on v_0 which needs to be chosen in such a way to fulfill eq. (2.51). Equation (2.37) now reads:

$$\frac{dy}{d\tau} = \frac{ca_0}{C_1}\sin(\omega\tau) + C2 \tag{2.54}$$

Due to $\beta_y\,(t=0) = 0$ it follows $C_2 = 0$. Equation (2.40) is now given by:

$$\frac{dx}{d\tau} = \frac{a_0^2 c}{2C_1^2}\sin^2(\omega\tau) + \frac{C3}{C1} \tag{2.55}$$

With:

$$C_3 = \gamma_0 v_0 \tag{2.56}$$

Similar to eq. (2.43) one can now derive a drift velocity in dependency of v_0 :

$$\langle\,\dot{x}\,\rangle_t = \frac{\int \dot{x}dt}{\int dt} = \frac{\frac{ca_0^2}{2C_1^2}\int_0^T \sin^2(\omega\tau) + \frac{C_3}{C_1}d\tau}{\int_0^T \left(1 + \frac{a_0^2}{2C_1^2}\sin^2(\omega\tau) + \frac{C_3}{C_1}\right)d\tau} =$$
$$\frac{\left(a_0^2\,(c + v_0) + 4v_0\right)c}{\left(a_0^2 - 4\right)v_0 + \left(a_0^2 + 4v_0 + 4\right)c} \overset{!}{=} 0 \tag{2.57}$$

The drift velocity for arbitrary initial v_0 reads:

$$\langle\,\dot{x}\,\rangle_t = \frac{a_0^2 c^3 + 4\gamma_0^2 cv_0\,(c - v_0)}{a_0^2 c^2 + 4\gamma_0^2\left(c^2 v_0 - cv_0^2 + (c - v_0)^2\right)} \tag{2.58}$$

For the required zero drift velocity one obtains for v_0 :

$$v_0 = -\frac{a_0^2}{a_0^2 + 4} c \qquad (2.59)$$

This result is not really surprising if one recalls the result of eq. (2.43). With the obtained constants of integration C_1, C_2, C_3 and v_0 one sees immediately that the amplitudes of the trajectories given by eqs. (2.54) and (2.55) are now limited for increasing intensities. In contrast to the trajectories of free electrons given by eqs. (2.37) and (2.40), the trajectory now looks like a figure eight. Due to the c-barrier the path length of the figure eight must be smaller than cT . In analogy to eq. (2.42) one obtains:

$$\gamma = \frac{a_0^2}{2C_1} \sin^2 (\omega\tau) + \gamma_0 \qquad (2.60)$$

The γ - factor asymptotically approaches:

$$\gamma \overset{a_0 \gg 1}{\approx} \frac{1}{2\sqrt{2}} a_0 + \frac{1}{\sqrt{2}} a_0 \sin (\omega\tau) \qquad (2.61)$$

In this case γ is always larger than unity, in contrast to the case of a free electron (see fig. 2.5). It is remarkable that in the case of a bound electron the quiver energy of the electron is only proportional to the squareroot of the intensity in comparison to the free electron, where it scales linear with the intensity (see eq. (2.60)). This finding motivates the use of the ponderomotive scaling for the hot electron temperature in TNSA (see also section 2.2.1) and the intensity scaling for RPA (see section 2.2.3).

The calculation of the ratio of the momenta is a little bit more cumbersome than in the case of the free electron movement (see eq. (2.46)). The final result reads:

$$\frac{\langle\, |p_x|\, \rangle_t}{\langle\, |p_y|\, \rangle_t} = \frac{\langle\, |\dot{x}|\, \rangle_t}{\langle\, |\dot{y}|\, \rangle_t} = \frac{1}{2\sqrt{2}} \frac{a0}{\sqrt{2 + a_0^2}} \qquad (2.62)$$

In the case of a free electron the longitudinal momentum dominates for $a_0 > 1$
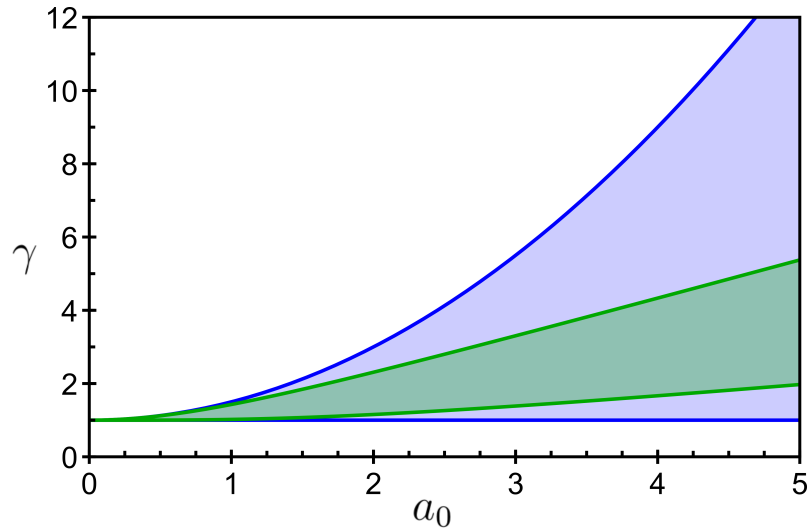
Figure 2.5: The blue shaded area depicts the possible γ - values for a free electron according to eq. (2.42). The green area shows the possible γ - values for an electron with zero drift velocity according to eq. (2.60).

and in a first order approximation the (quiver energy) is stored completely via longitudinal momentum for $a_0 \gg 1$. For a bound electron the ratio of the momenta approach a fixed value for $a_0 \gg 1$. The longitudinal momentum no longer dominates. It is limited roughly to three times the magnitude of the transverse momentum.

2.2   Laser Ion Acceleration

There are many ways to accelerate particles via strong lasers. Particle acceleration via strong laser pulses has been investigated intensively in the last decade. All experiments investigate the interaction of some kind of target with an energetic laser pulse. The goal is to transfer the laser energy onto the desired particles. This can be achieved by many different ways depending on the used target and laser parameters.

Two conceptual different strategies can be identified. One can imagine

that the laser interacts with the target in a coherent/collective manner. This concept dates back to [65]. Plasma based electron accelerators are a prominent example for collective acceleration schemes.

Due to their higher mass and limited laser intensity, ions typically are accelerated via surface acceleration mechanism. The most prominent is called target normal sheet acceleration (TNSA). Hereby the laser raises the internal energy of the target. During the relaxation of the target internal energy is converted to some extend into energetic particles.

Recently the investigation of collective laser ion acceleration schemes has started. Examples for volumetric ion acceleration schemes are hole-boring acceleration, radiation pressure acceleration and the Coulomb explosion.

The presented list of accelerating mechanisms just resembles a small overview and is by far not complete.

2.2.1 Target Normal Sheath Acceleration (TNSA)

Target normal sheet acceleration is a quite extensively investigated laser ion acceleration mechanism(see e.g., [18, 66–70]). Here it will be only described in a heuristic manner to highlight the underlying physics and the properties of ion beams produced via TNSA.

TNSA relies on the generation of a hot electron population via laser absorption. Due to their high conductivity, plasmas can be effectively heated by electromagnetic waves. Laser absorption in plasmas is a rather difficult subject, since it depends on many different parameters such as polarization, angle of incidence, intensity, pre-plasma scale length etc. Many different absorption mechanisms are described in theory such as collisional absorption (see section 2.3.3), resonance absorption [45], vacuum/Brunel heating [71] or relativistic $j \times B$ heating [72]. For intensities $I \gg 10^{18} \frac{W}{cm}$ relativistic $j \times B$ heating dominates [73]. For intensities $I \ll 10^{18} \frac{W}{cm}$ collisional absorption is the most dominant effect [73].

Regardless of the underlying mechanism, a significant portion of the laser

energy is converted into hot electrons [73]. These energetic electrons transverse the target and leave the rear side, where they produce a strong electric sheath field. In this field ions get ionized and subsequently accelerated. It is important to note, that the laser itself is only used as an energy source to generate a hot electron population. There is no light field present in regions were the acceleration actually takes place. This allows for an individual theoretical treatment of laser absorption and acceleration.

There are two main theoretical approaches to describe the acceleration process. In a dynamic approach one tries to describe the resulting plasma expansion via fluid dynamic models [67,74]. Unfortunately these iso-thermal models diverge and lead to infinite acceleration. This shortcoming can be solved by limiting the acceleration time. Experimentally it is found that $t_{acc} = 1.3 \, t_{LASER}$ [75].

An alternative treatment of TNSA approximates the accelerating field as quasi-static and treats the accelerated ions as test particles in this field [76]. These models lead to finite maximum energy. A fundamental assumption is the static nature of the accelerating structure, which doesn't hold for very high intensities (see sections 2.2.3 and 2.2.4).

TNSA delivers high emmittance $\epsilon < 0.01 \, \pi \, mm \cdot mrad$, high current $I > kA$ ion beams with a well defined origin in space an time. The beams exhibit a broad energy spectrum (100 %) and large divergence (ten's of degree). The spectrum has an exponential shape with a distinct cut-off energy. The maximum energy scales with $\sqrt{I}$ [70].

2.2.2 Hole Boring (HB)

TNSA typically takes place on the backside of the target. There are also acceleration mechanisms which take place at the target front side. Hole boring acceleration (HB) is a prominent example [77]. When a laser gets reflected, the target is set into motion due to momentum conservation (see also sections 2.2.3 and 2.4.2). The target surface gets an indention. In a one

dimensional case the momentum conservation reads:

$$\frac{C_1 N h}{\lambda} = mv \tag{2.63}$$

Hereby N depicts the number of photons, h resembles the plank constant, m and v is the accelerated mass and its corresponding velocity. The factor C_1 is a value between one (100% absorption) and two (perfect reflection). Dividing eq. (2.63) by $A\Delta t$ and inserting $m = n_i m_i Al = n_e \frac{A}{Z} m_p A v \Delta t$ for the mass leads to the hole boring velocity:

$$v_{HB} = \sqrt{\frac{2I\mathcal{Z}C_1}{c\mathcal{A}m_p n_e}} \tag{2.64}$$

$\mathcal{A}$ is the mass number, $\mathcal{Z}$ the atomic number. Equation (2.64) shows that HB works best for low density plasmas consisting of low Z material. The plasma should still be over-critical since otherwise the fundamental assumption of momentum transfer due to reflection would be violated. HB has some similarity to a snowplow which accumulates more and more snow in front of the shovel while it moves forward. The kinetic energy of ions generated by HB scales linear with the incident laser intensity. A longer pulse duration does not lead to higher energies since the amount of accelerated ions is proportional to the laser pulse duration.

The experimental maximum observable ion velocity amounts to twice the holeboring velocity [16, 78]. Ions in front of the moving density modulation can get reflected from it. This is analogous to trowing a ball at a wall with speed v. In the rest frame where the thrown ball is at rest the wall moves towards the ball with v and after the reflection from the wall the ball has a speed of $2v$.

The whole derivation was classical, a relativistic treatment of the holeboring is given by [79].

One key assumption in the derivation constitutes the fact that the plasma pressure is neglect able compared to the light pressure. Otherwise a front

side TNSA like expansion would counteract the holeboring process. Since the density modulation grows unbounded with increasing time, there will be always a time where the plasma pressure amounts to such high values that holeboring process comes to rest [80].

Finally it is important to note, that in contrast to TNSA were the laser is only used to generate a hot electron distribution, here the laser actively takes part in the acceleration constituting a more complex situation, where light and plasma are interlinked with each other. For HB a semi-finite plasma extension is assumed. As soon as the plasma is finite the laser can bore through the complete target and one can reach the so called radiation pressure acceleration regime, which is described in section 2.2.3.

2.2.3   Radiation Pressure Acceleration (RPA)

In HB acceleration the target was assumed to be semi infinite. This lead to a intensity depended maximum ion energy. The ion energy does not depend on the pulse duration. During the interaction more and more ions are accelerated onto the HB-velocity. In the case of a finite plasma the pulse can bore through the complete target. From this moment on, the transferred laser energy is distributed onto a limited amount of ions. In this case one would expect to encounter ion velocities, which exceed the HB-velocity. This mechanism is called radiation pressure acceleration (RPA) [81]. RPA represents the volumetric acceleration of a plasma bunch via the radiation pressure of the laser.

When light is reflected form a mirror/target its momentum changes. Due to momentum conservation the target must acquire momentum itself (see also section 2.4.2). This is the basic idea behind radiation pressure acceleration [82, 83]. In a oversimplified version of RPA, photons impinge on the target and the target is set it into motion via momentum transfer. Due to energy conservation the reflected photons have to loose part of their energy and experience a redshift. Momentum and energy conservation are given by:

$$\frac{d\,N}{dt}\left(\frac{h}{\lambda_{in}}+\frac{h}{\lambda_{out}}\right)=\frac{d\,(\gamma v)}{dt}m_T \tag{2.65}$$

$$\frac{d\,N}{dt}\left(hf_{in}-hf_{out}\right)=\frac{d\,(\gamma-1)}{dt}m_T c^2=\frac{d\,\mathcal{E}_{kin}}{dt} \tag{2.66}$$

Hereby h denotes the plank constant. λ and f the wavelength and frequency of the photons. m_T represents the mass of the target. $\mathcal{E}_{kin}$ is the total kinetic energy of the volumetric accelerated target. Even if the microscopic picture of RPA is much more complex in detail, eq. (2.66) helps to gain some insight into RPA. If one wishes to maximize the kinetic energy of individual particles via RPA, eq. (2.66) immediately implies that the target should be as light as possible. But if the target is too small on the other hand, the light pressure will expel all electrons from the target and the target will no longer act as a relativistic mirror (see section 2.2.4), which was the initial taken assumption for the derivation of eq. (2.66). This implies the existence of an optimum target thickness for radiation pressure acceleration were light forces and coulomb retaining forces are balanced [70, 84]:

$$a_0 \approx \pi\sigma = \pi\frac{n_e d}{n_c \lambda} \tag{2.67}$$

d is the thickness of the target. n_e, n_c depict electron density and the critical density. $lambda$ is the wavelength of the light. σ represents the dimensionless areal electron density. A detailed multi-parameter study via 2D PIC simulations yields the following heuristic relation:

$$\sigma \approx 0.4a_0 + 3 \tag{2.68}$$

The laser intensity in the PIC simulations spanned a range from $a_0 = 8.55$ to $a_0 = 85.5$. The difference between eqs. (2.67) and (2.68) is given by the fact, that the PIC simulation accounts for effects like the transmission of light via evanescent waves or relativistically induced transparency.
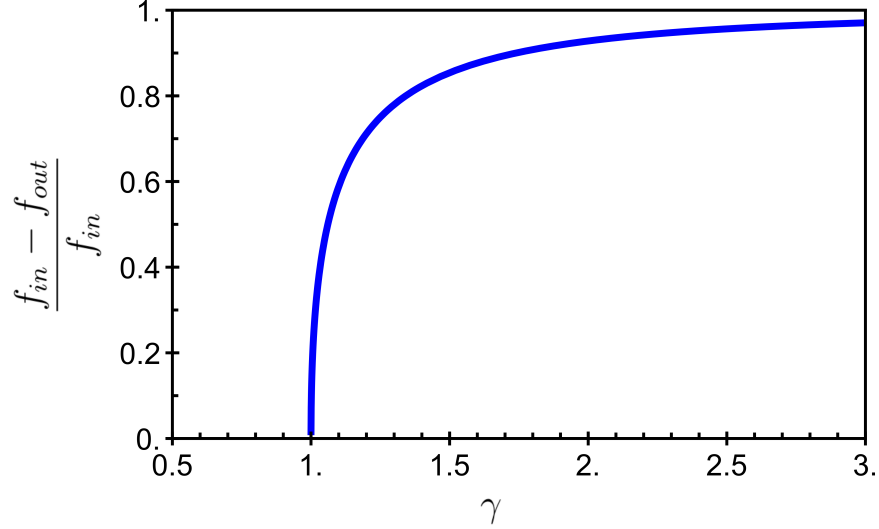
Figure 2.6: Energy transfer between light and a moving mirror

A second consequence which can be drawn from eq. (2.66) is, that the amount of participating photons and their redshift should be as large as possible.In section 2.4.2 the encountered redshift for a reflection from a moving mirror is derived. Equation (2.106) allows to derive a conversion efficiency based on the γ factor of the target:

$$\frac{f_{in} - f_{out}}{f_{in}} = \frac{(1+\beta)^2 \gamma^2 - 1}{(1+\beta)^2 \gamma^2} \tag{2.69}$$

Figure 2.6 shows that in the case of pure reflection, the efficiency of RPA is small for targets with a slow initial velocity. For a conversion efficiency of 50% one needs a target velocity of $\beta \approx 0.3$. For 10% efficiency a value of $\beta \approx 0.05$ is necesarry, which corresponds approximately to the velocity of a proton with 1 MeV. RPA is an efficient acceleration mechanism for large a_0. For low values of a_0 RPA is often overshadowed by other acceleration mechanisms such as e.g., TNSA.

The first experimental results yielding signatures of RPA used circular polarized laser beams in combination with $nm-$ thick targets [16, 26]. The

thickness of the targets demanded a good laser contrast, since the target still should be over-critical during the interaction (see also section 2.3.1). Circular polarization helps to suppress target expansion. Due to the absence of the two ω beating in the electron trajectory for circular polarization electrons are heated less compared to linear polarization (see also section 2.2.1).

In contrast to TNSA in RPA the whole target is accelerated as one single plasma bunch. While TNSA preferably accelerates protons, in RPA all ions acquire a similar velocity. RPA preferably accelerates heavier ions. Most experimental signatures are found in the spectra of heavy ions [16, 25, 26]. RPA represents an intriguing concept. Unfortunately today's lasers are not strong enough to investigate RPA in full detail. This could change in future muli-petawatt facilities such as CALA in Germany [85] or GIST in South Korea [86].

2.2.4 Coulomb Explosion (CE)

In RPA the light pressure is balanced with the electrostatic retaining potential as shown by eq. (2.67). If the intensity is increased even further, one enters the so called blowout regime. In the blowout regime all electrons are expelled from the target and the residual ions undergo a so called Coulomb explosion. Coulomb explosions have been studied extensively in theory and experiment [87–90]. The energy needed to remove all electrons (ideally instantaneously) from the target into infinity is stored as potential energy in the form of electrostatic fields produced by the remaining ionic core (assuming zero kinetic energy of the electrons after their removal). The starting configuration of the ideal coulomb explosion constitutes an extreme state, with maximized potential energy and absent kinetic energy.

It is instructive to consider a simple idealized case to gain some feeling for the process. The ideal one component coulomb explosion of a homogeneous sphere is discussed in section 2.2.4.1. Subsequently section 2.2.4.2 illustrates effects occurring in more realistic scenarios with different den-

sity distributions and multi-species effects. Due to the enhanced complexity
the analytical treatment is replaced by heuristic and numerical approaches.
Section 2.2.4.3 will connect the coulomb regime to the radiation pressure
regime.

2.2.4.1   Ideal CE of a Sphere

Probably the simplest configuration for a coulomb explosion is given by a
homogeneous spherical charge distribution.

$$n_q(r) = \begin{cases} n_{q0} & r \leq R \\ 0 & r > R \end{cases} \tag{2.70}$$

n_{q0} represents the electron number density. By the use of newtons shell
theorem [91] or Gauss's law in combination with the Poisson's equation one
obtains the corresponding potential and electrostatic field:

$$\Phi(r) = \begin{cases} \frac{1}{8\pi\epsilon_0} \frac{Q}{R} (3 - \frac{r^2}{R^2}) + C_1 & r \leq R \\ \frac{1}{4\pi\epsilon_0} \frac{Q}{r} + C_1 & r > R \end{cases} \tag{2.71}$$

$$E(r) = -\nabla U(r) = \frac{1}{4\pi\epsilon_0} \frac{Q_{enc}}{r^2} = \begin{cases} \frac{1}{4\pi\epsilon_0} \frac{Q}{R^3} r & r \leq R \\ \frac{1}{4\pi\epsilon_0} \frac{Q}{r^2} & r > R \end{cases} \tag{2.72}$$

ϵ_0 is the vacuum permitivity, Q denotes the total charge given by

$$Q = \int n_q(r) q \, dV = \frac{4}{3}\pi R^3 n_{q0} q \tag{2.73}$$

while Q_{enc} represents the charge situated at radii smaller than the radial
position r

$$Q_{enc} = \int_0^r n_q(r) q 4\pi r^2 \, dr = \frac{4}{3}\pi r^3 n_{q0} q \tag{2.74}$$

Equation (2.72) shows that the electric field increases linearly from sphere
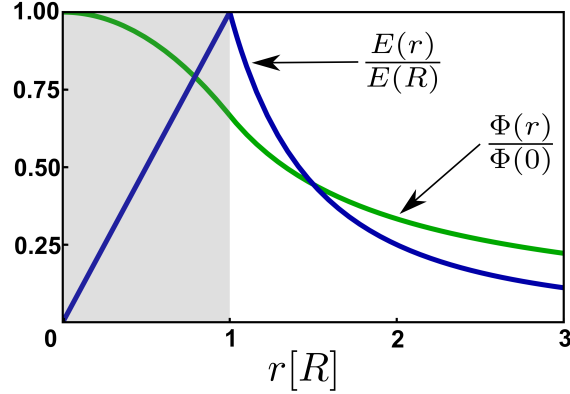
Figure 2.7: Normalized potential and electric field profile for an uniform charged sphere. The values on the abscissa are normalized with respect to the sphere radius R. The shaded area indicates regions inside the sphere.

center to surface. For an one component plasma this implies immediately that individual particles can't overtake each other (see also section 2.2.4.2). Ergo the most energetic particles originate from the sphere surface. By inserting eq. (2.73) into eq. (2.71) with $r = R$ one obtains the maximum obtainable final particle energy:

$$\mathcal{E}_{kin,max} = q^2 \frac{n_{q0}R^2}{3\epsilon_0} \tag{2.75}$$

This equation is also valid in the case of a homogenous multi-species target, when applied to the lightest ion species. The lightest ion on the surface will leave all other ions behind itself, ergo it runs down the complete potential hill like in the case of a single species sphere.

During a Coulomb explosion the complete initial field energy is converted into kinetic energy. This becomes immediately clear in the following thought experiment. Starting with an initially neutral sphere with immobile ions, one has to spend energy to extract the electrons. If one further assumes that the extracted electrons are at rest at infinity conservation of energy dictates that

the work done on the electrons is stored as potential energy in the electric field. The energy inherent to the initial charge distribution is obtained by:

$$\mathcal{E}_{Coulomb} = \frac{\epsilon_0}{2} \int E(r)^2 dV = \frac{4\pi q^2 n_{q0}^2 R^5}{\epsilon_0 15} \tag{2.76}$$

With $dN = 4\pi n_{q0} r^2 dr$ and eq. (2.75) one can obtain the spectrum for an one component Coulomb explosion.

$$\frac{dN}{1MeV 1sr} = \begin{cases} \frac{3\epsilon_0}{2q^3} \sqrt{\frac{3\epsilon_0 \mathcal{E}_{kin}}{n_{q0}}} & \mathcal{E}_{kin} < \mathcal{E}_{kin,max} \\ 0 & \mathcal{E}_{kin} > \mathcal{E}_{kin,max} \end{cases} \tag{2.77}$$

The form of the spectrum is given by a root function with a distinct cutoff at the maximum kinetic energy given by eq. (2.75). Equation (2.75) indicates the possibility to generate highly energetic ions via coulomb explosion. Unfortunately eq. (2.76) shows that the necessary energy to prepare the coulomb explosion scales with $n_0^2 R^5$. For example a proton on the surface of a fully ionized polystyrene sphere with diameter of $1\mu m$ would acquire a final kinetic energy of $0.5 \ GeV$. The energy needed to prepare such system amounts to $8.9 \ J$ (see section 2.2.4.2). This unfortunate scaling is understood immediately due to the fact that the amount of particles with the highest energy grows with R^2.

Equations (2.75) and (2.76) scale quite similar regarding particle density and target size. So there is not much to be gained to reduce the target density and increase the radius or vice versa. This circumstance is often used in PIC codes, where technical constraints can be relaxed by reducing target density and increasing the target thickness by the same amount. Nevertheless it will be shown in the next paragraphs, that it is still worth to explore smaller target densities and why the obove mentioned 'trick' in PIC simulations should be taken with some caution.

Depending on the energy stored in the system one can identify two regimes for the relaxation time. If the particles gain relativistic energies in the in-

teraction the particles will accumulate at the c barrier resulting in a shell structure [92]. The relaxation time in the lab frame will be modified by retardation effects compared by the classical case. To distinguish classical and relativistic coulomb explosion we demand $E_{kin,max}$ defined by eq. (2.75) to be much smaller than the particle rest mass. This results in the following condition for non relativistic coulomb explosions:

$$R \ll \sqrt{\frac{3\epsilon_0 m_q c^2}{q^2 n_{q0}}} \qquad (2.78)$$

One could also demand that the field energy given by eq. (2.76) is less than the rest mass of the complete particle resulting in:

$$R \ll \sqrt{\frac{5\epsilon_0 m_q c^2}{q^2 n_{q0}}} \qquad (2.79)$$

Equations (2.78) and (2.79) are equivalent statements and only differ by a small numerical constant.

Until now the charge distribution was simply defined. The question remains if one can prepare the conditions needed for a relativistic coulomb explosions starting from a neutral target. If one extracts the electrons via an energetic laser pulse both electrons and ions will accumulate almost immediately at the c-barrier. The symmetry of the coulomb explosion would be broken due to the fact that the electrons are only extracted along the laser propagation direction. Ergo the charge separation won't take place completely since electrons and ions fly with velocities close to the speed of light.

One has to be careful in such scenario. It represents an accelerated interaction with relativistic velocities, so that the causality is not completely evident as in the case of 'instantaneous fields'. Nevertheless qualitatively the relaxation time (see also eq. (2.88)) will be increased severely due to retardation effects, since particles and fields co-propagate at similar speeds. It could

be that there is an intrinsic 'RPA limit' for highly energetic scenarios, where one can't reach the coulomb explosion regime. This limit would be a rather academic one, since it would require very high values for a_0. Even if possibly not accessible, the maximum obtainable kinetic energy and the spectrum for such a 'mind experiment' coulomb explosion would still be given given by eqs. (2.75) and (2.77), since they are derived via a conservative potential. The temporal dynamics on how and when this final energy is achieved is a much more complicated question. An analytical treatment of this question would be highly interesting for future academic studies.

Until now only the final kinetic energy has been derived. In practice one has to prepare such a coulomb system starting from a neutral target. To obtain a non-relativistic Coulomb explosion one must extract all electrons on a timescale ΔT much shorter than the relaxation time $t_{\frac{1}{2}}$ of the system.

In the next paragraphs the classical relaxation time is derived, ergo it is assumed, that eqs. (2.78) and (2.79) are fulfilled. As seen earlier a particle initially located at $r_0 < R$ is only accelerated by particles with positions $r \leq r_0$. We can adjust C_1 in eq. (2.71) for each particle individually and obtain:

$$U(r) = \frac{1}{4\pi\epsilon_0} \frac{Q_{enc}}{r} \quad r > r_0 \tag{2.80}$$

ΔU results into the velocity of an individual particle.

$$v(r) = \sqrt{\frac{2(U(r_0) - U(r))}{m_q}} = \sqrt{C_2 \left(\frac{1}{r_0} - \frac{1}{r} \right)} \tag{2.81}$$

with the abreviation:

$$C_2 = \frac{q Q_{enc}}{2\pi\epsilon_0 m_q} \tag{2.82}$$

Equation (2.81) represents the position dependent velocity of each particle after the propagation distance $r - r_0$. The time dependent trajectory can be

obtained by separation of variables in combination with the starting condition $r(t = 0) = r_0$:

$$\int_{t=0}^{t} dt' = \int_{r_0}^{r} \frac{1}{v(r')} dr' \tag{2.83}$$

and leads to:

$$t = \sqrt{\frac{r_0}{C_2}} \left(\sqrt{r^2 - rr_0} + r_0 \operatorname{arsinh} \sqrt{\frac{r}{r_0} - 1} \right) \tag{2.84}$$

By inserting equations eqs. (2.74) and (2.82) into eq. (2.84) one obtains:

$$t = \sqrt{\frac{3\epsilon_0 m_q}{2n_{q0}q^2}} \left(\sqrt{\beta(\beta - 1)} + \operatorname{arsinh} \sqrt{\beta - 1} \right) \tag{2.85}$$

with the normalized expansion parameter $\beta = \frac{r}{r_0}$. Unfortunately the transcendent nature of eq. (2.85) hinders to obtain an analytical term in the form of $r(t)$. In the limit $r \to \infty$ eq. (2.84) reduces to:

$$\lim_{r \to \infty} t \approx r\sqrt{\frac{r_0}{C_2}} \tag{2.86}$$

Solving for r and differentiation leads to:

$$\lim_{\substack{r \to \infty \\ t \to \infty}} v \approx \sqrt{\frac{C_2}{r_0}} \tag{2.87}$$

Equation (2.87) is equivalent to eq. (2.75). Nevertheless one can deduce important characteristics inherent to the dynamics of the coulomb explosion. Equation (2.85) has no direct dependency on r_0. Since eq. (2.85) only depends on β the charge distribution evolves in a self similar fashion, ergo the rectangular shape of the charge density is preserved over time. This result is only true for the one component homogenous density profile defined in eq. (2.70). For other starting conditions the self similar evolution of the charge profile is lost (see section 2.2.4.2). Equation (2.85) allows for the definition of a

characteristic time for coulomb explosions. Equation (2.76) indicates that if the system expands by a factor of 2 it will have released half of the stored coulomb energy. With $\beta = 2$ one obtains:

$$t_{\frac{1}{2}} = \sqrt{\frac{3\epsilon_0 m_q}{2 n_{q0} q^2}} \left(\sqrt{2} + \operatorname{arsinh}(1) \right) \approx \frac{2.81}{\omega_{p_i}} \tag{2.88}$$

To a certain extend this result is quite surprising. The governing timescale is reciprocally proportional to the ion plasma frequency. The plasma frequency typically is derived for the case of a quasi-neutral infinitely large plasma with an infinitesimal disturbance [34]. Equation (2.88) was obtained starting from a spatially confined non-neutral charge distribution. The plasma-frequency seems to be a much more universal property of an assembly of various charges with charge number density n_{q0}.

Earlier it was stated, that one could generate 0.5 GeV when a polystyrene sphere absorbs 8.9 J (see section 2.2.4.2). Equation (2.88) indicates that this has to happen on a timescale $\Delta T \ll 3$ fs , resulting in extreme intensities.

Equation (2.88) is independent of the target size. This implies that laser-plasma interactions can be characterized via eqs. (2.76) and (2.88) in a zero order approximation. If the laser pulse duration is larger than $t_{\frac{1}{2}}$ the interaction can be described as isothermal. For laser pulses shorter than $t_{\frac{1}{2}}$ the interaction of the laser can be seen as isochoric. The first case the target absorbs laser energy and expands at the same time. It can be seen as a steady state between laser absorption and production of energetic particles. In the second case the target gets energized on timescale shorter than the time needed to release the stored energy via expansion. The resulting expansion is then adiabatic. In other words one can judge via $t_{\frac{1}{2}}$ if the target undergoes an intra-pulse expansion or if the laser pulse can be seen as an $\delta -$ excitation of the system.

In fig. 2.8 the blue graph shows the relaxation time $t_{\frac{1}{2}}$ given by eq. (2.88). The red graph shows the stored/absorbed energy $\mathcal{E}_{Coulomb}$ given by eq. (2.76).
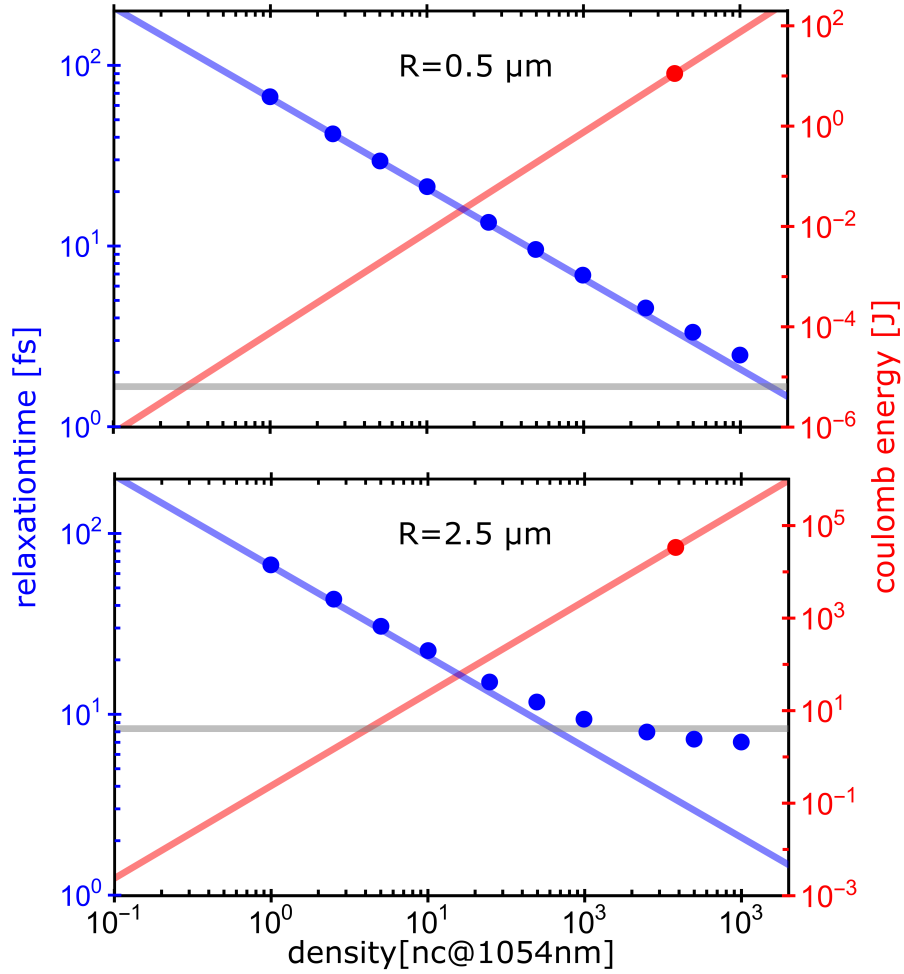
Figure 2.8: Relaxation time and stored energy of a Coulomb explosion for two different sphere sizes. The red graph depicts the stored coulomb energy given by eq. (2.76). The red dot marks the needed energy for solid density $(340 \ n_c)$. The blue line shows the relaxation time given by eq. (2.88). The blue dots resemble simulations (see section 2.2.4.2). The gray line shows the c-barrier given by $\ t_{\frac{1}{2}} = \frac{R}{c}$

The blue dots represent results obtained by simulations conducted via a particle to particle interaction code (GPT [93]). In scenarios with low maximum energies the simulations are in accordance with eq. (2.88). As soon as the ion energies reach relativistic values the blue dots do not follow the blue graph anymore (In the derivation of eq. (2.88) non relativistic speeds were a fundamental assumption). The blue dots asymptotically approach the c-barrier indicated by the gray line defined by $t_{\frac{1}{2}} = \frac{R}{c}$.

The graphs can help for the planning of future experiments. The idea is to fix the density according to the pulse duration. The target size gets chosen according to the available laser energy. Figure 2.8 does not show the maximum ion energy directly. Simulation results close to the gray line show scenarios in which ions get γ - factor of approximately 2 or even larger. Figure 2.8 also shows, that a certain minimum target size is needed to obtain high energies.

in conclusion it is interesting to highlight, that the relaxation time for near-critical plasmas $n_e \approx 5 \, n_c$ of 30 fs is similar to the pulse duration of a typical TiSa-laser system. This is a remarkable coincidence, since at these densities the target has interesting optical properties (see section 2.4.1).

2.2.4.2 Multispecies CE with Density Gradients

In section 2.2.4 the theory of an ideal one component Coulomb explosion was derived. This section will treat two aspects for more realistic coulomb explosions. The first one deals with the target geometry. In real live experiments one never interacts with a hard sharp boundary. Due to imperfections in the laser contrast(see section 2.3.1), one will always encounter a certain degree of target pre-expansion. The second aspect concerns target composition. Targets used for laser ion acceleration typically constitute a mixture of atoms rather than one single component. Plastic targets are quite commonly used for laser ion acceleration, but even targets made out of just one single species such as e.g., diamond or gold exhibit a hydro-carbon/water

contamination layer, due to imperfect vacuum conditions. These contamination layers have a typical thickness of around 1 nm [94]. The light atoms in these contamination layers are preferentially accelerated in the TNSA regime (see section 2.2.1). But often the bulk material has some contamination itself. So e.g., diamond like carbon foils have up to 10% hydrogen content in the target bulk [95].

By various methods experimentalists aim to produce one-component targets. One can e.g., heat metal targets to remove the contamination layer [24, 96]. Another approach is the production of pure hydrogen targets by cryogenic methods [97–99]. In this chapter the effects of different density profiles and target compositions will be discussed.

In Section 2.2.4 the radial density profile was given by a Heaviside step function via Equation (2.70). In this section a Gaussian and a cosine like density distribution will be compared to a solid sphere. The different density-distributions were chosen in such a manner, that the following integrals yield the same results for all three cases:

$$\frac{\epsilon_0}{2} \int E(r)^2 dV = \mathcal{E}_{Coulomb} \tag{2.89}$$

$$\int n(r) dV = N \tag{2.90}$$

Equation (2.90) ensures that the different density-profiles contain the same amount of particles. The constraint given by eq. (2.89) at the moment is quite arbitrary, but will be motivated before the end of this section.

Figure 2.9 shows exemplary the different density profiles and the corresponding electric fields.

In the case of non-homogeneous charge distributions one violates the assumptions that particles can't overtake each other. This becomes evident when one looks at the initial electric field distributions shown in fig. 2.9. The electric field is no longer monotonic in the target. One can no longer
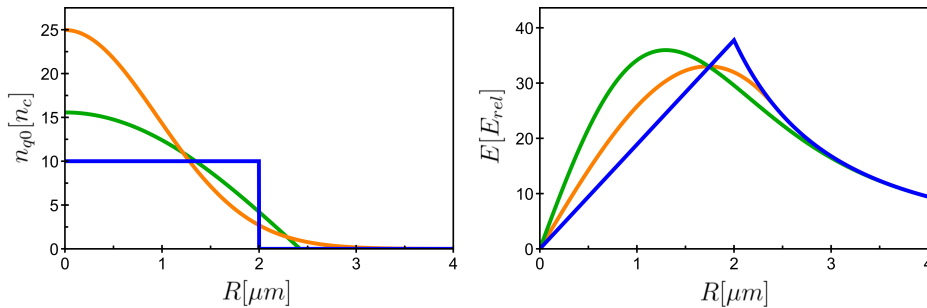
Figure 2.9: Non-homogeneous density profiles and corresponding electric field for a constant particle number N and constant coulomb energy $\mathcal{E}_{Coulomb}$. The density profile were chosen as Heaviside step function (blue), Gaussian (orange), cosine (green).

assume a self similar expansion like in section 2.2.4.1. In these cases charges will overtake each other even in the single species case. This renders an analytical treatment of the interaction complex. Here simulations were conducted to obtain some insight into the interaction. The employed code is called GPT [93]. It is a tracking code which accounts for particle to particle interactions.

The obtained spectra for the presented charge distributions (see fig. 2.9) are shown in fig. 2.10. The solid black line represents the analytical solution given by eq. (2.77). All simulations follow closely the analytically obtained spectrum for the low energy part of the spectrum. The maximum particle energy is slightly reduced for all three density profiles. All spectra exhibit a peak/bump close to the end of the spectrum due to the fact that particles overtake each other. One would expect the simulation of the homogenous charge distribution (blue line) to follow exactly the theoretical curve. Due to the granularity of the simulation this is not exactly the case. The particles are seeded via a mote carlo method. By selecting particles inside a sphere one introduces a gradient with a scale length in the order of the average intra-macroparticle-distance. If one would increase the number of macro-particles towards infinity this deviation would vanish completely (The
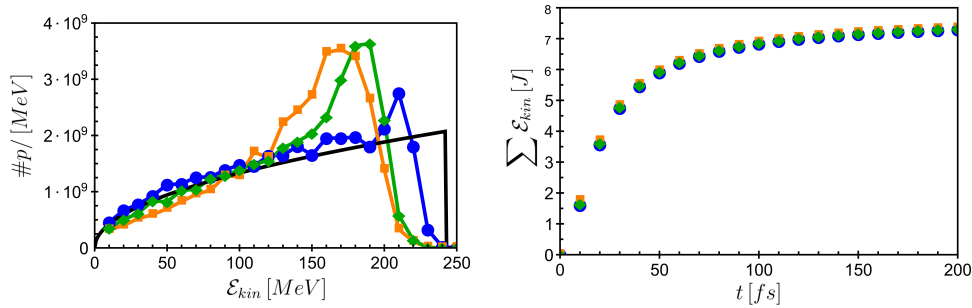
Figure 2.10: Left: Simulated spectra for a pure hydrogen target with various density profiles (see fig. 2.9) in comparison to the analytical solution under the assumption of constant particle numbers and constant $\mathcal{E}_{Coulomb}$. Right: Temporal evolution of the total kinetic energy.

number of macro particles amounted to values around 10^4). Smother density distributions don't experience this simulation error.

The time evolution of the total kinetic energy of the system is also shown in fig. 2.10. All three cases evolve in a similar fashion (The symbols of the individual simulation lie on top of each other). Ergo they are all governed by the same relaxation time $t_{\frac{1}{2}}$ even if they have different peak densities (see fig. 2.9).

Figure 2.11 shows the same situation as before only now a two component target is assumed (C:H=1:1). Now the proton spectra exhibit a pronounced mono-energetic peak located at the maximum kinetic energy as suggested by eq. (2.75). This can be explained by a rapid de-mixing of protons and carbon ions, so that a two layer target is formed, where the protons explode from the ions. For a moving target (e.g., after an RPA stage) this mechanism is refered to as directed coulomb explosion [100].

Finally one can formulate the conjecture, that for every target composition and density distribution one can construct an equivalent homogeneous sphere with eqs. (2.89) and (2.90). With this equivalent sphere one can use eq. (2.75) to estimate the maximum obtainable ion energy. Equation (2.88) can be used to estimate the relaxation time of the initially given target pa-
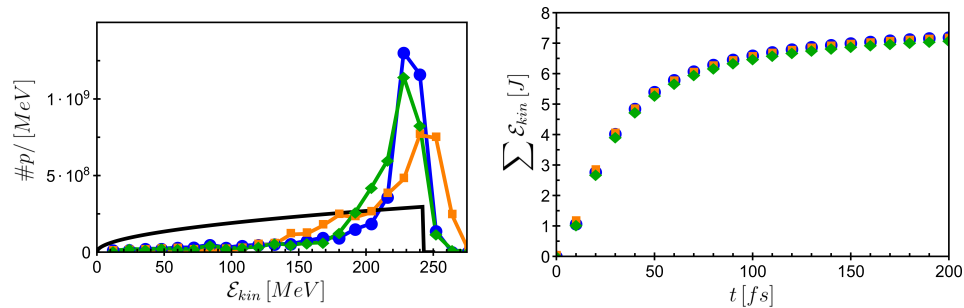
Figure 2.11: Left: Simulated spectra for a two component target (C:H=1:1) with various density profiles (see fig. 2.9) in comparison to the analytical solution under the assumption of constant particle numbers and constant $\mathcal{E}_{Coulomb}$. Right: Temporal evolution of the total kinetic energy.

rameter. This conjecture is motivated by simulations. The conjecture could be proven in a straight forward manner. Particles which experience the maximum field will be accelerated stronger than the particles in front of them. If they overtake many particles they will obtain more energy, compared the homogenous case. To obtain large ΔE one needs steep gradients. On the other hand large gradients also imply that the particles overtake each other after a very short time so that $\Delta \mathcal{E}_{kin}$ is limited. In the case of a small target these two effects work against each other. The small size and large velocities resemble the key point for the conjecture. The conjecture won't necessary hold for scenarios which involve large structures and small velocities (e.g., scenarios which could be encountered in astronomy).

The ideas presented above can be generalized for partially depleted targets. In cases where the relaxation time of the fully charged sphere is shorter than the laser pulse duration, the potency of the equivalent homogeneous sphere diminishes over time, due to the intra-pulse expansion. If one pursues this idea further with more sophisticated models one could derive a TNSA limit, which is set by the pulse duration of the driving laser. This would explain, why new PW-TiSa systems achieve proton energies [101] comparable with results obtained on PW glass laser systems [18,69].

Similarly the maximum obtainable kinetic proton energy gets diminished in the case of a pre-expansion. As seen in fig. 2.9 a pre-expansion would lead to a less potent equivalent sphere compared to the unexpanded sphere, with the trivial limit of zero kinetic energy for a completely vanished target.

2.2.4.3 From CE to RPA

In the previous chapter the dynamics of an ideal and semi-ideal CE were discussed. The initial charge distributions are rather defined in an axiomatic way. In a real world experiment such a charge distribution would have to be prepared starting from an initially neutral target, e.g., by expelling the electrons with a strong laser pulse. To prepare situations comparable to an ideal CE the electron population must be expelled from the target on timescales Δt shorter than the relaxation time $t_{\frac{1}{2}}$ given by Equation (2.88):

$$\Delta t \ll t_{\frac{1}{2}} \approx \frac{2.81}{\omega_p} \tag{2.91}$$

Ergo an energy $\mathcal{E}_{Abs}$ has to be deposited to an area of πR^2 during a time $\Delta t \ll t_{\frac{1}{2}}$ to be able to prepare a system which will subsequently will undergo a CE.

In section 2.2.3 it was shown, that during RPA the light pressure is balanced by the restoring forces of the plasma. This force balance is expressed in eqs. (2.67) and (2.68). By converting the equality into in inequality one also can define a CE condition since then the light forces would exceed the maximum achievable restoring forces from the plasma.

In this spirit one should also be able to obtain a RPA condition starting of the equations derived for the CE in section 2.2.4. Using eqs. (2.76) and (2.88) one can define an intensity via:

$$I = \frac{C_{Abs}\mathcal{E}_{Coulomb}}{t_{\frac{1}{2}}\pi R^2} = \frac{1}{2}c\epsilon_0 a_0^2 E_{rel}^2 \tag{2.92}$$

C_{Abs} depicts the absorption coefficient which can take values between 0 and

1. Inserting eqs. (2.39), (2.76), (2.88) and (2.101) into eq. (2.92) leads to:

$$a_0 = \pi \frac{n_e}{n_c} \frac{R}{\lambda} \sqrt{\frac{32 C_{Abs} R}{15 t_{\frac{1}{2}} c}} \tag{2.93}$$

Equation (2.93) has great similarity to the radiation pressure balance given by eq. (2.67), if one ignores the term under the square-root. Fortunately the term under the square root takes values close to 1. It is interesting to note that eq. (2.93) was obtained without any assumption of a force balance, nevertheless the dynamics (and hereby forces) are encoded in the relaxation time $t_{\frac{1}{2}}$ of the system. Secondly no explicit microscopical picture is use to derive eq. (2.92). The laser energy can be brought into the target by absorption (TNSA-like) or via momentum transfer (RPA-like). Obviously the magnitude of C_{Abs} strongly depends on the underlying microscopical processes.

2.3 Laser Contrast and Pre-Plasma Dynamics of MLTs

Today's high power laser systems are able to reach peak intensities of up to $2 \cdot 10^{22} \frac{W}{cm^2}$ [102]. During the temporal evolution of the such a pulse the intensity sweeps over twenty two orders of magnitude. A lot of different physical effects take place on the way to the peak intensity. For example the formation of a plasma occurs at intensities in the order of $10^{13} \frac{W}{cm^2}$ (see section 2.3.2). In the case of a perfect Gaussian envelope in time, this intensity is reached at $\approx 3.5 \cdot FWHM$ prior to the peak of the main pulse (assuming an peak intensity of $2 \cdot 10^{22} \frac{W}{cm^2}$). Unfortunately real world laser-pulses deviate significantly from an ideal Gaussian temporal profile. Typically the formation of a plasma occurs a few ten to hundred picoseconds prior to the arrival of the main pulse corresponding to approximately $350 \cdot FWHM$. This is hundred times worse than the ideal case. It should be noted that this is already a great

technological achievement and always has to be considered in the context of other laser parameters such as: peak intensity, focus quality, pulse energy etc. Nevertheless as soon as the target is converted into a plasma, the target will undergo pre-expansion, ergo the initial density profile gets modified prior to the arrival of the main pulse. This target modification via pre-plasma dynamics is inherent to all high intensity laser-plasma experiments, which use solid density targets. The underlying different physical processes are well known in principle. Their multitude in combination with the rapidly changing intensity render it rather difficult to predict the amount of target pre-expansion due to the imperfect laser contrast. Nevertheless it is essential to know which target parameters are encountered by the arrival of the main pulse. The amount of pre-plasma expansion can alter the main interaction significantly. Typically experimentalist try to minimize the amount of pre-plasma expansion by employing many different techniques to enhance the temporal laser contrast.

The following subsections will motivate various aspects related to pre-plasma physics. In section 2.3.1 the temporal evolution of a real world laser pulse is described using the example of the PHELIX laser pulse. Section 2.3.2 describes the plasma formation via the process of field ionization. Section 2.3.3 describes the most important absorption process for intensities $< 10^{17} \frac{W}{cm^2}$. The treatment of pre-plasma dynamics using analytical approaches or simulations is very demanding. Section 2.3.4 motivates the complexity via a heuristic description of the pre-plasma-expansion of a sub focus sized mass limited target as encountered in experiment (see section 3.2.1).

2.3.1   Laser Contrast

The temporal shape of laser intensity is referred to as temporal contrast. The temporal contrast resembles a key parameter of a high power laser systems. Figure 2.12 shows the temporal contrast for the PHELIX laser system, as used in the experiment. The laser pulse has a duration of 500 fs (FWHM of
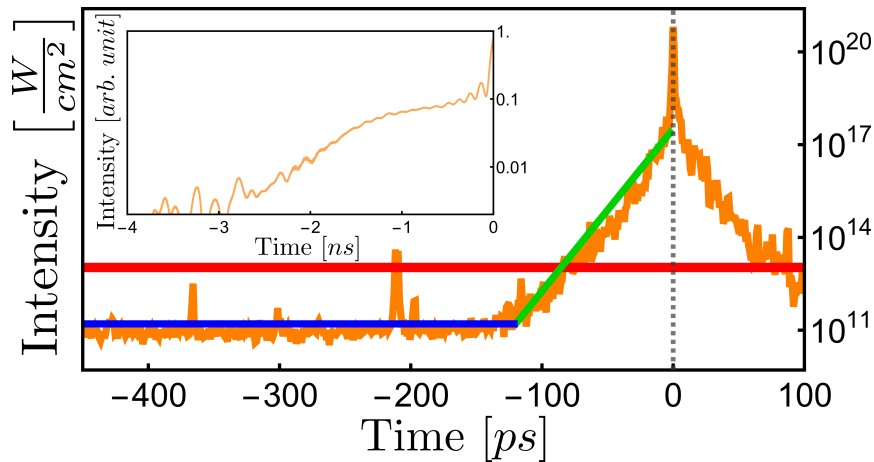
Figure 2.12: Logarithmic plot of the temporal contrast of the PHELIX laser pulse. The trace was obtained by auto correlation (Data kindly provided by Florian Wagner).

the intensity). The pulse energy amounts to 150 J. One notices directly, that the laser pulse deviates significantly from an ideal Gaussian distribution.

The pulse is situated on a so called ASE-pedestal with a few ns length. Amplified spontaneous emission (ASE) mainly originates from cavities present at the front end of a high power laser system. Spontaneous emitted photons from gain medium in the resonator build up a cw component in the cavity, which competes with the recirculating laser pulse. When the pulse is extracted, this cw component is extracted as well and amplified in the subsequent amplifier chain, forming the so called ASE-pedestal. By the use of a fast Pockels cell the length of the ASE is reduced to a few ns. This is close to the absolute minimum, since the Pockels cell operates on a stretched laser pulse and it should be avoided to cut into the spectrum of the main pulse. In practice the ASE level must be kept to intensity levels, where no plasma is formed, meaning below $10^{13} \frac{W}{cm^2}$. Otherwise the target would be gone completely prior to the arrival of the main laser pulse. With increasing peak intensities the ratio of ASE to peak intensity needs to be optimized. This ratio is typically referred to as ASE laser-contrast. Various techniques have

been used to influence the ASE-contrast. Most methods rely on nonlinear effects. In the case of the PHELIX laser the ASE level (blue line in fig. 2.12) amounted to values better than $10^{11} \frac{W}{cm}$. At these intensity values the target can be assumed to be unaffected by the ASE (see section 2.3.2).

Around -200 ps there is a small pre-pulse. Pre-pulses can be caused by many different reasons. Typically they do not carry a lot of energy into the plasma since they have a similar duration like the main pulse, and have many orders of magnitude weaker peak powers. The intensity of a pre-pulse can strike a plasma (the red line in fig. 2.12 indicates the damage threshold, also see section 2.3.2). With the formation of a plasma, collisional absorption can efficiently couple ASE laser energy into the plasma (see section 2.3.3). Collisional absorption is most efficient for dense and cold plasmas. Even if the energy provided by the ASE is quite small, one has to recall, that it acts over a relatively long time compared to the duration of the main pulse. Slow pre-plasma dynamics can have large effects if they have enough time to act on the plasma.

An exponential shoulder (also called coherent contrast) preceding the main pulse is common to most laser systems (green line in fig. 2.12) The origin of the coherent contrast is until now not completely identified. There are hints, that it is produced in the strecher of the laser systems. In contrast to ASE and prepulses the coherent contrast carries a large amount of energy, which can be coupled into the dense cold plasma via inverse Bremsstrahlung (see section 2.3.3). The coherent contrast emerges from the ASE level at around 110 ps prior to the main laser pulse. It contains roughly 1% of the total laser energy ≈ 1.5 J, if one integrates from $t_1 = -\infty$ to t_2 , with $I(t_2) = 10^{18} \frac{W}{cm^2}$.

2.3.2   Damage Threshold and Field Ionization

At large enough intensities matter turns into a plasma. The properties of a plasma are quite similar to metals. So a trasnparent dielectric target will

change its optical properties as soon as it turns into a plasma. Initially the target is transparent and almost doesn't absorb light. An over-critical plasma on the other hand is reflective and efficiently absorbs laser energy (see section 2.3).

Shortly after the light induced damage occurred plasma dynamics start due to energy transport into the plasma. Ergo for laser-plasma interactions, it is vitally important to know at which intensities a plasma is formed. Unfortunately this question is rather difficult to answer in detail, since it depends on many different parameters such as target material, pulse duration etc. Depending on the circumstances different effects might be responsible for plasma creation such as: multi-photon ionization, avalanche ionization or field ionization.

For short pulses ($\ll 12^{-12}\ s$) field ionization is the dominant effect. A rough estimate for necessary intensities can be derived via the so called above the barrier ionization. Hereby the electric field of the laser distorts the binding potential of the atom in such a strong way, that no bound solution for the valance electron exists anymore. This results into the ionization of the atom. The field ionization threshold is given by [103]:

$$I_{FI} = \frac{Z_{eff}^6}{256} I_{at} \tag{2.94}$$

Where the atomic intensity is given by $I_{at} = 3.5 \cdot 10^{16} \frac{W}{cm^2}$ and the effective atomic number is given by $Z_{eff} = \sqrt{\frac{\mathcal{E}_i}{13.6\ eV}}$. Z_{eff} incorporates all physics which take place in the shell structure of the atom via the ionization energy E_i.

For a typical first ionization energy of 6 eV leads to intensities of $10^{13} \frac{W}{cm^2}$. Due to the possibility of tunneling, field ionization can take place at slightly lower intensities than estimated by eq. (2.94). Nevertheless eq. (2.94) delivers a good order of magnitude estimate. So e.g., to fully ionize carbon one need an intensity of $6 \cdot 10^{18} \frac{W}{cm^2}$.

2.3.3   Collisional Absorbtion (Inverse Bremsstrahlung)

Due to their high conductivity plasmas can be effectively heated by electro-
magnetic waves. Collisional absorption describes the energy transfer of an
electromagnetic waves into a plasma by binary electron-ion collisions. It is
the dominant heating process in plasmas for intensities below $10^{17}\frac{W}{cm^2}$ [73].
It is also known under the term inverse Bremsstrahlung. This terminology
is somewhat miss leading. Bremsstralung describes the conversion of en-
ergetic electrons into electromagnetic radiation, while collisional absorption
describes the conversion of electromagnetic waves into energetic electrons.
This symmetry lead to the name inverse Bremsstrahlung. It is important
to point out, that the microscopic nature of both processes are completely
different. Inverse Bremsstrahlung does not represent a time reversed version
of Bremsstrahlung.

The physical picture of collisional absorption is quite simple. Light im-
pinging on a plasma will be reflected at the critical density. In the resulting
standing wave electrons undergo a quiver motion. This quiver motion is ran-
domized by binary electron-ion collisions. This leads to the damping of the
electromagnetic wave and increases the temperature of the plasma.

Collisional absorption has been extensively investigated in the past [104–
106]. To derive quantitative results the picture gets quite complex. So for
example one has to account for the field swelling in a plasma gradient due
to the local dependency of the group velocity, which depends on the den-
sity gradient. The electron ion collision frequency is a function of plasma
temperature and density, the dynamics of the plasma depend on its density
and temperature and so on. Completely self-consistent solutions are almost
impossible to obtain.

The fractional absorption rate f_A can be derived for assumed density
profiles. For an exponential density gradient of the form $n_e = n_c e^{-\frac{x}{L}}$ the

fractional absorption is given by [107]:

$$f_A = 1 - e^{-\frac{8\nu_{ei}^{\star}L}{3c}\cos^3\alpha} \tag{2.95}$$

In the case of a linearly density profile f_A is given by:

$$f_A = 1 - e^{-\frac{32\nu_{ei}^{\star}L}{15c}\cos^5\alpha} \tag{2.96}$$

α represents the angel of incidence, $\nu_{ei}^{\star} = \nu_{ei}(n_c)$ is the collision frequency at the critical density given by:

$$\nu_{ei} \approx 3 \cdot 10^6 \ln{(\Lambda)} \frac{n_e Z}{\theta_{ev}^{\frac{3}{2}}} \tag{2.97}$$

Here the density n_e is given in cm^{-3} and the plasma temperature is given in eV. Z depicts the atomic number. Λ is the so called coulomb logarithm which is given be the fraction of maximum and minimum impact parameter b . In the case of collisional absorption Λ is given by:

$$\Lambda = \frac{b_{max}}{b_{min}} = \frac{\frac{v_e}{\omega}}{\frac{Zq^2}{mv_e^2}} \tag{2.98}$$

Equations (2.95) and (2.96) already imply, that most of the absorption takes place at the critical density, otherwise one would expect a more complex density dependency. This becomes evident if one looks at the energy damping rate κ [105]:

$$\kappa = \frac{\nu_{ei}\omega_p^2}{c\omega\sqrt{1 - \frac{\omega_p^2}{\omega^2}}} = C_1 \frac{Zn_e^2}{\theta_{ev}^{\frac{3}{2}}\sqrt{1 - \frac{n_e}{n_c}}} \tag{2.99}$$

Equation (2.99) shows that collisional absorption works best for cold, high Z plasmas near the critical density. Figure 2.13 shows the corresponding graph for an carbon plasma with a plasma temperature of 600 eV. Figure 2.13 illustrates that in the absence of a critical density region no significant heating
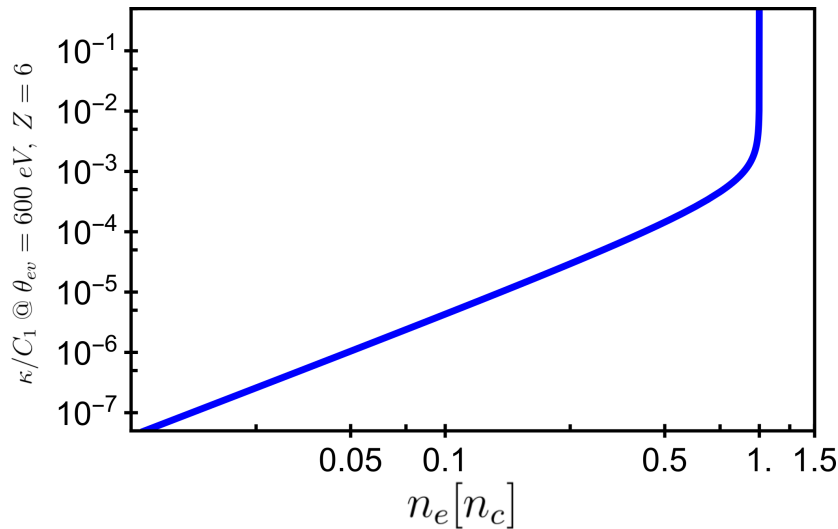
Figure 2.13: Energy damping rate κ due to collisional absorption for a Carbon plasma with a plasma temperature of $600\ eV$

of the plasma will occur.

2.3.4 Pre-Plasma-Dynamics of a Sub-Focus Sized MLT

As stated in section 2.3.3 pre-plasma dynamics prior to the main laser pulse constitute a complicated physical situation. Therefore the following aspects are treated in a rather qualitative manner.

The pre-plasma dynamics of sub focus sized spheres differs from standard foil targets. In contrast to a foil, a sphere has two additional degrees of freedom to expand, ergo the density drops much faster compared to foil targets under the assumption of comparable expansion velocities. A second difference constitutes the fact, that during the expansion the cross-section of the sphere enlarges due to its initial sub focused size dimensions, ergo the amount of energy absorbed per particle increases as long as the target is still over-critical. Ergo one expects higher temperatures compared to a foil. This further increases the reduction of target density.

As soon as the target turns completely under-critical there is no further relevant absorption (see section 2.3.3) and the energy import into the target stops. This implies that from this moment on cooling effects such as radiative cooling and cooling due to expansion reduce the target temperature and hereby also the expansion velocity.

The experimental verified peak density for a sub-focus sized mass-limited target at the PHELIX laser shows values close to the critical density. The fact that a 1 μm diameter sphere expands to those values can have two different explanations.

It could be, that the laser had just the right amount/quality of contrast, that one obtains these density values by pure luck. A different contrast would have lead to other densities.

An alternative explanation would be a self regulating mechanism. As explained above a sphere reaches low densities sooner than foils. This could have the effect, that a low contrast leads to a premature expansion. The target expands sooner and reaches under-critical densities at low expansion speed (since this happens early in the rising edge). As soon as the target turns under-critical the remaining part of the coherent contrast can pass through the target without depositing further energy for $I < 10^{17} \frac{W}{cm^2}$. In this scenario a lower contrast can lead to a smaller target pre-expansion.

Clarification, if the target pre-expansion can be described by this anti-intuitive behavior or if it was encountered by lucky circumstances, remains to be investigated in future experiments.

2.4   Reflected and Transmitted Light of a Laser-Plasma Interaction with MLTs

2.4.1   In-Line-Holography

As stated before pre-plasma expansion is an important aspect in laser ion acceleration (see section 2.3) and also hard to simulate (see section 2.3.4). To quantify pre-plasma expansion experimentally various optical methods have been established such as shadowgraphy and interferometry. The refractive index of the plasma is given by:

$$\eta = \sqrt{1 - \frac{n_e}{n_c}} \tag{2.100}$$

n_c is the critical density given by:

$$n_c = \frac{\epsilon_0 m_e \omega_L^2}{e^2} = \frac{4\pi^2 \epsilon_0 m_e c^2}{e^2 \lambda_L^2} \tag{2.101}$$

n_e is the electron number density, e, m_e represent the electron elementary charge and electron mass. Equation (2.100) shows, that for electron densities larger than the critical density, the refractive index is imaginary, thus only evanescent waves can propagate into the plasma. For electron densities smaller than the critical density the plasma exhibits a refractive index with a value between zero and one. Light is able to propagate through the plasma with superluminestent phase velocities.

The critical density scales with λ^{-2}. Two different laser systems are widely used in high intensity laser-plasma interactions experiments. Glass lasers using Nd:YAG-glass as amplifying medium, with a central wavelength of 1054 nm and TiSa crystals with a central wavelength of 800 nm. The
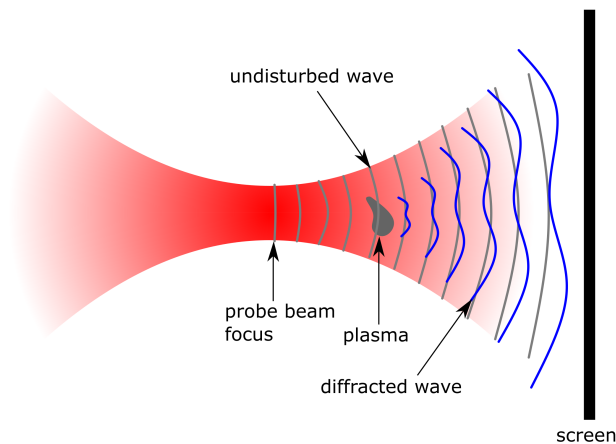
Figure 2.14: Schematic setup for In-Line-Holography.

corresponding critical densities are:

$$n_{c,800nm} \approx \frac{1.74 \cdot 10^{27}}{m^3} \tag{2.102}$$

$$n_{c,1054nm} \approx \frac{1.00 \cdot 10^{27}}{m^3} \tag{2.103}$$

Shadowgraphy and interferometry are mostly based on complex experimental setups. They rely on secondary beams (often frequency doubled or shifted in frequency to circumvent problems with the self-emission of the plasma under investigation). These secondary beams need to be overlapped with the target and driver beam in space and time.

In-Line-Holography (ILH) [108] represents a probing method ideally suited for sub focus sized mass limited targets (MLT). A schematic sketch of this method is shown in figure 2.14. For ILH the object under investigation is placed in a coherent diverging beam. Parts of the light wave which 'hit' the object are modified in amplitude and/or phase and interfere with parts of the beam which passed the object undisturbed. The resulting hologram encodes

information about the object.

Due to its collinear nature and the necessity that light has to pass by the target undisturbed, implies the use of MLT's. The elegance of this method relies in its simplicity. In the case of a MLT the driving laser can act as probe at the same time. One just has to record the transmitted light via a screen and a camera. A 'drawback' of this single beam setup (in the presented experiment actually a feature) constitutes the fact, that the hologram is recorded at peak intensity. Since probe beam and driver consist of the same beam, they are perfectly overlapped in space and time. The plasma states before and after the main interaction can not be investigated by this single beam method without losing the simplistic setup consisting out of solemnly one beam, screen and camera. The experimentally recorded holograms/diffraction patterns are shown in figure 3.5

2.4.2   Reflected Light (Relativistic Mirror)

If light gets reflected from a relativistic moving object (e.g., by a mirror) the light is also shifted in its frequency. This is a famous thought experiment described by Einstein [109].

An observer which moves away from a light source will see a red-shifted version of the light source. In the laboratory frame light will have traveled the distance $c\Delta T = \lambda$ during one period $\Delta T = \frac{1}{f}$. If the observer co-propagates with the light source it will take a longer time ΔT_2 between two extrema of the electric field. This leads to:

$$c\Delta T_2 = \lambda + v\Delta T_2 \tag{2.104}$$

The observer will experience a shifted frequency given by:

$$f' = \frac{1}{T_2'} = \frac{\gamma}{T_2} = \frac{c}{\lambda'} \tag{2.105}$$

By eliminating T_2 from eqs. (2.104) and (2.105) on obtains the equation for

the relativistic Doppler effect:

$$\lambda' = \sqrt{\frac{1+\beta}{1-\beta}}\lambda = (1+\beta)\,\gamma\lambda \qquad (2.106)$$

Here the convention is used, that a positive β indicates that light and observer move into the same direction. In the case of a source which moves towards an resting observer, one obtains the same formula only with altered signs.

In the case of a moving mirror, the relativistic Doppler shift has to be applied twice, since one changes from the laboratory frame into the mirror frame and back again into the laboratory frame. Due to the reflection the symmetry is broken and the two frame changes do not cancel each other out. The mirror sees a red shifted source. It reflects this red shifted light which the observer in the laboratory frame records with an additional redshift, since the source (mirror) is moving away from him. The frequency shift for a relativistic moving mirror with $\beta \approx 1$ is then given by:

$$\lambda' = \frac{1+\beta}{1-\beta}\lambda = (1+\beta)^2\,\gamma^2\lambda \approx 4\gamma^2\lambda \qquad (2.107)$$

With the availability of relativistic intensities the thought experiments from Einstein can nowadays by realized at today's high intensity laboratories. The concept of the relativistic mirror can be used to generate energetic radiation via high harmonic generation [110, 111] or by Thomson back scattering [112].

But the concept of the relativistic mirror is also a nice diagnostic tool for laser-plasma interactions [113, 114]. During a laser-plasma interaction light is reflected from the target at the critical density. The position of the critical density can change during the laser pulse. The velocity of this movement is encoded into the reflected spectrum [115]. A blue shifted spectrum would indicate a plasma expansion towards the laser, while a redshift indicates a movement in laser propagation direction. For example the hole boring velocity was experimentally verified by the analysis of reflected light [113].

Unfortunately one can not derive the complete dynamics just by the spec-

trum alone, since it constitutes a time integrated observable. This becomes evident by a simple thought experiment. If one assumes a mirror which is linearly accelerated from v_1 to v_2 and a second mirror which is decelerated from v_2 to v_1 it is evident that the spectrum in both cases will be the same. Nevertheless the reflected spectrum in combination with additional experimental and simulation data can help to solidify the physical interpretation of experiments.

Chapter 3

Experiment

3.1 General Remarks Concerning Experiments with High Power Laser Systems

To investigate uncharted physical terrain, experimentalists make use of advanced technological methods. Often state of the art technology is used to study nature in unequaled detail. Examples for such techniques are: modern telescopes [116], electron microscopes [9], laser spectroscopy [117], etc.

In the case of high intensity laser matter interactions, highly advanced technology is used to create and modify extremest conditions of matter. Unfortunately, due to the small volumes and short times of such interactions, available diagnostic techniques are often limited in one way or the other. Most experimental observable quantities are obtained as time integrated values, which are recorded at macroscopic distances away from the interaction point. Due to the complexity and nonlinear nature of laser-plasma interactions, interpretation and evaluation of experimental data is rather complicated and sometimes even impossible.

Modern numerical methods such as e.g., particle in cell codes (PIC) [118] are able to describe virtual experiments of laser-plasma interactions. Due to

their virtual nature they can access different parameters much easier. For example changing the target density in a simulation is a rather easy task, while in experiments this often implies the use of a completely different target system. Furthermore diagnostics with virtual detectors are almost unlimited compared to experimental diagnostics. So the question remains, why one still conducts real world experiments if simulations are so much better and easier?

Even if the last statement is rather provocative the answer is quite simple: These kind of simulations are very complex and need large computational resources. The development of the appropriate codes which run efficiently on today's supercomputers is a challenging task itself. The challenges that need to be solved are so diverse and complex, that a new field in physics did emerge - computational physics.

A second drawback of pure virtual experiments is given by the fact, that simulations only resemble the world as good as the physics they contain. The outcome of a real experiment is defined by the laws of nature. The outcome of a simulated experiment is purely defined by the employed algorithms (including approximations and possible mistakes). Accordingly the codes must be bench marked against real world experiments.

This benchmarking is a rather complex task for itself. Due to the technological constraints (computation time, computational power, hard disk and memory capabilities) numerical physicist need to make several simplifying assumptions concerning the simulation of laser-plasma interactions. Typical assumptions are e.g., reduced dimensionality, the postulation of a continuum rather than a granular system, the absence of ionization dynamics etc.

Next to these simulation inherent approximations, also experimental uncertainties make it difficult to compare simulation and experimental data. The experimental insecurities can be target pre-expansion, peak intensity, spatio-temporal distribution of the laser energy in the focal spot etc. For example the pre-expansion of the target prior to the main laser pulse is

often not know by experimentalist due to imperfect laser contrast (see section 2.3.1) and a lack of proper diagnostics [119, 120]. In many simulation centered publications the pre-expansion is only an arbitrarily guessed value (typical in the order of λ). Some publications try account for pre-expansion by additional simulations applying hydrodynamic codes in the presence of collisions [121]. Nevertheless, the underlying physics of those codes is quite complex since they treat highly coupled plasmas.

In this work we could quantify the pre-plasma expansion experimentally. This was accomplished by the implementation of an in-line-holography in combination with a mass limited target.

This information allowed to benchmark the PIC-code PIConGPU [122], by comparing the time integrated experimental results and the corresponding quantities encountered in the simulation. It was found, that for the presented target system a reduction in dimensionality leads to wrong simulation results. Unfortunately, reducing the dimensionality is one of the most effective ways to save computational resources. Fortunately, the small target density and limited particle number were perfect requisites, which enabled to conduct a three-dimensional PIC simulations. A team of numerical scientist from the Helmholtzentrum Dresden-Rossendorf conducted the PIC simulation at the Oak Ridge Leadership Computing Facility. The simulation was conducted on the supercomputer named TITAN and took approximately $10^7/; cpuh$. Due to its large computational cost the simulation could only be run once. A three-dimensional simulation yielded satisfying agreement between theory and experiment (see section 3.2.3).

The quantitative reproduction of the experimental results creates great confidence that the developed PIConGPU code indeed simulates reality to a high degree of accuracy, if applied with accurate input parameters, proper dimensionality etc. This benchmarke dsimulation then allows to study the interaction in a more detailed way than by purely experimental methods as discussed above. Hereby the PIC simulation helps to study the microscopic

and time resolve picture of the acceleration process. This deeper understanding helps to identify possible ways for future optimizations of this accelerating mechanism in future experiments (see chapter 4).

3.2   Paul Trap GSI

The subsequent sections will describe the experimental results obtained during an experimental run at the PHELIX laser-system located at GSI near Darmstadt. A schematic sketch of the experimental setup is given by fig. 3.1. The photograph of the experimental setup at GSI is shown in fig. 3.2. The following paragraphs describe the main components of the experiment shown in fig. 3.1.

PHELIX-laser

The PHELIX-laser is a CPA based laser system based on glass amplifiers. Glass amplifiers have the advantage that they are available in large sizes. This allows the generation of energetic laser pulses. Due to the poor thermal conductivity of glass the PHELIX-laser system is limited to one shoot every 90 minutes. PHELIX runs at a central wavelength of 1054 nm with 3 nm bandwidth. Due to the bandwidth the pulse duration amounted to 500 fs. The pulse energy was 150 J. The laser beam had an diameter of 250 mm and was focused by an 45° off-axis parabolic copper mirror with an effective focal length of 400 mm. The resulting focal spot diameter measured 3.7 ± 0.3 μm. A typical focus image is shown in fig. 3.3. The peak intensity amounted to $2 \cdot 10^{21} \frac{W}{cm^2}$. The laser contrast is enhanced by a fast Pockels cell and the use of optical parametric pulse cleaning techniques. The laser contrast of Phelix is described in detail in section 2.3.1. The PHELIX laser exhibits a pointing jitter of roughly one focal spot diameter, a typical value for high intensity lasers. To increase the hit probability the target was positioned roughly one Rayleigh length behind the focal
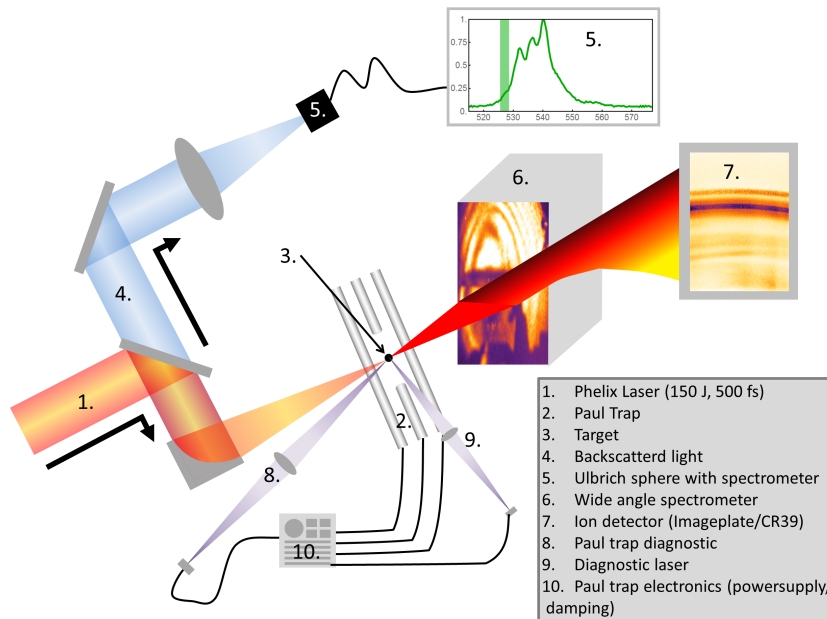
Figure 3.1: Schematic overview of the experimental setup. 1. incoming PHELIX laser beam with beam diameter of $250\ mm$ 2. linear Paul trap 3. target, PMMA (hollow) sphere with $d = 1\ \mu m$ 4. reflected light beam path 5. Ulbrich sphere with attached optical spectrometer 6. wide angle spectrometer with optical diffraction pattern on the front plate 7. Image Plate raw proton/ion data (without degraders) 8. optical path for the electro-optical diagnostic for target damping and positioning 9. $660\ nm$ illumination laser 10. Paul trap electronics
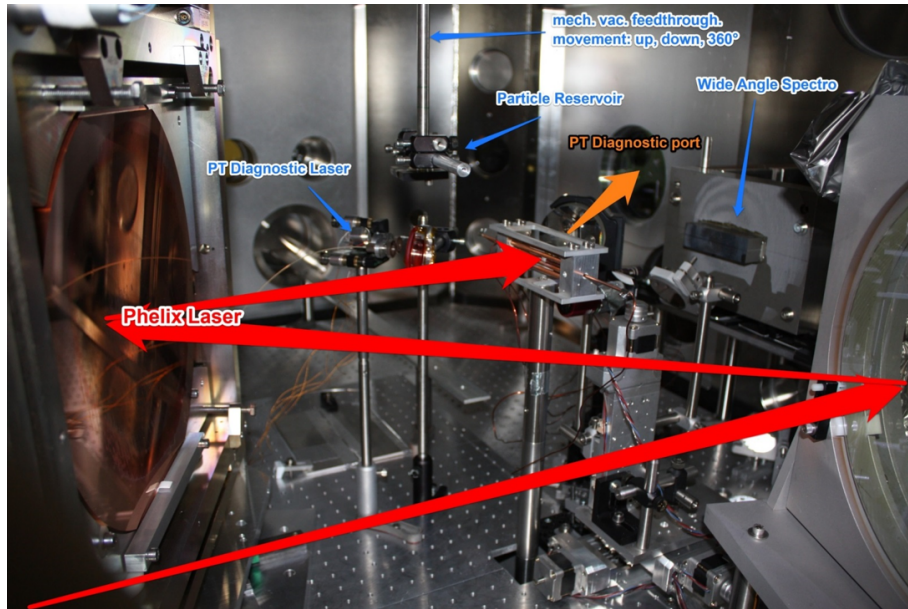
Figure 3.2: Photograph from the inside of the PHELIX experimental chamber taken after the first shoot.
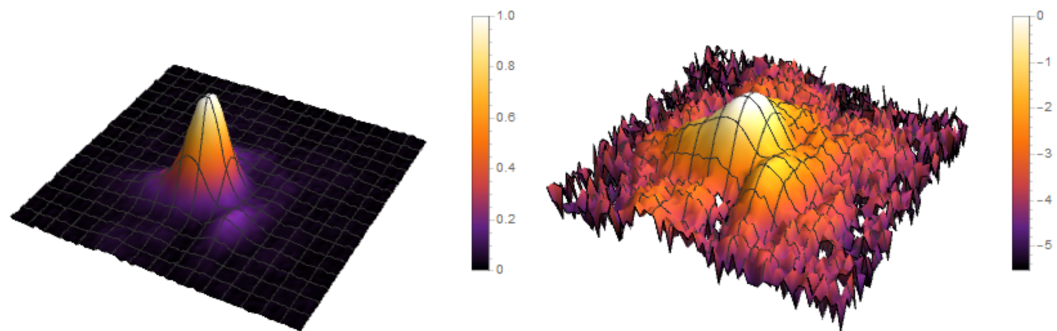
Figure 3.3: Focal spot of the PHELIX laser system. Left linear scale, right logarithmic scale.

spot.

Paul-trap

Plastic spheres with a diameter of 1 μm and hollow spheres with the
same outer diameter and wall strength of 100 nm were used as targets.
The amount of contained protons only differs by a factor of 2 for hollow
and solid spheres. Due to their small spatial dimension they were
charged and subsequently trapped by an electrodynamic Paul trap.
The functionality of the trap is described in [52–57].

Backscattered light diagnostic

Behind the last turning mirror we collected the leakage of the back-
scattered light with an 90° off-axis parabolic mirror. The backscattered
light was collected with an Ulbrich sphere and spectraly recorded via
an attached fiber spectrometer.

Particle Spectrometer

A wide angle spectrometer was employed to measure proton and elec-
tron beams. The technical details and information about deconvolution
of the raw data are given in chapter A. CR39 and Image plates were
used as detectors. The front plate of the spectrometer served as screen
for the in-line-holography.

3.2.1   In Situ Target Characterization via In Line Holography

As described in section 2.4.1 in-line-holography (ILH) [108] constitutes a
method to determine the pre-expansion of the target prior to the main laser
pulse. ILH has already been used experimentally to characterize small air
plasmas [123]. In this experiment ILH was used to determine the amount of
pre-plasma expansion (a critical input parameter for PIC simulations). The
PHELIX laser pulse acts as driver and probe at the same time. The sub
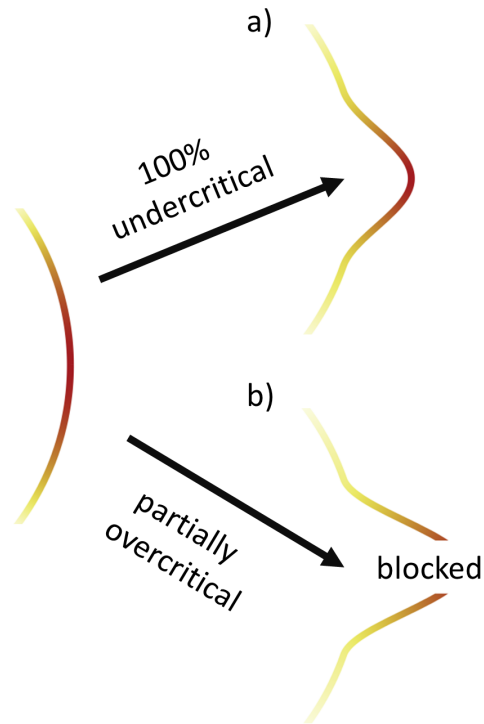
Figure 3.4: Schematic presentation of the alternation of the phase front due to the pre-expanded target. The color scale indicates the amplitude of the wave. a) depicts a pre-expansion where the maximum density of the target is smaller than the critical density. The target acts as a pure phase object. b) shows the case for a target which is partially over-critical. Here the middle part of the beam gets blocked.

focus sized mass limited target was placed $1 - 1.5$ Rayleigh-lengths behind the focal spot constituting an extreme situation for ILH. Depending on the amount of pre-expansion the incoming laser pulse is modified in amplitude and phase. This is schematically shown in fig. 3.4. In regions were the plasma is over-critical the light is blocked. Under-critcal regions alter phase of the beam. This modifications of the expanding beam alter the near field of the PHELIX laser which was recorded on the spectrometer front plate.

In the next paragraphs the methodology for the simulated diffraction

patterns will be described. In a first step one must model the PHELIX laser. To mimic divergence and laser focal spot size, a Gaussian beam was assumed with a $M^2 = 2.8$. Twenty micrometer behind the focus a spherical electron distribution has been defined by:

$$n_e(r) = n_m e^{-\frac{r^2}{2r_\sigma^2}} \tag{3.1}$$

The number of initially contained electrons is fixed. To keep the number of particles constant for all different σ it follows:

$$n_m = n_0 \sqrt{\frac{9\pi}{8}} \frac{r_0^3}{r_\sigma^3} \tag{3.2}$$

The electron density was assumed to be a thin lens. The optical path difference in dependency of the radius was evaluated numerically to alter the phase of the incoming beam accordingly. For regions with over-critical density the amplitude of the wave was set to zero. Evanescent waves and diffraction inside the target were neglected completely.

The obtained phase and amplitude maps were used to solve Kirchhoff's integrals to obtain the diffraction patterns in the near field.

The experimentally obtained diffraction patterns are shown in fig. 3.5. This experimental data can be compared to simulated data for various values of target pre-expansion. Amount of fringes and fringe contrast allow to make a rough guess regarding the encountered pre-expansion.

From these considerations it can be inferred that the peak density of the target dropped by a factor of ≈ 420 from $340n_c$ to $0.8n_c$. This large value might seem surprising. Recalling the concepts presented in section 2.3.4 indicating a stronger pre-expansion for MLT's compared to foil targets and the fact that the 110 ps long exponential shoulder present in the time evolution of the laser (see fig. 2.12) contains an total energy of 1.5 J motivates this extensive pre-expansion.

If the final density distribution results out of a self regulatory mechanism
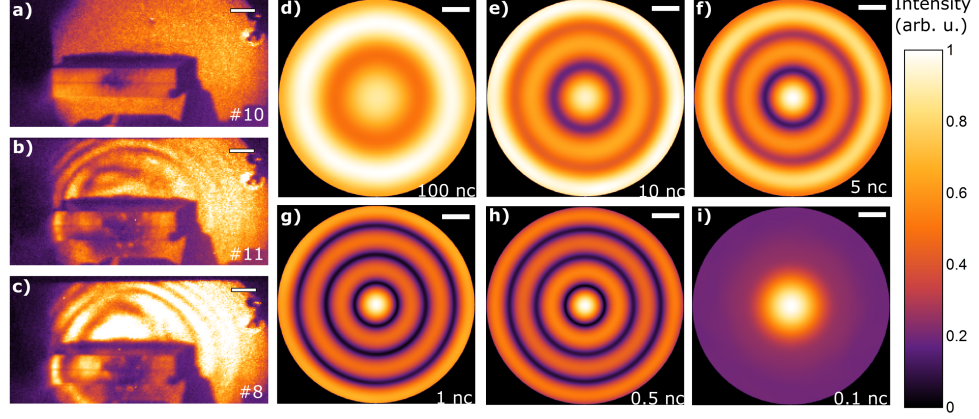
Figure 3.5: Experimental obtained diffraction patterns via in-line-holography. a) blank shot b) solid sphere c) hollow sphere d-i) simulated diffraction pattern for Gaussian density profiles with differing peak densities.

or if it was encountered by a lucky coincidence of laser and target parameters can not be clarified without future experimental and theoretical effort (see also section 2.3.4).

3.2.2   Electron Acceleration

As shown in section 3.2.1 the pre-plasma expansion yielded an under-critical plasma with a peak density of $0.8\ n_c$. This fact enabled the PHELIX laser to propagate through the target. The laser interacts with all electrons in a volumetric coherent manner. Figure 3.6 shows the electron distribution and longitudinal phase space for three different time steps ($460\ fs, 345\ fs, 260\ fs$) of interest prior to the arrival of the main pulse. The corresponding instantaneous on-axis laser intensity acting on the plasma amounts to $6.8 \cdot 10^{19}, 1.9 \cdot 10^{20}, 3.3 \cdot 10^{20} \frac{W}{cm^2}$. During this period, the laser pulse infolds the plasma transversely, as visualized in the overlaid electron density distribution blue colormap in fig. 3.6. This is in close analogy to a metal sphere in the
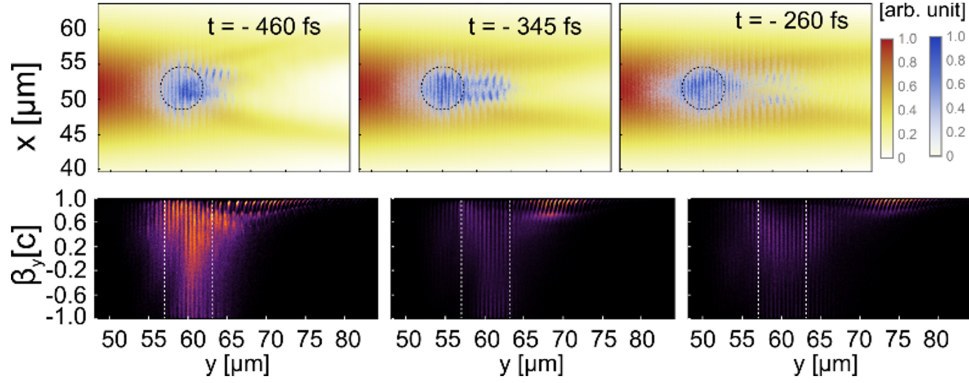
Figure 3.6: Particle-in-cell simulation and analysis. Top: Individually normalized instantaneous laser intensity distribution and electron density distribution in the polarization plane. Bottom: Individually normalized longitudinal electron phase-space density.

doughnut-mode of an optical tweezer [124], only here the doughnut-mode is self-induced by the optical properties of the plasma. The pre-expanded target is marked via dotted lines. The longitudinal phase space shows that the electron population bound to the ionic core shows a behavior as described in section 2.1.3.3. Over time, a substantial fraction of the electrons leave the target and are accelerated to large longitudinal velocities approaching the speed of light with growing intensity (see fig. 3.6), similar to free electrons in a relativistic electromagnetic wave (see section 2.1.3.1). As observable in their density distribution slice in fig. 3.6, they leave the indicated initial target region preferably in laser propagation direction. The laser intensity valley at the same time confines them transversely via ponderomotive forces.

3.2.3   Ion Acceleration

The proton spectra were recorded via a slit spectrometer (for a detailed description see chapter A). The spectrometer covered an opening angle in horizontal dimension of $\pm 4°$. The proton spectra have been evaluated for four
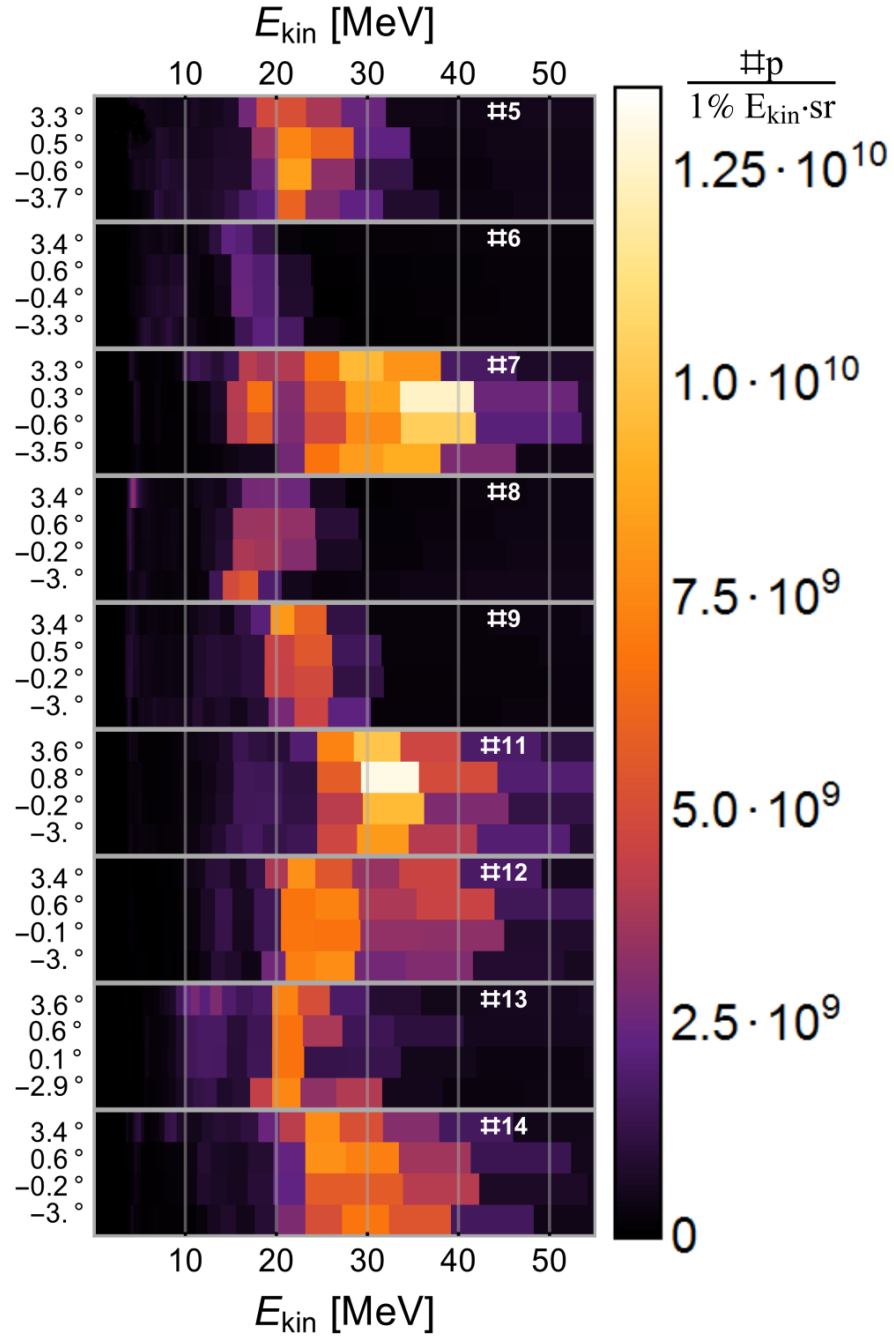
Figure 3.7:   Differential proton spectra for consecutive laser shots for various angles.
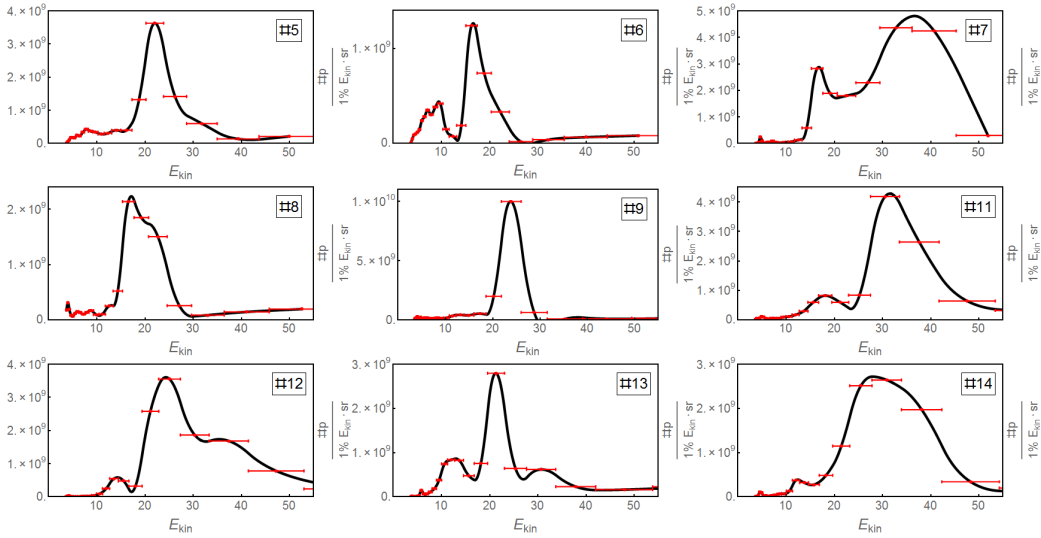
Figure 3.8: Individual proton spectra for consecutive shots exhibiting mono-energetic features.

distinct angles. The deconvolved differential proton spectra of consecutive shoots are shown in figs. 3.7 and 3.8. Shots $\#5 - \#9$ were taken on hollow spheres, shots $\#11 - \#14$ used solid spheres as targets. Shot $\#10$ was a shot without target, which served as a reference shot for the in-line-holography (see section 2.4.1). Figure 3.7 shows all spectra for every angle via a waterfall plot. Figure 3.8 shows the differential spectra of consecutive shoots for one single angle.

All spectra exhibit a narrow energy distribution. In some shoots the FWHM of the peak is so narrow, that it is comparable to the energy-resolution of the spectrometer itself (red error bars in figs. 3.8 and 3.10). There is no evident difference between hollow and solid spheres.

Almost all other experiments which yielded mono-energetic proton spectra (see fig. 1.2), exhibit a exponential background signal, ergo the mono-energetic feature indicating a mixture of different acceleration mechanisms. Such a background signal is completely missing in the presented data. This circumstance implies a complete absence of TNSA like acceleration. This
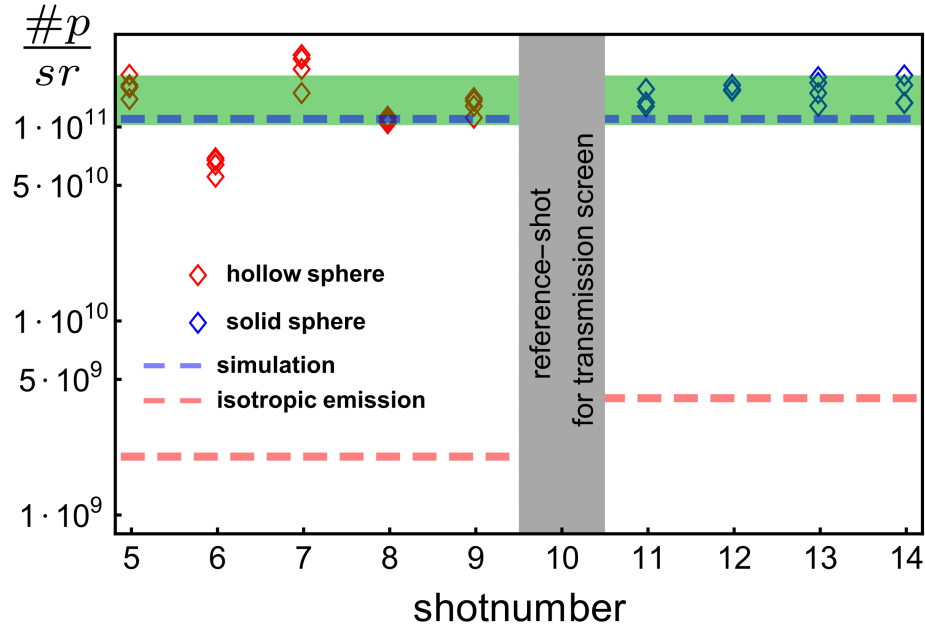
Figure 3.9: Differential proton numbers for consecutive shots. Only protons with an energy above $3.5 MeV$ are taken into account. For comparison a purely isotropic emission into 4π is indicated by the dashed red lines. The blue line depicts the result obtained in the simulation. The green area marks the standard deviation of the experimental data.

allows to use linear plots rather than typically used logarithmic plots.

Figure 3.9 shows the proton spectra integrated over the energy, ergo the particle flux. Each diamond represents one angle of the corresponding shoot. At a first glance solid and hollow spheres deliver similar results. No notable deviation across the angular range of the spectrometer is found. This supports the finding of the severe pre-expansion prior to the main laser-plasma interaction, in which the different target geometries are washed out. Due to the mass limited character of the target one knows to a high degree of certainty the amount of elementary particles contained in the initial target. This allows to estimate the proton flux for the case of an ideal coulomb
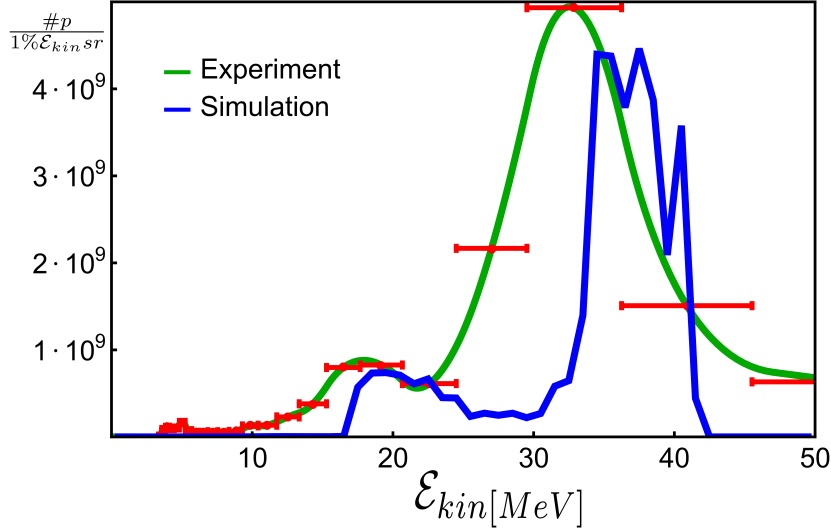
Figure 3.10: Differential proton spectra for experiment (shot # 11, green line) and simulation (blue line). The red error bars show the resolution power of the employed wide angle spectrometer.

explosion. The red dotted line in fig. 3.9 represents the expected particle flux for an isotropic coulomb explosion. Any experimental data close to this value would evidence a volumetric acceleration, in which most of the particles participate in the acceleration mechanism. It is remarkable, that the measured particle flux is roughly two orders of magnitude larger than the estimated value of an ideal coulomb explosion. This circumstance indicates not only a volumetric acceleration mechanism, but also implies a directionality of the accelerated proton beam. Next to the spectral characteristics of the accelerated proton beam this is one of the key results of the presented experiment.

The spectrum obtained via 3D-PIC simulation in comparison to the experiment is shown in fig. 3.10. The simulated spectrum reproduces the experimental data quite well. Also the particle flux (blue line in fig. 3.9) is in
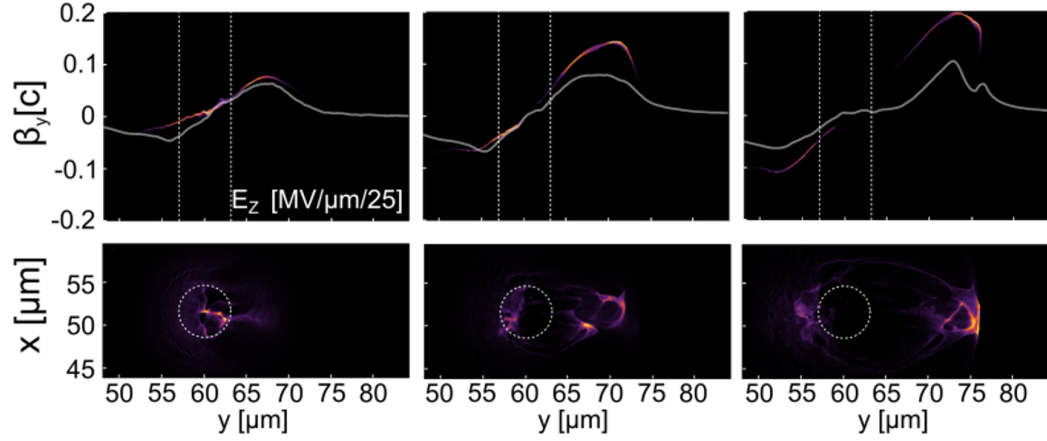
Figure 3.11: Top: Individually normalized longitudinal phase space of protons with superimposed accelerating field. Bottom: Individually normalized proton density distribution in the polarization plane of the laser. The time steps correspond to $(-460\ fs, -345\ fs, -260\ fs)$

very good agreement with the measured data. This shows, that if 3D-PIC codes are provided with the right input parameters, they are able to produce quantitative results.

Since protons constitute the lightest ions they follow the electron jet shown in fig. 3.6. In consequence protons are dragged preferably toward the intensity valley as well (see fig. 3.11). Figure 3.11 evidences that the accelerating field distribution remains stable over an extended period of time. The protons develop a negative energy chirp in the monotonic slope of the accelerating field. When the fastest protons reach the peak of the field, which amounts to $\approx 2.5 \frac{MV}{\mu m}$, the tail of the bunch catches up, observable in the superimposed proton phase space. The narrowest energy spread is reached at $t = -50\ fs$ with 3.5% (1 MeV FWHM @ 29 MeV).

The temporal evolution of the spectrum is shown in fig. 3.12. It is interesting to note, that the energy peak position of the detaching proton bunch closely follows the red line superimposed in fig. 3.12 until $t = -260\ fs$. It represents the cumulatively time and spatially integrated laser intensity,
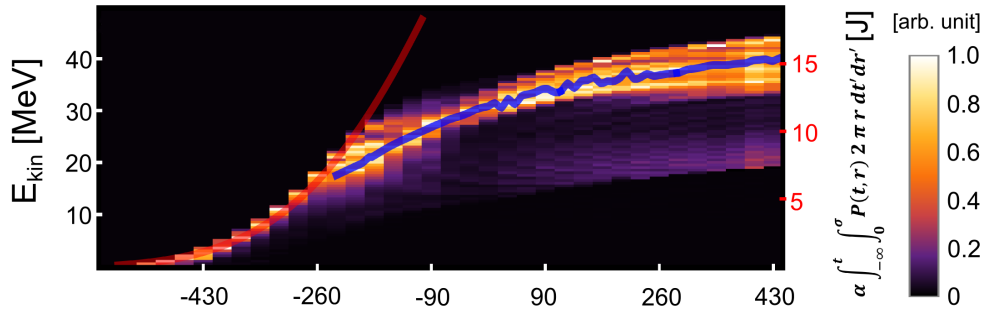
Figure 3.12: Temporal evolution of the spectrum in forward direction. The red line shows the laser energy which passed through the target. The blue line shows the result of a charge repulsion calculation. A detailed description is given in the main text.

i.e. the laser energy that has passed though the plasma up until the respective time. The proportionality factor between the accumulated energy and central bunch energy is estimated in this case to $\frac{2\,MeV}{J}$. At $t = -260\ fs$ the bunch energy no longer follows this favorable scaling, which would otherwise result in a proton bunch with $163\ MeV$ energy. Over the time the electron population in the target gets more and more depleted. Hence, the acceleration due to the electron jet is replaced gradually by Coulomb repulsion forces of the remaining heavier ions (Carbon and Oxygen). Extracting the three-dimensional ion density distributions at time $t = -230\ fs,$ the further evolution of the proton bunch can be well described by considering pure Coulomb repulsion (see methods). The time evolution of the proton energy distribution resulting from this calculation is visualized by the blue line in fig. 3.12. In the light of the above explanation, one can conclude, that the initial acceleration phase, which only lasts until $\approx -345\ fs$ before the laser intensity peak, terminates due to strong electron heating and the depletion of electrons (see fig. 3.6). The remaining time is dominated by Coulomb repulsion between the leading protons from carbon and oxygen ions (see section 2.2.4).
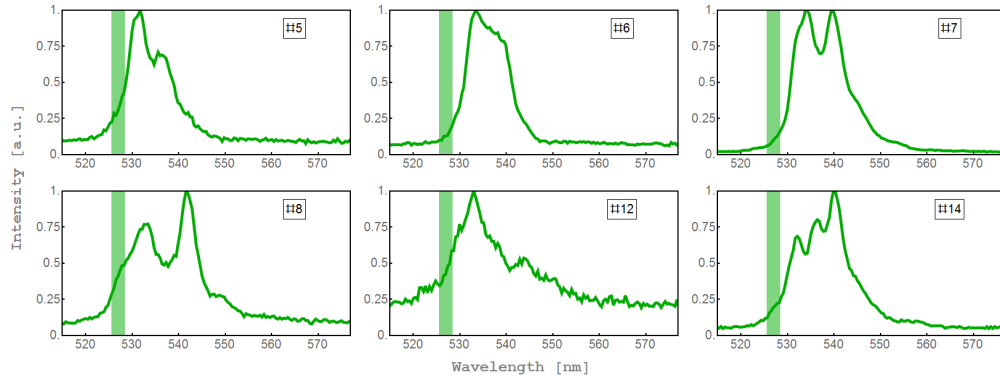
Figure 3.13: Frequency spectra of the light which was reflected form the target. The green bar shows bandwidth and position of the second harmonic of the laser system.

3.2.4   Reflected Light

As stated in section 2.4.2 the reflected light of a laser-plasma interaction can serve as a diagnostic tool. This was the intention in installing a back scatter diagnostic in the experiment as described in section 3.2. The last turning mirror of the experiment was a HR dielectric mirror. Unfortunately the transmission for the fundamental wavelength was so low, that we didn't measure any signal near 1054 nm. At the second harmonic with an wavelength of 527 nm the mirror had a transmission of approximately 30%. The experimental results are shown in fig. 3.13.   A red shifted spectrum with increased bandwidth of $> 2\%$ is observed. The initial bandwidth of the laser amounts to 0.3% . Normally one would interpret this results as the velocity of the critical density as described in [113, 115]. In section 3.2.1 it was shown that the target has no (relativistic-)critical density region. This implies the necessity for a different interpretation. As seen in section 3.2.2 the laser interacts in a volumetric fashion with the target. The coherence of the laser is transferred onto the bound electrons (see fig. 3.6). A coherent mechanism could be envisioned.

Unfortunately the amount of back scattered light was only in the order of
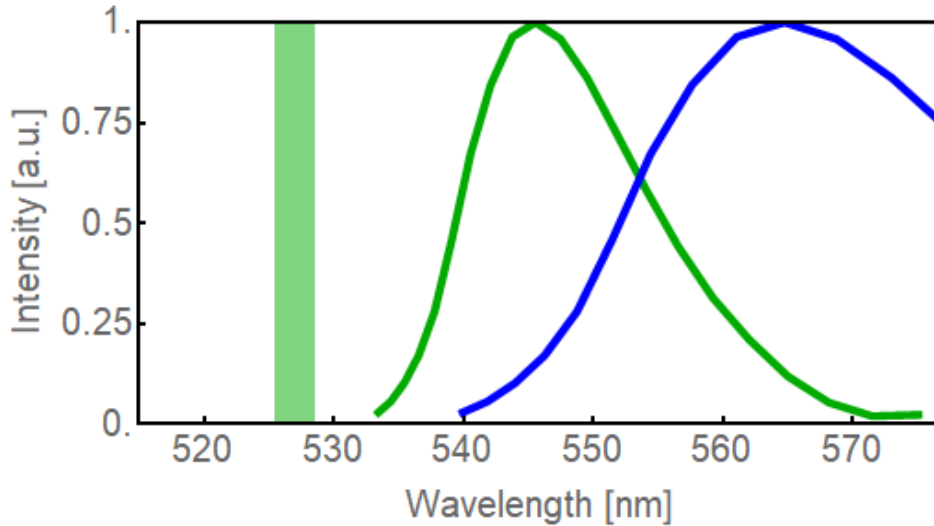
Figure 3.14: Reconstructed spectrum of the back scattered light. The green curve is obtained via the single Doppler shift obtained with eq. (2.106). The blue curve is obtained with eq. (2.107) (twice the redshift). The green bar shows bandwidth and position of the second harmonic of the laser system.

a few hundred nJ, therefore the back scattered light can not be seen directly in the 3D PIC simulation, due to the fact that only single precision is used in the simulation, to efficiently use the limited memory of the used graphic cards.

There is another way to extract some information from the simulation concerning the back scattered light. Under the assumption, that the number of back scattered photons is directly proportional to the number of incoming photons and also the number of electrons, one can calculate the product of intensity and electron density. The spatial integral over this quantity would encode the intensity of the back scattered light. The velocity of the center of mass of this quantity encodes the amount of redshift. By this means one can reconstruct a rough spectrum from the simulations for the back scattered light, which is shown in fig. 3.14.

The reconstructed spectrum fits the experimental results qualitatively, if

one only applies the relativistic redshift once and not twice, like in the case of an relativistic mirror. This can be explained in the following manner. The electron density is modulated with the wavelength of the laser. The target can be seen as a relativistic moving Fabry-Perot-interferometer, which would then explain, why the relativistic redshift must only be applied once. This interpretation is to a certain extend quite speculative at the moment and should be consolidated by additional 3D PIC simulations (with particle tracking) and additional experiments in the future. The radiation should be measured for various angles individually to observe the blue-shift into forward direction and the transverse emitted radiation parallel and perpendicular to the laser polarization. Relativistically and coherently driven micro plasmas could pave the way to interesting new radiation sources.

Chapter 4

Summary and Outlook

This work describes the interaction of a subfocus-sized masslimited target, with an high-power laser pulse. The pre-expansion of the target played a vital role for the encountered laser-plasma interaction and was characterized via an in-line-holography during the experiment. It was found, that the target expands prior to the main interaction such that the main laser pulse interacts with a subfocus-sized, under-critical target.

Normally under-critical targets are used for electron acceleration. To a certain extend it is surprising, that protons can be accelerated efficiently in an under-critical target, and that it was not observed before. The reason for that is, that the specific size of just a few μm in combination with relative low target density can only be achieved by the three-dimensional expansion of very small targets.

The accelerated proton beam from such a target exhibited quite unique properties. The proton spectrum exhibited a mono-energetic shape. The particle numbers showed that a large fraction of the initial target gets accelerated into the forward direction. A demanding 3D-PIC simulation was able to reproduce the experimental results quantitatively. The simulation revealed, that the underlying acceleration process can be divided into two parts. In a first step a ponderomotively collimated electron current is driven
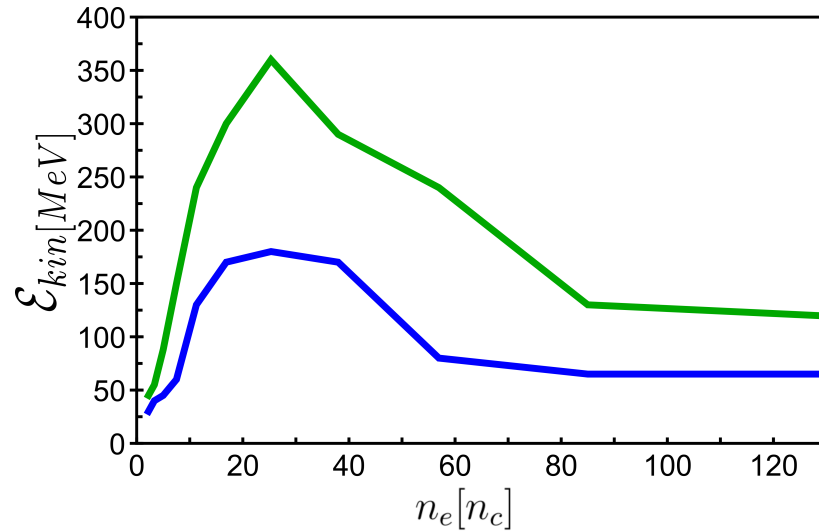
Figure 4.1: 3D PIC parameter scan for a sphere with a radius of 2 μm and varying density using CALA like laser parameters. The green curve correspond two a pulse duration of 30 fs, the blue depicts a pulse duration of 100 fs.

through the target which drags along the protons. In a second stage the target is depleted from electrons and the protons undergo a directed coulomb explosion from the remaining carbons. The pulling from the electrons and the consecutive pushing from the carbons leads to a phase space rotation and ultimately yields mono energetic protons. While in the first stage the laser couples energy into the ion beam, the second stage on the other hand can be seen as a relaxation stage, were stored energy is released. The transition between those two stages occurred quite early during the interaction.

Future experiments and simulations will be needed to identify proper target size and amount of pre-expansion to enhance the target performance. In cooperation with the group of Hartmuth Ruhl a parameter scan via 3D-PIC simulations was conducted for a CALA like lasers system. Figure 4.1 shows the obtainable maximum proton energies for different target densities. The radius of the target was 2 μm. The laser had a pulse energy of $\approx 40\ J$

. The pulse duration was 30 fs (green graph in fig. 4.1) and 100 fs (blue graph in fig. 4.1).

To conduct experiments with the appropriate target size and density, a deeper understanding and/or control over the target pre-expansion is essential. This questions are currently investigated with a second Paul trap at the ZEUS laser system in Garching.

Even if the presented acceleration mechanism and its technical implementation is rather complex, the advantageous proton beam parameters motivate future efforts in experiment and simulation. The coherent nature of the acceleration process and possible new radiation sources constitute interesting questions for future research with mass-limited targets, that can be provided via the developed Paul trap.

The Paul trap represents a nice tool to identify and demonstrate the optimum parameters for the presented volumetric acceleration mechanisms. The absence of EMP, back reflection and debris are strong technical arguments for the implementation of mass-limited, near-critical targets at up-coming petawatt facilities such as ATLAS 3000.

Appendix A

Particle Spectrometer

A slit spectrometer was used in the experiment. Hereby a magnetic field disperses different particle momenta spatially. Different particle species can have the same momentum and ergo the same dispersion. To obtain proton spectra degraders were used to prevent the carbon ions to reach the detector (Protons have a higher penetration depth than carbon ions with the same momentum). Consequently heavy ion spectra (in this case carbon and oxygen) are sacrificed for spatial information.

The magnetic slit spectrometer fig. A.1 consists out of two dipole magnets. The first magnet was located 240 mm behind the target. The magnet had a length of 240 mm and a gap of 170 mm . The entry slit was made out of 20 mm thick tungsten blocks on a 60 mm thick steel front plate and had a width of 500 μm. Its orientation was parallel to the laser polarization. The distance between detector and slit amounted to 620 mm. A second dipole magnet was placed directly in front of the detector to increase the dispersion further. The second magnet consisted out of three gaps with 45 mm width and had a length of 120 mm. The magnetic field in the center of the first dipole magnet amounts to 0.1 T and 0.3 T for the second. A 3D particle tracking was employed to account for the inhomogeneous magnetic fields of the spectrometer. The necessary magnetic field maps were measured with a
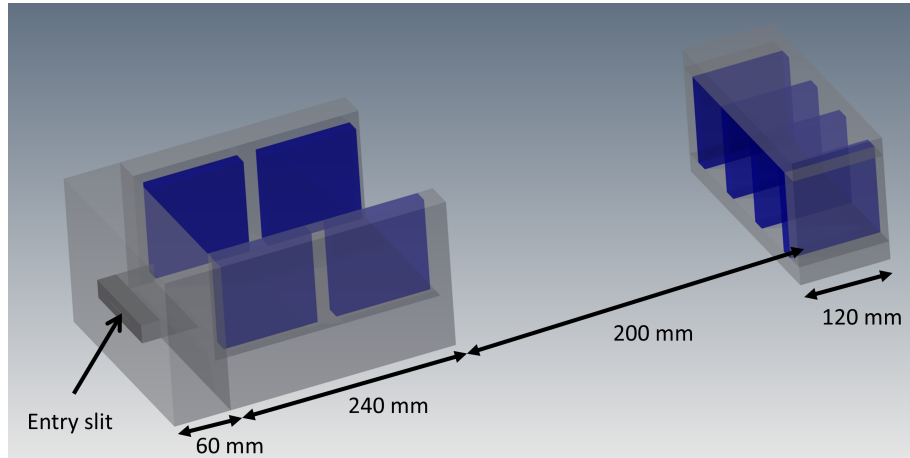
Figure A.1: Ion Spectrometer.

three axis hall probe.

The evaluation routine for the proton spectra is presented exemplary on shoot # 11 in fig. A.2. Bas-TR image-plates (IP) were used as detectors. They were covered in 100 μm thick aluminum foil. Parts of the detector were additionally covered with 0.9 mm thick CR39 nuclear track detectors wrapped in 15 μm thick aluminum. Positions of CR39 are indicated in fig. A.2 by yellow squares. The IP's were scanned with an MS-FLA5100 scanner from Fuji with a resolution of 100 μm. In the case of saturation (saturation only occurred for carbon data) the image plates were scanned twice. The obtained raw data was converted into photostimulated luminescence (PSL) using Fuji's conversion plugin for ImageJ. Scans were composed into an HDR image shown in fig. A.2. A via particle tracing obtained energy-angle map was aligned within the PSL image. Some important iso- energy lines for protons are shown in fig. A.2. Protons with energy of 3.4 MeV are able to penetrate the 100 μm thick aluminum shielding of the IP's representing the low energy cut off of the spectrometer. Protons with 11 MeV are able to penetrate regions which were additionally covered with CR39. At regions where protons with an energy of 24.8 MeV would be situated
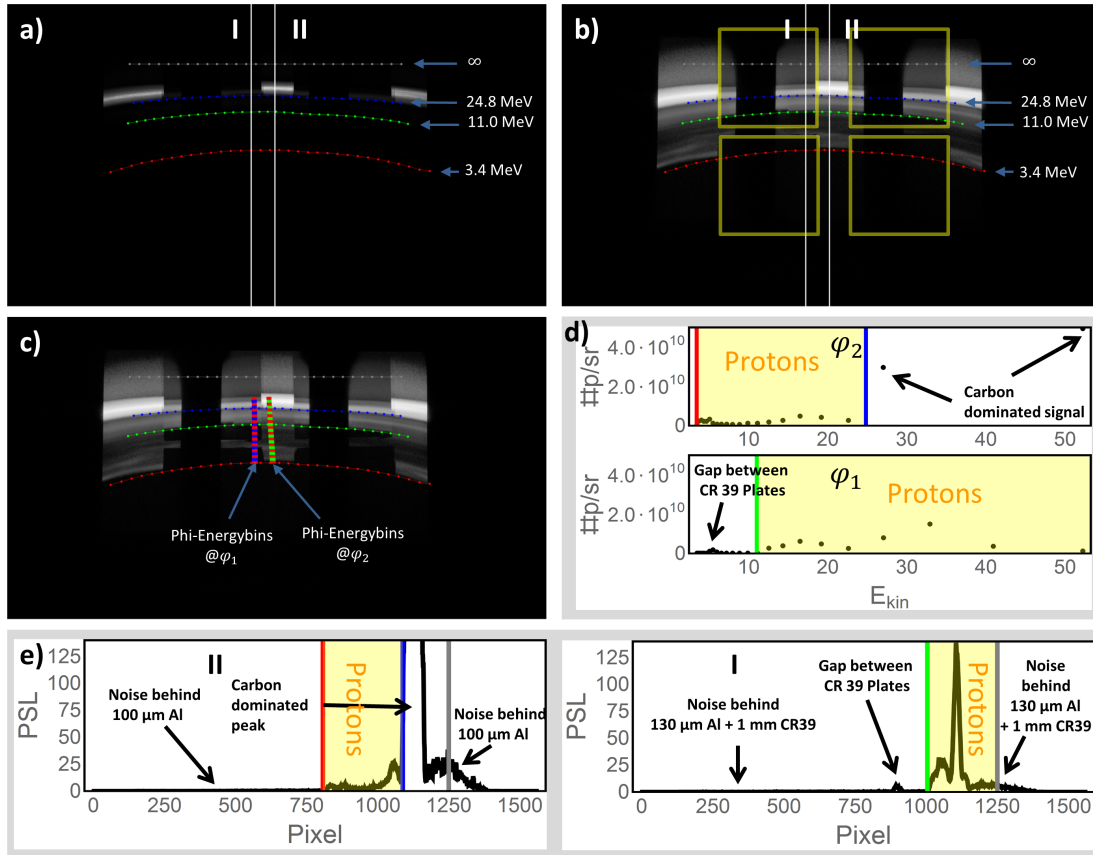
Figure A.2: Image plates raw data and evaluation: a) raw data with iso-energy lines for protons, b) logarithmic representation of a) ,yellow squares indicate the position of CR 39 plates c) energy-angle bins on the detector d) spectra obtained from c) e) PSL raw data lineout.

C_6^+ - ions with 75 MeV are able to penetrate the 100 μm thick aluminum. C_6^+ - ions with energies exceeding 249 MeV would be able to penetrate the 0.9 mm thick CR39 detector together with 130 μm alumina. Protons with the same deflection correspond to an kinetic energy of 83 MeV. In no shoot we recorded image plate signal at these deflections. This implies that we were able to discriminate uniquely proton signal from carbon signal for the proton energy range spanning from 3.4 to 83 MeV (yellow squares fig. A.2).

Line outs of the PSL signal are shown in fig. A.2. The left line out shows the PSL signal which was shielded by 100 μm aluminum (Position II in fig. A.2). The right line out shows the PSL signal which was shielded by 130 μm aluminum and 0.9 mm CR39 (Position I in fig. A.2). Due the different degraders regions of the IP can be identified that can only be reached by protons indicated as yellow regions in fig. A.2. The cut off lines in fig. A.2 are shown as vertical lines with corresponding color. Energy-angle bins were defined as shown in fig. A.2 (blue, green and red quadrilaterals). Hereby the energy bin width has been chosen in such a way that corresponding bins in detector space had a height of 1500 μm , which corresponds to the slit projection on the IP. Due to the negligible angle dependence of the raw data signal, the angle bin width has been arbitrarily chosen to be 2, 792 $mrad$. Different angle bin sizes yielded similar results. One energy-angle bin contains about 450 pixel of the IP. Pixel which were partially covered by a bin were weighted according to their overlap. The conversion function from PSL to #p/pixel has been calibrated with a Tandem accelerator (MLL). The energy loss of the protons in the degraders has been taken into account for each bin individually. The final spectra are obtained at the borders of the CR39. Energy bins with values between 3.5 MeV and 22 MeV were evaluated behind $100\mu m$ aluminum (fig. A.2 red-green quadrilaterals). For energies above 22 MeV the IP signal behind CR39 was used (fig. A.2 red-blue quadrilaterals). The corresponding spectra are shown in fig. A.2. Also here the cut off lines are indicated by vertical lines with corresponding color. Yellow boxes mark re-

gions were the signal is purely caused by protons. The resulting final spectra are shown in fig. 3.8. Regarding carbon ion energies only weak statements can be made based on cutoff lines. In the experiment $100\mu m$ aluminum was penetrated by carbon ions with a kinetic energy of at least 75 MeV. The absence of a cutoff line behind CR39 in our shoots evidences that the carbon energies were smaller than 250 MeV.

Bibliography

[1] P. Hilz, T. M. Ostermayr, A. Huebl, V. Bagnoud, B. Borm, M. Bussmann, M. Gallei, J. Gebhard, D. Haffa, J. Hartmann and et al., *Isolated proton bunch acceleration by a petawatt laser pulse*, Nature Communications **9**, (2018).

[2] Andrew Ayton and Preston [Bart] Sir Philip, *The Battle of Crécy, 1346* (Boydell & Brewer, Suffolk, 2017).

[3] Juliet R. V. Barker, Bernard Cornwell and John Gilkes, *Agincourt: the king, the campaign, the battle* (Abacus, London, 2015).

[4] Eugenie Samuel Reich, *Finding puts brakes on faster-than-light neutrinos*, Nature (2011).

[5] A. Dogariu, A. Kuzmich and L. J. Wang, *Transparent anomalous dispersion and superluminal light-pulse propagation at a negative group velocity*, Physical Review A **63**, (2001).

[6] Raymond Y. Chiao, Claus Ropers, Daniel Solli and Jandir M. Hickmann, *Faster-than-light propagations and their applications*, Coherence and Quantum Optics VIII 109 (2003).

[7] W. C. Röntgen, *Über Eine Neue Art von Strahlen*, (1949).

[8] W. Friedrich, P. Knipping and M. Laue, *Interferenzerscheinungen bei Röntgenstrahlen*, Annalen der Physik **346**, 971 (1913).

[9] M. Knoll and E. Ruska, *Das Elektronenmikroskop*, Zeitschrift für Physik **79**, 699 (1932).

[10] P. Rai-Choudhury, *Handbook of microlithography, micromachining, and microfabrication* (SPIE Optical Engineering Press, Bellingham, WA, 1997).

[11] W. D. Kilpatrick, *Criterion for Vacuum Sparking Designed to Include Both rf and dc*, Review of Scientific Instruments **28**, 824 (1957).

[12] Thomas P. Wangler, *RF linear accelerators* (Wiley-VCH Verlag, Weinheim, 2017).

[13] SLAC By The Numbers, https://www6.slac.stanford.edu/by-the-numbers.

[14] https://www.xfel.eu/anlage/ueberblick/zahlen_amp_fakten/index_ger.html.

[15] John Breuer and Peter Hommelhoff, *Laser-Based Acceleration of Non-relativistic Electrons at a Dielectric Structure*, Physical Review Letters **111**, (2013).

[16] A. Henig, D. Kiefer, M. Geissler, S. G. Rykovanov, R. Ramis, R. Hörlein, J. Osterhoff, Zs. Major, L. Veisz, S. Karsch and et al., *Laser-Driven Shock Acceleration of Ion Beams from Spherical Mass-Limited Targets*, Physical Review Letters **102**, (2009).

[17] Peter S. Ebey, James M. Dole, Drew A. Geller, James K. Hoffer, John Morris, Arthur Nobile, Jon R. Schoonover, Doug Wilson, Mark Bonino, David Harding and et al., *Overview of Recent Tritium Target Filling, Layering, and Material Testing at Los Alamos National Laboratory in Support of Inertial Fusion Experiments*, Fusion Science and Technology **54**, 375 (2008).

[18] F. Wagner, O. Deppert, C. Brabetz, P. Fiala, A. Kleinschmidt, P. Poth, V. A. Schanz, A. Tebartz, B. Zielbauer, M. Roth and et al., *Maximum Proton Energy above 85 MeV from the Relativistic Interaction of Laser Pulses with Micrometer ThickCH2Targets*, Physical Review Letters **116**, (2016).

[19] Charlotte A. J. Palmer, N. P. Dover, I. Pogorelsky, M. Babzien, G. I. Dudnikova, M. Ispiriyan, M. N. Polyanskiy, J. Schreiber, P. Shkolnikov, V. Yakimenko and et al., *Monoenergetic Proton Beams Accelerated by a Radiation Pressure Driven Shock*, Physical Review Letters **106**, (2011).

[20] Dan Haberberger, Sergei Tochitsky, Frederico Fiuza, Chao Gong, Ricardo A. Fonseca, Luis O. Silva, Warren B. Mori and Chan Joshi, *Collisionless shocks in laser-produced plasma generate monoenergetic high-energy proton beams*, Nature Physics **8**, 95 (2011).

[21] H. Schwoerer, S. Pfotenhauer, O. Jačkel, K.-U. Amthor, B. Liesfeld, W. Ziegler, R. Sauerbrey, K. W. D. Ledingham and T. Esirkepov, *Laser-plasma acceleration of quasi-monoenergetic protons from microstructured targets*, Nature **439**, 445 (2006).

[22] T. M. Ostermayr, D. Haffa, P. Hilz, V. Pauw, K. Allinger, K.-U. Bamberg, P. Böhl, C. Bömer, P. R. Bolton, F. Deutschmann and et al., *Proton acceleration by irradiation of isolated spheres with an intense laser pulse*, Physical Review E **94**, (2016).

[23] S. Ter-Avetisyan, B. Ramakrishna, R. Prasad, M. Borghesi, P. V. Nickles, S. Steinke, M. Schnürer, K. I. Popov, L. Ramunno, N. V. Zmitrenko and et al., *Generation of a quasi-monoergetic proton beam from laser-irradiated sub-micron droplets*, Physics of Plasmas **19**, 073112 (2012).

[24] B. M. Hegelich, B. J. Albright, J. Cobble, K. Flippo, S. Letzring, M. Paffett, H. Ruhl, J. Schreiber, R. K. Schulze, J. C. Fernndez and et al.,

Laser acceleration of quasi-monoenergetic MeV ion beams, Nature **439**, 441 (2006).

[25] S. Kar, K. F. Kakolee, B. Qiao, A. Macchi, M. Cerchez, D. Doria, M. Geissler, P. Mckenna, D. Neely, J. Osterholz and et al., *Ion Acceleration in Multispecies Targets Driven by Intense Laser Radiation Pressure*, Physical Review Letters **109**, (2012).

[26] S. Steinke, P. Hilz, M. Schnürer, G. Priebe, J. Bränzel, F. Abicht, D. Kiefer, C. Kreuzer, T. Ostermayr, J. Schreiber and et al., *Stable laser-ion acceleration in the light sail regime*, Physical Review Special Topics - Accelerators and Beams **16**, (2013).

[27] D Jung, L Yin, B J Albright, D C Gautier, S Letzring, B Dromey, M Yeung, R Hörlein, R Shah, S Palaniyappan and et al., *Efficient carbon ion beam generation from laser-driven volume acceleration*, New Journal of Physics **15**, 023007 (2013).

[28] Lev D. Landau and Lifsic Evgenij M., *Fluid dynamics* (Butterworth-Heinemann, Oxford, 1995).

[29] Herbert B. Callen, *Thermodynamics: an introduction to the physical theories of equilibrum thermostatistics and irreversible thermodynamics* (Wiley, New York, 1970).

[30] Bernard Diu and Freimut Marschner, *Grundlagen der statistischen Physik: ein Lehrbuch mit Übungen* (De Gruyter., Berlin, YEAR).

[31] Sean G. Ryan and Andrew Norton, *Stellar evolution and nucleosynthesis* (Cambridge University Press, Cambridge, UK, 2010).

[32] *Der neue Kosmos* (Springer, Berlin Heidelberg, 2002).

[33] Richard Fitzpatrick, *Plasma physics: an introduction* (CRC Press, Boca Raton, 2015).

[34] Francis F. Chen, *Introduction to plasma physics and controlled fusion* (Springer, Cham, 2018).

[35] S. P. D. Mangles, C. D. Murphy, Z. Najmudin, A. G. R. Thomas, J. L. Collier, A. E. Dangor, E. J. Divall, P. S. Foster, J. G. Gallacher, C. J. Hooker and et al., *Monoenergetic beams of relativistic electrons from intense laser-plasma interactions*, Nature **431**, 535 (2004).

[36] Hyung Taek Kim, Ki Hong Pae, Hyuk Jin Cha, I Jong Kim, Tae Jun Yu, Jae Hee Sung, Seong Ku Lee, Tae Moon Jeong and Jongmin Lee, *Enhancement of Electron Energy to the Multi-GeV Regime by a Dual-Stage Laser-Wakefield Accelerator Pumped by Petawatt Laser Pulses*, Physical Review Letters **111**, (2013).

[37] A. J. Gonsalves, K. Nakamura, J. Daniels, C. Benedetti, C. Pieronek, T. C. H. De Raadt, S. Steinke, J. H. Bin, S. S. Bulanov, J. Van Tilborg and et al., *Petawatt Laser Guiding and Electron Beam Acceleration to 8 GeV in a Laser-Heated Capillary Discharge Waveguide*, Physical Review Letters **122**, (2019).

[38] A. Higginson, R. J. Gray, M. King, R. J. Dance, S. D. R. Williamson, N. M. H. Butler, R. Wilson, R. Capdessus, C. Armstrong, J. S. Green and et al., *Near-100 MeV protons via a laser-driven transparency-enhanced hybrid acceleration scheme*, Nature Communications **9**, (2018).

[39] Raymond E. March and John F. J. Todd, *Quadrupole ion trap mass spectrometry* (Wiley, Hoboken (N.J.), 2005).

[40] V. N. Gheorghe, F. G. Major and G. Werth, *Charged Particle Traps* (Springer-Verlag Berlin Heidelberg, New York, 2005).

[41] P. L. Kapitza and P. A. M. Dirac, *The reflection of electrons from standing light waves*, Mathematical Proceedings of the Cambridge Philosophical Society **29**, 297 (1933).

[42] P. H. Bucksbaum, D. W. Schumacher and M. Bashkansky, *High-Intensity Kapitza-Dirac Effect*, Physical Review Letters **61**, 1182 (1988).

[43] Daniel L. Freimund, Kayvan Aflatooni and Herman Batelaan, *Observation of the Kapitza-Dirac effect*, Nature **413**, 142 (2001).

[44] Landau Lev Davidovič, Lifşic Evgenij Michajloviç. and Paul Ziesche, *Mechanik* (Akademie Verlag, Berlin, 1990).

[45] Paul Gibbon, *Short pulse laser interactions with matter: an introduction* (Imperial College Press, London, 2005).

[46] A. E. Kaplan and A. L. Pokrovsky, *Fully Relativistic Theory of the Ponderomotive Force in an Ultraintense Standing Wave*, Physical Review Letters **95**, (2005).

[47] D. Bauer, P. Mulser and W. H. Steeb, *Relativistic Ponderomotive Force, Uphill Acceleration, and Transition to Chaos*, Physical Review Letters **75**, 4622 (1995).

[48] G. Malka, E. Lefebvre and J. L. Miquel, *Experimental Observation of Electrons Accelerated in Vacuum to Relativistic Energies by a High-Intensity Laser*, Physical Review Letters **78**, 3314 (1997).

[49] Kirk T. Mcdonald, *Comment on "Experimental Observation of Electrons Accelerated in Vacuum to Relativistic Energies by a High-Intensity Laser"*, Physical Review Letters **80**, 1350 (1998).

[50] P. Mora and B. Quesnel, *Comment on "Experimental Observation of Electrons Accelerated in Vacuum to Relativistic Energies by a High-Intensity Laser"*, Physical Review Letters **80**, 1351 (1998).

[51] E. Lefebvre, G. Malka and J.-L. Miquel, *Lefebvre, Malka, and Miquel Reply:*, Physical Review Letters **80**, 1352 (1998).

[52] Peter Hilz, Diploma Thesis, LMU, 2010.

[53] T. M. Ostermayr, J. Gebhard, D. Haffa, D. Kiefer, C. Kreuzer, K. Allinger, C. Bömer, J. Braenzel, M. Schnürer, I. Cermak and et al., *A transportable Paul-trap for levitation and accurate positioning of micron-scale particles in vacuum for laser-plasma experiments*, Review of Scientific Instruments **89**, 013302 (2018).

[54] Tobias Ostermayr, Dissertation, LMU, 2018.

[55] Tobias Ostermayr, Master Thesis, LMU, 2012.

[56] Daniel Haffa, Master Thesis, LMU, 2014.

[57] Johannes Gebhard, Master Thesis, LMU, 2016.

[58] J D Lawson, *Lasers and Accelerators*, IEEE Transactions on Nuclear Science **26**, 4217 (1979).

[59] P.m. Woodward, *A method of calculating the field over a plane aperture required to produce a given polar diagram*, Journal of the Institution of Electrical Engineers - Part IIIA: Radiolocation **93**, 1554 (1946).

[60] E. Esarey, C. B. Schroeder and W. P. Leemans, *Physics of laser-driven plasma-based electron accelerators*, Reviews of Modern Physics **81**, 1229 (2009).

[61] John David. Jackson and Müller Kurt, *Klassische Elektrodynamik* (De Gruyter, Berlin, 2002).

[62] O. Klein and Y. Nishina, *Über die Streuung von Strahlung durch freie Elektronen nach der neuen relativistischen Quantendynamik von Dirac*, Zeitschrift für Physik **52**, 853 (1929).

[63] T. G. Blackburn, Radiation reaction in electron-beam interactions with high-intensity lasers, 2019.

[64] T. G. Blackburn, D. Seipt, S. S. Bulanov and M. Marklund, *Radiation beaming in the quantum regime*, Physical Review A **101**, (2020).

[65] V. I. Veksler, *The principle of coherent acceleration of charged particles*, The Soviet Journal of Atomic Energy **2**, 525 (1957).

[66] J. Fuchs, C. A. Cecchetti, M. Borghesi, T. Grismayer, E. D'Humieres, P. Antici, S. Atzeni, P. Mora, A. Pipahl, L. Romagnani and et al., *Laser-Foil Acceleration of High-Energy Protons in Small-Scale Plasma Gradients*, Physical Review Letters **99**, (2007).

[67] S. C. Wilks, A. B. Langdon, T. E. Cowan, M. Roth, M. Singh, S. Hatchett, M. H. Key, D. Pennington, A. Mackinnon, R. A. Snavely and et al., *Energetic proton generation in ultra-intense laser-solid interactions*, Physics of Plasmas **8**, 542 (2001).

[68] Stephen P. Hatchett, Curtis G. Brown, Thomas E. Cowan, Eugene A. Henry, Joy S. Johnson, Michael H. Key, Jeffrey A. Koch, A. Bruce Langdon, Barbara F. Lasinski, Richard W. Lee and et al., *Electron, photon, and ion beams from the relativistic interaction of Petawatt laser pulses with solid targets*, Physics of Plasmas **7**, 2076 (2000).

[69] R. A. Snavely, M. H. Key, S. P. Hatchett, T. E. Cowan, M. Roth, T. W. Phillips, M. A. Stoyer, E. A. Henry, T. C. Sangster, M. S. Singh and et al., *Intense High-Energy Proton Beams from Petawatt-Laser Irradiation of Solids*, Physical Review Letters **85**, 2945 (2000).

[70] Hiroyuki Daido, Mamiko Nishiuchi and Alexander S Pirozhkov, *Review of laser-driven ion sources and their applications*, Reports on Progress in Physics **75**, 056401 (2012).

[71] F. Brunel, *Not-so-resonant, resonant absorption*, Physical Review Letters **59**, 52 (1987).

[72] W. L. Kruer and Kent Estabrook, *J x B heating by very intense laser light*, Physics of Fluids **28**, 430 (1985).

[73] Yun-Qian Cui, Wei-Min Wang, Zheng-Ming Sheng, Yu-Tong Li and Jie Zhang, *Laser absorption and hot electron temperature scalings in laser-plasma interactions*, Plasma Physics and Controlled Fusion **55**, 085008 (2013).

[74] P. Mora, *Plasma Expansion into a Vacuum*, Physical Review Letters **90**, (2003).

[75] J. Fuchs, P. Antici, E. D'Humieres, E. Lefebvre, M. Borghesi, E. Brambrink, C. A. Cecchetti, M. Kaluza, V. Malka, M. Manclossi and et al., *Laser-driven proton scaling laws and new paths towards energy increase*, Nature Physics **2**, 48 (2005).

[76] J. Schreiber, F. Bell, F. Grüner, U. Schramm, M. Geissler, M. Schnürer, S. Ter-Avetisyan, B. M. Hegelich, J. Cobble, E. Brambrink and et al., *Analytical Model for Ion Acceleration by High-Intensity Laser Pulses*, Physical Review Letters **97**, (2006).

[77] S. C. Wilks, W. L. Kruer, M. Tabak and A. B. Langdon, *Absorption of ultra-intense laser pulses*, Physical Review Letters **69**, 1383 (1992).

[78] A. Pak, S. Kerr, N. Lemos, A. Link, P. Patel, F. Albert, L. Divol, B. B. Pollock, D. Haberberger, D. Froula and et al., *Collisionless shock*

acceleration of narrow energy spread ion beams from mixed species plasmas using 1 *µm lasers*, Physical Review Accelerators and Beams **21**, (2018).

[79] A P L Robinson, P Gibbon, M Zepf, S Kar, R G Evans and C Bellei, *Relativistically correct hole-boring and ion acceleration by circularly polarized laser pulses*, Plasma Physics and Controlled Fusion **51**, 024004 (2009).

[80] Natsumi Iwata, Sadaoki Kojima, Yasuhiko Sentoku, Masayasu Hata and Kunioki Mima, *Plasma density limits for hole boring by intense laser pulses*, Nature Communications **9**, (2018).

[81] T. Esirkepov, M. Yamagiwa and T. Tajima, *Laser Ion-Acceleration Scaling Laws Seen in Multiparametric Particle-in-Cell Simulations*, Physical Review Letters **96**, (2006).

[82] G. Marx, *Interstellar Vehicle Propelled By Terrestrial Laser Beam*, Nature **211**, 22 (1966).

[83] J. F. L. Simmons and C. R. Mcinnes, *Was Marx right? or How efficient are laser driven interstellar spacecraft?*, American Journal of Physics **61**, 205 (1993).

[84] Andrea Macchi, Silvia Veghini and Francesco Pegoraro, *"Light Sail" Acceleration Reexamined*, Physical Review Letters **103**, (2009).

[85] Centre for Advanced Laser Applications, https://www.cala-laser.de/.

[86] GIST, https://www.ibs.re.kr/eng/sub02_03_05.do.

[87] F. Peano, R. A. Fonseca and L. O. Silva, *Dynamics and Control of Shock Shells in the Coulomb Explosion of Very Large Deuterium Clusters*, Physical Review Letters **94**, (2005).

[88] A. E. Kaplan, B. Y. Dubetsky and P. L. Shkolnikov, *Shock Shells in Coulomb Explosions of Nanoclusters*, Physical Review Letters **91**, (2003).

[89] K. Nishihara, H. Amitani, M. Murakami, S.v. Bulanov and T.zh. Esirkepov, *High energy ions generated by laser driven Coulomb explosion of cluster*, Nuclear Instruments and Methods in Physics Research Section A: Accelerators, Spectrometers, Detectors and Associated Equipment **464**, 98 (2001).

[90] T. Ditmire, J. W. G. Tisch, E. Springate, M. B. Mason, N. Hay, R. A. Smith, J. Marangos and M. H. R. Hutchinson, *High-energy ions produced in explosions of superheated atomic clusters*, Nature **386**, 54 (1997).

[91] Isaac Newton, *Philosophiae naturalis principia mathematica*, (1687).

[92] V. Yu. Bychenkov and V. F. Kovalev, *Relativistic coulomb explosion of spherical microplasma*, JETP Letters **94**, 97 (2011).

[93] Pulsar Physics, http://www.pulsar.nl/gpt/.

[94] J. Braenzel, A. A. Andreev, K. Platonov, M. Klingsporn, L. Ehrentraut, W. Sandner and M. Schnürer, *Coulomb-Driven Energy Boost of Heavy Ions for Laser-Plasma Acceleration*, Physical Review Letters **114**, (2015).

[95] Wenjun Ma, V.kh. Liechtenstein, J. Szerypo, D. Jung, P. Hilz, B.m. Hegelich, H.j. Maier, J. Schreiber and D. Habs, *Preparation of self-supporting diamond-like carbon nanofoils with thickness less than 5nm for laser-driven ion acceleration*, Nuclear Instruments and Methods in Physics Research Section A: Accelerators, Spectrometers, Detectors and Associated Equipment **655**, 53 (2011).

[96] P. Mckenna, K. W. D. Ledingham, J. M. Yang, L. Robson, T. Mccanny, S. Shimizu, R. J. Clarke, D. Neely, K. Spohr, R. Chapman and et al., *Characterization of proton and heavier ion acceleration in ultrahigh-intensity laser interactions with heated target foils*, Physical Review E **70**, (2004).

[97] Lieselotte Obst, Sebastian Göde, Martin Rehwald, Florian-Emanuel Brack, Joao Branco, Stefan Bock, Michael Bussmann, Thomas E. Cowan, Chandra B. Curry, Frederico Fiuza and et al., *Efficient laser-driven proton acceleration from cylindrical and planar cryogenic hydrogen jets*, Scientific Reports **7**, (2017).

[98] M. Gauthier, J. B. Kim, C. B. Curry, B. Aurand, E. J. Gamboa, S. Göde, C. Goyon, A. Hazi, S. Kerr, A. Pak and et al., *High-intensity laser-accelerated ion beam produced from cryogenic micro-jet target*, Review of Scientific Instruments **87**, (2016).

[99] M. Berglund, L. Rymell, H. M. Hertz and T. Wilhein, *Cryogenic liquid-jet target for debris-free laser-plasma soft x-ray generation*, Review of Scientific Instruments **69**, 2361 (1998).

[100] S. S. Bulanov, A. Brantov, V. Yu. Bychenkov, V. Chvykov, G. Kalinchenko, T. Matsuoka, P. Rousseau, S. Reed, V. Yanovsky, D. W. Litzenberg and et al., *Accelerating monoenergetic protons from ultrathin foils by flat-top laser pulses in the directed-Coulomb-explosion regime*, Physical Review E **78**, (2008).

[101] I. Jong Kim, Ki Hong Pae, Il Woo Choi, Chang-Lyoul Lee, Hyung Taek Kim, Himanshu Singhal, Jae Hee Sung, Seong Ku Lee, Hwang Woon Lee, Peter V. Nickles and et al., *Radiation pressure acceleration of protons to 93 MeV with circularly polarized petawatt laser pulses*, Physics of Plasmas **23**, 070701 (2016).

[102] V. Yanovsky, V. Chvykov, G. Kalinchenko, P. Rousseau, T. Planchon, T. Matsuoka, A. Maksimchuk, J. Nees, G. Cheriaux, G. Mourou and et al., *Ultra-high intensity- 300-TW laser at 0.1 Hz repetition rate*, Optics Express **16**, 2109 (2008).

[103] Hermann Haken, *Atom- und Quantenphysik: Einfuhrung in die experimentellen und theoretischen Grundlagen* (Springer, Berlin Heidelberg, 2003).

[104] A. Bruce Langdon, *Nonlinear Inverse Bremsstrahlung and Heated-Electron Distributions*, Physical Review Letters **44**, 575 (1980).

[105] CE Max, *Theory of the coronal plasma in laser fusion targets* (Lawrence Livermore Laboratory, University of California, 1981).

[106] Vitalij L. Ginzburg and Vitalij L. Ginzburg, *The propagation of electromagnetic waves in plasmas* (Pergamon Press, Oxford, 1970).

[107] William L. Kruer, *The physics of laser plasma interactions* (Westview, Boulder, CO, 2003).

[108] D. Gabor, *A New Microscopic Principle*, Nature **161**, 777 (1948).

[109] A. Einstein, *Zur Elektrodynamik bewegter Körper*, Annalen der Physik **322**, 891 (1905).

[110] B. Dromey, S. Kar, C. Bellei, D. C. Carroll, R. J. Clarke, J. S. Green, S. Kneip, K. Markey, S. R. Nagel, P. T. Simpson and et al., *Bright Multi-keV Harmonic Generation from Relativistically Oscillating Plasma Surfaces*, Physical Review Letters **99**, (2007).

[111] B. Dromey, M. Zepf, A. Gopal, K. Lancaster, M. S. Wei, K. Krushelnick, M. Tatarakis, N. Vakakis, S. Moustaizis, R. Kodama and et al., *High harmonic generation in the relativistic limit*, Nature Physics **2**, 456 (2006).

[112] D. Kiefer, M. Yeung, T. Dzelzainis, P.s. Foster, S.g. Rykovanov, C.ls. Lewis, R.s. Marjoribanks, H. Ruhl, D. Habs, J. Schreiber and et al., *Relativistic electron mirrors from nanoscale foils for coherent frequency upshift to the extreme ultraviolet*, Nature Communications **4**, (2013).

[113] M. Zepf, M. Costro-Colin, D. Chambers, S. G. Preston, J. S. Wark, J. Zhang, C. N. Danson, D. Neely, P. A. Norreys, A. E. Dangor and et al., *Measurements of the hole boring velocity from Doppler shifted harmonic emission from solid targets*, Physics of Plasmas **3**, 3242 (1996).

[114] C. A. J. Palmer, J. Schreiber, S. R. Nagel, N. P. Dover, C. Bellei, F. N. Beg, S. Bott, R. J. Clarke, A. E. Dangor, S. M. Hassan and et al., *Rayleigh-Taylor Instability of an Ultrathin Foil Accelerated by the Radiation Pressure of an Intense Laser*, Physical Review Letters **108**, (2012).

[115] R. Sauerbrey, *Acceleration in femtosecond laser-produced plasmas*, Physics of Plasmas **3**, 4712 (1996).

[116] Information@eso.org, Very Large Telescope, https://www.eso.org/public/teles-instr/paranal-observatory/vlt/.

[117] Demtröder Wolfgang, *Laserspektroskopie* (Springer, Berlin, 2011).

[118] John M. Dawson, *Particle simulation of plasmas*, Reviews of Modern Physics **55**, 403 (1983).

[119] V. Bagnoud, J. Hornung, T. Schlegel, B. Zielbauer, C. Brabetz, M. Roth, P. Hilz, M. Haug, J. Schreiber, F. Wagner and et al., *Studying the Dynamics of Relativistic Laser-Plasma Interaction on Thin Foils by Means of Fourier-Transform Spectral Interferometry*, Physical Review Letters **118**, (2017).

[120] Florian Wagner, Stefan Bedacht, Alex Ortner, Markus Roth, Anna Tauschwitz, Bernhard Zielbauer and Vincent Bagnoud, *Pre-plasma formation in experiments using petawatt lasers*, Optics Express **22**, 29505 (2014).

[121] V. Bagnoud and F. Wagner, *Ultrahigh temporal contrast performance of the PHELIX petawatt facility*, High Power Laser Science and Engineering **4**, (2016).

[122] Heiko Burau, Renee Widera, Wolfgang Honig, Guido Juckeland, Alexander Debus, Thomas Kluge, Ulrich Schramm, Tomas E. Cowan, Roland Sauerbrey, Michael Bussmann and et al., *PIConGPU: A Fully Relativistic Particle-in-Cell Code for a GPU Cluster*, IEEE Transactions on Plasma Science **38**, 2831 (2010).

[123] Martin Centurion, Ye Pu, Zhiwen Liu, Demetri Psaltis and Theodor W. Hänsch, *Holographic recording of laser-induced plasma*, Optics Letters **29**, 772 (2004).

[124] K. Sakai and S. Noda, *Optical trapping of metal particles in doughnut-shaped beam emitted by photonic-crystal laser*, Electronics Letters **43**, 107 (2007).

Peer-reviewed publications

[1] D. Haffa, R. Yang, J. Bin, S. Lehrack, F. E. Brack, H. Ding, F. Englbrecht, Y. Gao, J. Gebhard, M. Gilljohann, J. Götzfried, J. Hartmann, S. Herr, **P. Hilz**, S. Kraft, C. Kreuzer, F. Kroll, F. Lindner, J. Metzkes-Ng and J. Schreiber, *I-BEAT: Ultrasonic method for online measurement of the energy distribution of a single ion bunch*, Scientific Reports **9**, (2019).

[2] G. A. Becker, S. Tietze, S. Keppler, J. Reislöhner, J. H. Bin, L. Bock, F. Brack, J. Hein, M. Hellwing, **P. Hilz**, M. Hornung, A. Kessler, S. D. Kraft, S. Kuschel, H. Liebetrau, W. Ma, J. Polz, H. Schlenvoigt, F. Schorcht, M. B. Schwab, A. Seidel, K. Zeil, U. Schramm, M. Zepf, J. Schreiber, S. Rykovanov and M. C. Kaluza, *Ring-like spatial distribution of laser accelerated protons in the ultra-high-contrast TNSA-regime*, Plasma Physics and Controlled Fusion **60**, 055010 (2018).

[3] **P. Hilz**, T. M. Ostermayr, A. Huebl, V. Bagnoud, B. Borm, M. Bussmann, M. Gallei, J. Gebhard, D. Haffa, J. Hartmann and et al., *Isolated proton bunch acceleration by a petawatt laser pulse*, Nature Communications **9**, (2018).

[4] T. M. Ostermayr, J. Gebhard, D. Haffa, D. Kiefer, C. Kreuzer, K. Allinger, C. Bömer, J. Braenzel, M. Schnürer, I. Cermak, J. Schreiber and **P. Hilz**, *A transportable Paul-trap for levitation and accurate po-*

sitioning of micron-scale particles in vacuum for laser-plasma experiments, Review of Scientific Instruments **89**, 013302 (2018).

[5] F. H. Lindner, J. H. Bin, F. Englbrecht, D. Haffa, P. R. Bolton, Y. Gao, J. Hartmann, **P. Hilz**, C. Kreuzer, T. M. Ostermayr, T. F. Rösch, M. Speicher, K. Parodi, P. G. Thirolf and J. Schreiber, *A novel approach to electron data background treatment in an online wide-angle spectrometer for laser-accelerated ion and electron bunches*, Review of Scientific Instruments **89**, 013301 (2018).

[6] T. Rösch, **P. Hilz**, J. Bin, F. Englbrecht, Y. Gao, D. Haffa, J. Hartmann, S. Herr, F. Lindner, M. Speicher, M. Würl, K. Parodi and J. Schreiber, *Considerations on employing a PMQ-doublet for narrow and broad proton energy distributions*, Current Directions in Biomedical Engineering **3**, (2017).

[7] V. Bagnoud, J. Hornung, T. Schlegel, B. Zielbauer, C. Brabetz, M. Roth, **P. Hilz**, M. Haug, J. Schreiber and F. Wagner, *Studying the Dynamics of Relativistic Laser-Plasma Interaction on Thin Foils by Means of Fourier-Transform Spectral Interferometry*, Physical Review Letters **118**, (2017).

[8] S. Seuferling, M. Haug, **P. Hilz**, D. Haffa, C. Kreuzer and J. Schreiber, *Efficient offline production of freestanding thin plastic foils for laser-driven ion sources*, High Power Laser Science and Engineering **5**, (2017).

[9] Y. Gao, J. Bin, D. Haffa, C. Kreuzer, J. Hartmann, M. Speicher, F. H. Lindner, T. M. Ostermayr, **P. Hilz**, T. F. Rösch and et al., *An automated, 0.5 Hz nano-foil target positioning system for intense laser plasma experiments*, High Power Laser Science and Engineering **5**, e12 (2017).

[10] F.H. Lindner, D. Haffa, J.H. Bin, F. Englbrecht, Y. Gao, J. Gebhard, J. Hartmann, **P. Hilz**, C. Kreuzer, S. Lehrack, T.M. Ostermayr and

T.F. R *Towards swift ion bunch acceleration by high-power laser pulses at the Centre for Advanced Laser Applications (CALA)*, Nuclear Instruments and Methods in Physics Research Section B: Beam Interactions with Materials and Atoms **402**, 354 (2017), proceedings of the 7th International Conference Channeling 2016: Charged & Neutral Particles Channeling Phenomena.

[11] T. M. Ostermayr, D. Haffa, **P. Hilz**, V. Pauw, K. Allinger, K.-U. Bamberg, P. Böhl, C. Bömer, P. R. Bolton, F. Deutschmann, T. Ditmire, M. E. Donovan, G. Dyer, E. Gaul, J. Gordon, B. M. Hegelich, D. Kiefer, C. Klier, C. Kreuzer, M. Martinez, E. McCary, A. R. Meadows, N. Moschüring, T. Rösch, H. Ruhl, M. Spinks, C. Wagner and J. Schreiber, *Proton acceleration by irradiation of isolated spheres with an intense laser pulse*, Phys. Rev. E **94**, 033208 (2016).

[12] N. P. Dover, C. A. J. Palmer, M. J. V. Streeter, H. Ahmed, B. Albertazzi, M. Borghesi, D. C. Carroll, J. Fuchs, R. Heathcote, **P. Hilz**, K. F. Kakolee, S. Kar, R. Kodama, A. Kon, D. A. MacLellan, P. McKenna, S. R. Nagel, D. Neely, M. M. Notley, M. Nakatsutsumi, R. Prasad, G. Scott, M. Tampo, M. Zepf, J. Schreiber and Z. Najmudin, *Buffered high charge spectrally-peaked proton beams in the relativistic-transparency regime*, New Journal of Physics **18**, 013038 (2016).

[13] J. H. Bin, W. J. Ma, K. Allinger, H. Y. Wang, D. Kiefer, S. Reinhardt, **P. Hilz**, K. Khrennikov, S. Karsch, X. Q. Yan, F. Krausz, T. Tajima, D. Habs and J. Schreiber, *On the small divergence of laser-driven ion beams from nanometer thick foils*, Physics of Plasmas **20**, 073113 (2013).

[14] S. Steinke, **P. Hilz**, M. Schnürer, G. Priebe, J. Bränzel, F. Abicht, D. Kiefer, C. Kreuzer, T. Ostermayr, J. Schreiber, A. A. Andreev, T. P. Yu, A. Pukhov and W. Sandner, *Stable laser-ion acceleration in the light sail regime*, Phys. Rev. ST Accel. Beams **16**, 011303 (2013).

[15] J. Braenzel, C. Pratsch, **P. Hilz**, C. Kreuzer, M. Schnürer, H. Stiel and W. Sandner, *Note: Thickness determination of freestanding ultra-thin foils using a table top laboratory extreme ultraviolet source*, The Review of scientific instruments **84**, 056109 (2013).

[16] C. Palmer, J. Schreiber, S. Nagel, N. Dover, C. Bellei, F. Beg, S. Bott-Suzuki, R. Clarke, A. Dangor, S. Hassan, **P. Hilz**, D. Jung, S. Kneip, S. Mangles, K. Lancaster, A. Rehman, A. Robinson, C. Spindloe, J. Szerypo and Z. Najmudin, *Rayleigh-Taylor Instability of an Ultrathin Foil Accelerated by the Radiation Pressure of an Intense Laser*, Phys. Rev. Lett. **108**, 225002 (2012).

[17] J. Bin, K. Allinger, W. Assmann, G. Dollinger, G. A. Drexler, A. A. Friedl, D. Habs, **P. Hilz**, R. Hoerlein, N. Humble, S. Karsch, K. Khrennikov, D. Kiefer, F. Krausz, W. Ma, D. Michalski, M. Molls, S. Raith, S. Reinhardt, B. Röper, T. E. Schmid, T. Tajima, J. Wenz, O. Zlobinskaya, J. Schreiber and J. J. Wilkens, *A laser-driven nanosecond proton source for radiobiological studies*, Applied Physics Letters **101**, 243701 (2012).

[18] W. Ma, V.Kh. Liechtenstein, J. Szerypo, D. Jung, **P. Hilz**, B.M. Hegelich, H.J. Maier, J. Schreiber and D. Habs, *Preparation of self-supporting diamond-like carbon nanofoils with thickness less than 5nm for laser-driven ion acceleration*, Nuclear Instruments and Methods in Physics Research Section A: Accelerators, Spectrometers, Detectors and Associated Equipment **655**, 53 (2011), proceedings of the 25th World Conference of the International Nuclear Target Development Society.

[19] S. Becker, **P. B. Hilz**, F. Grüner and D. Habs, *Retardation effects in space charge calculations of high current electron beams*, Phys. Rev. ST Accel. Beams **12**, 101301 (2009).

Danksagung

Ivo Cermak konzipierte große Teile der Paulfallenelektronik, vielen Dank dafür.

Ganz besonderer Dank gilt den mechanischen Werkstätten und der Konstruktionsabteilung der LMU München. Das Team von Rolf Oehm hat etliche ‚Paulteile' gefertigt, die vom Konstruktionsteam unter der Leitung von Johannes Wulz gewissenhaft ‚gemalt' wurden.

Dem Technologischen Labor mit Uli Friebel, Simon Stork und Jerzy Szerypo danke ich für die tatkräftige Unterstützung was die Produktion von Targets anging.

Stephan Becker habe ich damals geholfen sein Labor zu räumen, damit ich dort anfangen konnte. Das war der Beginn unserer Freundschaft.

Die unzähligen Diskussionen mit Gabriel Schaumann bezüglich der Produktion von Targets habe ich stets genossen.

Professor Kraus und Professor Rempe möchte ich für Ihre ganz besondere Motivation danken.

Professor Habs danke ich für seinen unermüdlichen Eifer und seine Visionen, welche die Hochintensitätslaserphysik in München und darüber hinaus etabliert haben.

Professor Matt Zepf - dir möchte ich für das in mich gesetzte Vertrauen danken.

Ich danke meinen Eltern für Ihre unermüdliche Unterstützung, die sie mir schon immer zukommen haben lassen. Dank Ihnen kann ich den Weg im Leben beschreiten den ich mir wünsche. Ohne sie wäre ich nie so weit gekommen.

Der größte Dank gilt meiner Frau Angela und meinen Kindern Simon und Elisabeth. Ihr seid mein Leben.